

The Chemical Abundances of the Stellar Populations in the Leo I and Leo II dSph Galaxies^{*}

Tammy L. Bosler,¹ Tammy A. Smecker-Hane², Peter B. Stetson³

¹*National Science Foundation, Division of Astronomical Sciences.*

²*Department of Physics & Astronomy, 4129 Frederick Reines Hall, University of California, Irvine, CA 92697–4575.*

³*National Research Council of Canada, Herzberg Inst. of Astrophysics, Dominion Astrophysical Observatory, 5071 West Saanich Road, Victoria, BC V9E 2E7, Canada.*

28 August 2018

ABSTRACT

We have obtained calcium abundances and radial velocities for 102 red giant branch (RGB) stars in the Leo I dwarf spheroidal galaxy (dSph) and 74 RGB stars in the Leo II dSph using the Low Resolution Spectrograph (LRIS) on the Keck I 10-meter Telescope. We report on the calcium abundances $[\text{Ca}/\text{H}]$ derived from the strengths of the Ca II triplet absorption lines at 8498, 8542, 8662 Å in the stellar spectra using a new empirical Ca II triplet calibration to $[\text{Ca}/\text{H}]$. The two galaxies have different average $[\text{Ca}/\text{H}]$ values of -1.34 ± 0.02 for Leo I and -1.65 ± 0.02 for Leo II with intrinsic abundance dispersions of 1.2 and 1.0 dex, respectively. The typical random and total errors in derived abundances are 0.10 and 0.17 dex per star. For comparison to existing literature, we also converted our Ca II measurements to $[\text{Fe}/\text{H}]$ on the scale of Carretta and Gratton (1997) though we discuss why this may not be the best determinant of metallicity; Leo I has a mean $[\text{Fe}/\text{H}] = -1.34$ and Leo II has a mean $[\text{Fe}/\text{H}] = -1.59$. The metallicity distribution function of Leo I is approximately Gaussian in shape with an excess at the metal-rich end, while that of Leo II shows an abrupt cutoff at the metal-rich end. The lower mean metallicity of Leo II is consistent with the fact that it has a lower luminosity, hence lower total mass, than Leo I; thus the evolution of Leo II may have been affected more by mass lost in galactic winds. Our direct and independent measurement of the metallicity distributions in these dSph will allow a more accurate star-formation histories to be derived from future analysis of their CMDs.

Key words: stars: abundances — galaxies: abundances — galaxies: evolution — galaxies: dwarf — galaxies: individual (Leo I dSph, Leo II dSph)

1 INTRODUCTION

The goal of this project is to map the chemical abundance distribution of the stellar populations of the Leo I and Leo II dwarf spheroidal (dSph) galaxies in order to constrain the physical processes that regulate their evolution. Table 1 lists the properties of each galaxy for reference.

Dwarf spheroidal galaxies (dSphs) are low luminosity ($M_V \leq -14$ mag), low surface brightness ($\Sigma_V \lesssim 22$ mag/arcsec²), and low mass ($M_{tot} \lesssim 10^7 M_\odot$) systems. They have little or no interstellar gas ($M_{HI} \lesssim 10^5 M_\odot$), and are dark-matter dominated. For recent reviews, see Mateo (1998), Smecker-Hane & McWilliam (1999), and Grebel (2000). Their stellar velocity dispersions are

typically ~ 10 km/sec, and therefore galactic winds from the first generation of supernovae are expected to efficiently rid them of gas and prevent extended or multiple epochs of star formation. Although they seem to lack the mass and material to sustain star formation for a significant fraction of the Hubble time, the CMDs of the dSph satellites of the Milky Way have shown that most dSphs have *very complex* star formation histories (SFHs) and chemical evolution. Cold dark matter hierarchical galaxy formation models have difficulty explaining extended epochs of star formation in dSphs. They are predicted to begin forming stars at early epochs, but lose a significant amount of gas due to photoevaporation during reionization, which curtails their star formation activity (Barkana & Loeb 1999). Klypin et al. (1999) also points out that CDM models vastly over predict the number of low mass halos; the Milky Way and M31 have only one-tenth the number of low mass satellites. Are these “missing” satellites dark because they never accreted gas, or were the dark matter halos stripped of their baryons through supernovae-driven winds? Determining the age of the oldest stars in the outer halo satellites such as the Leo I and Leo II dSphs, whose

^{*} Data presented herein were obtained at the W.M. Keck Observatory, which is operated as a scientific partnership among the California Institute of Technology, the University of California and the National Aeronautics and Space Administration. The Observatory was made possible by the generous financial support of the W.M. Keck Foundation.

Galactocentric distances are 270 and 204 kpc, respectively, is important because CDM models predict that these should form later than the Milk Way’s inner halo globular clusters and dSphs.

Almost every dSph in the Local Group appears to have had a unique SFH. From analysis of a CMD obtained with WFPC2 aboard the HST, Mighell & Rich (1996) have shown that the Leo II dSph formed essentially all of its stars from ~ 7 to 14 Gyr ago with 50% of its stars formed in a 4 Gyr period. In striking contrast, most of the stars in the Leo I dSph are younger than this; 87% of its star formation occurred from 1 to 7 Gyr ago and only 12% occurred $\gtrsim 10$ Gyr ago (Gallart et al. 1999a and 1999b). More recent photometry from Held et al. (2000), which includes a much larger radial coverage than the HST data, also shows an extended blue horizontal-branch in Leo I indicating the existence of an old, metal-poor population. Held et al. (2001) also report the discovery of candidate RR Lyrae stars in the system, further strengthening the case for an old population in Leo I.

Defining the chemical evolution of the dSphs will be key to understanding their complex SFHs because the chemical abundances constrain the inflow and outflow of gas from the systems. Did some dSphs accrete fresh gas that fuelled subsequent star formation? Were outflows driven by supernovae so extensive that today’s dSphs have only a small fraction of their former mass? The chemical abundances of dSph stars – the mean metallicity as well as the detailed distribution in metallicity – can be determined from spectroscopy of individual red giant stars in the dSphs. Measuring the metallicity distribution of individual stars will greatly improve the SFHs derived from analysis of CMDs.

In order to understand the true spread in stellar chemical abundances more precise abundance indicators than can be inferred from CMD analysis are needed. We, therefore, measured the abundance distribution of the Leo I and Leo II dSphs from spectroscopy of individual red giant stars using the Ca II absorption lines in the near infrared (8498, 8542, and 8662 Å). We utilized the new calibration of Ca II to [Ca/H] from Bosler (2004, hereafter B04) to derive abundances with random and total errors of 0.10 and 0.17 dex, respectively. This new empirical calibration to calcium abundances avoids the inherent dependence on [Ca/Fe] built into the existing Ca II calibration to [Fe/H]. However, in order to allow for easier comparison to earlier Ca II work on Local dwarf galaxies, we also calculated the [Fe/H] values of the stars based on the Rutledge et al. (1999) calibration; however, we discuss the pitfalls of using the Ca II triplet to determine [Fe/H]. The new Ca II calibration to [Ca/H] is completely independent of star to star variations in [Ca/Fe] unlike previously utilized Ca II abundance calibrations.

2 THE SAMPLE

The photometry and astrometry for Leo I and Leo II were obtained as part of a larger program to provide homogeneous photometry for star clusters and nearby resolved galaxies (e.g., Stetson, Hesser & Smecker-Hane 1998, Stetson 2000). The present photometry is based upon a large database of CCD images acquired by ourselves and collaborators, images obtained from the archives of the Canada-France-Hawaii Telescope and the Isaac Newton Group, and images privately donated by other astronomers. In the present case, the Leo I photometric database contains some 30,000 different stars recorded in 449 individual CCD images taken in the UBVR filters (4 in U, 96 in B, 257 in V, 72 in R, and 20 in I) covering an irregular area spanning an extreme range of 40.7’ in the east-west direction by 40.6’ north-south. For Leo II, some 17,000 stars

were measured in 124 CCD images taken in UBVR filters (2 in U, 30 in B, 81 in V, 5 in R, and 6 in I) spanning an area with extreme dimensions 16.9’ by 16.5’. All observations were transformed to the UBVR photometric system of Landolt (1992; see also Stetson 2000) based on observations of primary (Landolt) and secondary (Stetson) standard stars obtained during the same nights with the same equipment.

The astrometry for the Leo I and II photometric catalogs was based on positions of reference stars taken from the United States Naval Observatory Guide Star Catalogue A2.0; (henceforth USNOGSC, Monet et al. 1998), access to which was obtained through the services of the Canadian Astronomy Data Center. The authors of the USNOGSC claim a typical astrometric error of 0.25 arcsec, which they believe is dominated by systematic errors in the calibration procedure. When transforming relative (x, y) positions from large-format CCD images to absolute right ascensions and declinations from the USNOGSC for stars in common, the typical root-mean-square difference is 0.3 to 0.4 arcsec in each coordinate. Some of this is clearly due to proper-motion displacements accumulated during the forty-plus years between the obtaining of the first Palomar Observatory Sky Survey and these CCD data. However, a significant part of the differences is also due to the lower angular resolution of the Schmidt plates as scanned by the Precision Measuring Machine (built and operated by the U. S. Naval Observatory Flagstaff): particularly in crowded fields such as these, a single entry in the USNOGSC is occasionally found to correspond to the photocenter of a close pair or a clump of several stars in the CCD imagery.

As a result of these non-Gaussian errors (i.e., proper motions and blending), astrometric transformations were performed using an iterative procedure wherein 20-constant cubic polynomials are used to approximate the transformation of the (x, y) positions measured in the CCD images to standard coordinates obtained from the USNOGSC (see Cohen, Briley, & Stetson 2002 for more details). When this procedure has been completed 706 detections common to the USNOGSC were found and the data set in the field of Leo I show positional differences with a dispersion of 0.37 arcsec in both the right ascension and declination directions; for Leo II, 292 stars show positional agreement with a dispersion of 0.32 arcsec in each direction.

The systematic errors of right ascensions and declinations on the system of the USNOGSC are expected to be of order $\sigma/\sqrt{N-20} \sim 0.02$ arcsec where N is the number of stars used in the astrometric solution. We can provide no independent information on the accuracy with which the USNOGSC coordinate system is referred to an absolute inertial reference frame of right ascension and declination. Individual *random* errors in the coordinate measurements are probably not much better than 0.02 arcsec on a star-by-star basis, the errors becoming somewhat worse where crowding is an issue. The logarithm of the observed flux in the stellar spectra is very well correlated with our V-band magnitudes for the stars, and thus there is no evidence of sizable relative position errors compared to the size of the 1.0 arcsec-wide slits. However while aligning LRIS slit masks on the stars in a given field, one rotates the field of view to get the best possible alignment, and thus the flux measurements do not rule out possible systematic rotations of the coordinate system with respect to the true inertial frame. Still, these should not be present at levels much greater than the 0.02-arcsec precision claimed above. A comprehensive catalog of positions and photometry for these two galaxies is in preparation.

Our current CMDs for the Leo I and Leo II dSphs are shown in Figures 1 and 2, respectively. The stars in the spectroscopic sam-

ple are marked with large open circles. On each CMD, fiducials for two Galactic globular clusters with different metallicities are plotted for comparison. For Leo I, we have assumed a reddening of $E(V-I) = 1.25[1 + 0.06(B-V)_0 + 0.014E(B-V)]$ $E(B-V) = 0.054$ mag using the reddening relationship derived by Dean, Warren & Cousins (1978) and assuming the mean color of the red giant branch (RGB) stars is $(B-V)_0 = 1.2$. We have defined fiducial RGBs for each dSph, which were used to quantify the color distribution in each dSph and ensure that the spectroscopic targets span the color range, and thus the selection is as representative in metallicity as possible. For the Leo I fiducial, we simply adopted the fiducial for M15 = NGC 7078 (Da Costa & Armandroff 1990), which has $[Fe/H] = -2.02$, because it lies roughly along the middle of the Leo I RGB. Because of the age-metallicity degeneracy in the CMD, the old (14 Gyr), metal-poor M15 RGB fiducial lies along the same part of the CMD as the RGB of the younger (4 Gyr), intermediate-metallicity Leo I RGB fiducial. Yale isochrones with $[Fe/H] = -1.28$ and ages 2 and 4 Gyrs have been plotted on the Leo I CMD to illustrate the young ages of the stars on blue edge of the RGB. For the Leo II fiducial, we adopted the fiducial of the Galactic globular cluster M68 = NGC 4590 (McClure, et al. 1987), which has $[Fe/H] = -1.92$, with an additional shift of 0.1 mag in $(B-V)$ so that it ran along the middle of the Leo II RGB.

All dSph stars selected for observation have $-3 \leq V - V_{HB} \leq -2$ and $1.0 \leq V - I \leq 1.5$, where V_{HB} is the V-band magnitude of the horizontal branch. In order to have the spectroscopic sample be as representative as possible with respect to color and metallicity, we chose stars with the aim of spanning the same distribution in color as the entire sample. To quantify this, we defined the color difference, $\Delta_{(B-V)}$, to be the B-V color of an individual star minus the B-V color of the fiducial RGB at the V-magnitude of the star. We used B and V-band photometry to select Leo II stars, and V and I-band photometry to select Leo I stars for spectroscopy. Note that the images in the RI filters of the Leo II fields were taken under non-photometric conditions and remain uncalibrated. In designing the slit mask configurations, we attempted to match the distribution in $\Delta_{(V-I)}$ and $\Delta_{(B-V)}$ for Leo I and Leo II, respectively. The histograms of color differences are illustrated in Figures 3 and 4.

Candidate red giants in the Leo I and Leo II dSphs were chosen for spectroscopic observations based on their location in the CMD and position in the slit mask field-of-view, which was $4' \times 7'$ on the sky. Using five slit mask orientations for Leo I we covered the core radius of the galaxy and 83% of the tidal radius along the east-west axis; only 56% of the tidal radius was covered along the north-south axis. Leo II was observed with four slit mask orientations, which covered an area of $7' \times 7'$ on the sky; this covered all of the core radius of the galaxy and approximately 80% of the tidal radius.

3 OBSERVATIONS

We obtained low-dispersion spectra of red giants in Leo I and Leo II dSphs using the Keck I 10-meter telescope and LRIS (Oke et al. 1995) during 2 runs; run 1 was on 8 February 2002, and run 2 was on 5 March 2003 (UT). The pixel scale of the CCD in the spatial direction was $0.215''/\text{pixel}$. The CCD was read out using two amplifiers with gains of 1.97 and 2.10 e^-/adu , and readnoises of 6.3 and 6.6 e^- , for the left and right amplifiers, respectively. We used the 1200 l/mm grating blazed at 7500 Å, which gave a dispersion of 0.62 Å/pix and resolution of 1.55 Å ($R \approx 14,000$).

The GG495 filter was used to block second-order light. In multi-slit mode, the available field of view was $4' \times 7'$ for a minimum spectral coverage extending from 8355 – 8890 Å. The slit widths were 1.0'' and the minimum slit length was 6.0''. We were able to observe approximately 20 to 30 stars per multi-slit mask. In the long-slit mode which was used for some of the calibration stars, the slit was $1.0'' \times 3.0'$. The typical seeing was 0.8'' as measured by the FWHM of the profile of the spectra along the spatial direction.

Exposure times were 4×900 sec for most masks. Observations of one field in Leo I was only 2×900 sec due to a pointing problem which caused the stars to be off center of the slits for 2 exposures which were not used in the analysis. Due to LRIS's sizable flexure, we obtained spectra of the Ne-Ar arc lamp and a halogen flat after the final exposure on each target for calibration purposes. In addition, a radial velocity standard and telluric standards (rapidly rotating, B-type stars) were observed in long-slit mode. Spectra of red giants in four Galactic globular clusters were also taken using the slit mask configuration to place our equivalent width measurements on the well-defined scale of Rutledge et al. (1997a and 1997b; hereafter R97a and R97b).

4 DATA REDUCTION

The usual CCD image reduction procedures of overscan fitting, overscan subtraction, and zero subtraction were done using routines we developed in the Interactive Data Language (IDL)¹. The two amplifiers have different zero levels, which needed to be taken into account when creating the zero image. Two bad pixels caused bleeding on the Amp 1 side and created structure in the zero image. Further reductions followed those outlined in the data reduction tutorial on the LRIS web page (<http://\alamoana.keck.hawaii.edu/inst/lris>) and Massey et al. (1992) with slight modification in reduction parameters. Cosmic ray removal, flat fielding in two dimensions, extraction of spectra from two dimensions to one dimension, and normalizing the continuum to unity were performed with tasks in the IMRED package of the Image Reduction and Analysis Facility (IRAF)².

Distortion in both the dispersion direction (x axis) and spatial direction (y axis) had to be corrected in the 2-D spectra before the spectra were extracted to 1-D. We mapped and corrected distortions along the y axis of spectra using IRAF's IDENTIFY, REIDENTIFY and FITCOORDS tasks on halogen flats taken directly after each exposure. We applied the distortion correction to the arc and object exposures using the TRANSFORM task. To correct the distortion along the x axis, we used the IRAF-based task XDISTOR (Greg Wirth 2002, private comm.) adapted to the specifications of the data set. This task uses the strong night sky lines in the object spectra, or arc lines in the Ne-Ar spectra, to map and correct the distortion in the spectral direction for each aperture. The distortion correction was very accurate; after correction, the shifts in the centroids of typical arc lines over the most distorted apertures at the top and bottom of an image were $\lesssim 0.05$ pixels, which is $\lesssim 1.6\%$ of the FWHM.

Because the spectrograph has sizable flexure over the 4×900 sec observation times, the wavelength solution for each aperture

¹ IDL is commercial software sold by Research Systems, Inc.

² IRAF is freely distributed by the National Optical Astronomy Observatories, which is operated by the Association of Universities for Research in Astronomy, Inc., under cooperative agreement with the National Science Foundation.

was determined using bright night sky lines in the spectra themselves rather than the arc lamps taken after each set of exposures. Most of the night sky lines were blended at our $0.62 \text{ \AA}/\text{pix}$ dispersion so we did not adopt the wavelengths of the sky lines determined from high-dispersion spectra (e.g., Osterbrock et al. 1996, Osterbrock & Fulbright 1997). Instead, we calculated the central wavelength for approximately 40 bright, night-sky emission lines in 25 apertures using Ne-Ar spectra taken immediately after an exposure. Each stellar spectrum was wavelength calibrated by using 25 to 40 night sky lines fit with a spline3 (1st order) fit, which yielded wavelength solutions with typical RMS residuals of 0.03 \AA . Each slit had a unique wavelength coverage that fell somewhere in the range of $7770 - 9440 \text{ \AA}$.

Different spectra for individual targets were combined using the IRAF SCOMBINE task rejecting outliers at the 3σ level. The continua of all spectra were fit with cubic splines, rejecting absorption features, and normalized to unity with the CONTINUUM task to produce the final calibrated spectra. We measured the average signal-to-noise ratio per pixel (SNR) in each spectrum by calculating the RMS in two wavelength windows where absorption features are weak, $8580 - 8620 \text{ \AA}$ and $8700 - 8800 \text{ \AA}$, and averaged the results. The mean SNR was 18 for Leo I stars and 23 for Leo II stars, and the range was $6 \leq \text{SNR} \leq 42$ for all of the observed dSph stars. Abundances were only determined for stars with SNR greater than 10 and for which at least the two strongest Ca II lines were observed. These criteria reduced the number of stars analyzed from 121 to 102 for Leo I and from 90 to 74 for Leo II.

5 DATA ANALYSIS

In this section the measurement of heliocentric velocities, the reduced equivalent widths of the Ca II lines, and metallicities are discussed.

5.1 Heliocentric Velocities

We verified membership of the stars in each dSph by deriving their radial velocities because the intrinsic velocity dispersions of these galaxies are well-defined, $\sim 10 \text{ km/s}$, and very different than stars in the Milky Way. We computed heliocentric radial velocities, v_{helio} , by cross-correlation (e.g. Tonry & Davis 1979) with a spectrum of IAU radial velocity standard HD 12029 (K2III spectral type, $B-V = 1.24$, $v_{\text{helio}} = 40.0 \text{ km sec}^{-1}$) for Run 1 and HD 35410 (G9III spectral type, $B - V = 0.95$, $v_{\text{helio}} = 20.3 \text{ km sec}^{-1}$) for Run 2. We used our IRAF task RVITERATE to iterate the cross-correlation performed by the IRAF FXCOR task. RVITERATE changes the window of the observed wavelength in the object spectrum over which the correlation is performed until the rest frame window of $8200 - 9000 \text{ \AA}$ was used in both the template and object spectrum. A ramp filter was used to filter out the large wavelength fluctuations from any telluric bands on scales $\approx 40 \text{ \AA}$, and small scale fluctuations from random noise.

For 121 stars observed in Leo I, the median velocity error is 9.2 km sec^{-1} . We found the average heliocentric velocity, weighted by the errors, is $\langle v_{\text{helio}} \rangle = +282.6 \pm 9.8 \text{ km sec}^{-1}$. Mateo, et al. (1998) found $\langle v_{\text{helio}} \rangle = +287.0 \pm 2.2 \text{ km sec}^{-1}$ based on high-dispersion spectra of 15 RGB stars. For 90 stars observed in Leo II, the median velocity error is 8.5 km sec^{-1} . We found $\langle v_{\text{helio}} \rangle = +85.8 \pm 8.4 \text{ km sec}^{-1}$. Vogt, et al. (1995) found $\langle v_{\text{helio}} \rangle = +76.0 \pm 1.3 \text{ km sec}^{-1}$ and a dispersion of $\sigma_{v_{\text{helio}}} = 6.7 \pm$

1.1 km sec^{-1} based on high-dispersion spectra of 31 red giants. The differences between the mean velocities for this work and those of earlier work are not significant given the differences in the spectral resolution between the data sets. Our velocity resolution is 54 km sec^{-1} while that of Vogt et al. (1995) and Mateo, et al. (1998) is 9 km sec^{-1} . For the case of Leo I, the great velocity dispersion (see Figure 5) as well as the small number of stars observed by Mateo et al. could also contribute to the differences in derived average velocities. As we are more concerned with the deviations from the average rather than the true velocities of the galaxies, we have used our mean velocities for membership determination.

There can be systematic shifts in the radial velocities of stars observed through multi-slit masks (e.g., Tolstoy et al. 2001) if stars are not centered on the slits. Since our computed velocity dispersions are similar to those determined from long slit work, we can assume that our stars were typically well-centered on the slits. There are no obvious correlations between a star's velocity residual from the average v_{helio} and its magnitude, color or radial position within the galaxy.

Of the 121 stars in Leo I, 90 have v_{helio} within 3σ of the average velocity, and all stars have v_{helio} within 5σ . Of the 90 stars observed in Leo II, 83 have v_{helio} within 3σ of the average velocity, and all stars have v_{helio} within 5σ . Figure 5 illustrates the velocity distributions for each galaxy; as no obvious velocity outliers are apparent, we can assume each star observed is a dSph member.

6 CHEMICAL ABUNDANCE ANALYSIS

6.1 The Reduced Equivalent Widths of the Ca II Triplet

The Ca II triplet absorption lines at 8498 , 8542 and 8662 \AA are very strong in spectra of red giant stars, with equivalent widths of order a few Angstroms. Figures 6 and 7 show how the strengths of the Ca II lines compare to strengths of the Fe I lines in low and high-dispersion spectra. The most widely used method of relating the equivalent widths of the Ca II triplet to metallicity is given by Rutledge et al. (1997a and 199b; R97a and R97b, respectively). R97a measured the reduced equivalent widths, W' (defined below) of the Ca II triplet for stars in 52 Globular clusters and, in R97b, found the empirical relationship between W' and $[\text{Fe}/\text{H}]$ for the metallicity scales of Carretta & Gratton (1997, CG97) and Zinn & West (1984, ZW84).

We have followed the R97a definition of sum of the equivalent widths of the Ca II lines,

$$\sum W = 0.5 W_{8498} + W_{8542} + 0.6 W_{8662}. \quad (1)$$

Lower weight is given to the weaker lines to yield higher precision in the final index. The pseudo-equivalent widths and errors of the Ca II lines were measured with an IRAF-based FORTRAN code named EW (G. Da Costa 1999, private comm.). The program assumes the same line window regions used by R97a and the continuum windows used by Armandroff & Zinn (1988).

We were able to measure all three Ca II lines in 155 of the observed spectra, but in 20 spectra we could only accurately measure the equivalent widths of the two strongest lines at 8542 \AA and 8662 \AA due to their lower SNRs. In order to obtain a measurement of $\sum W$ for these stars, we determined the relationship between $\sum W$ and the equivalent widths of the two strongest lines from the cluster stars with high SNR spectra. We found the relationship was linear with

$$\sum W = m (W_{8542} + 0.6 W_{8662}) + b, \quad (2)$$

where $m = 1.104 \pm 0.018$ and $b = 0.138 \pm 0.060 \text{ \AA}$ were the coefficients derived from least-squares fitting analysis that incorporated errors on both values (The data and fit are shown in Figure 8).

The strengths of the Ca II lines are most sensitive to stellar gravity and abundance and much less sensitive to effective temperature (e.g. Díaz, Terlevich & Terlevich 1989, Jorgensen et al. 1992, and Cenarro et al. 2002). Using the “reduced equivalent width”, W' , as defined by Armandroff & Da Costa (1991) allows the effect of gravity to be removed to first order. The reduced equivalent width of a star is defined to be

$$W' = \sum W + 0.64(V - V_{HB}), \quad (3)$$

where V and V_{HB} are the V-band magnitudes of the observed stars and the cluster or dSph horizontal branch, respectively. R97a found a linear relationship existed between $(V - V_{HB})$ and $\sum W$ for stars of an individual globular cluster, and that the slope of $0.64 \pm 0.02 \text{ \AA/mag}$ was insensitive to the metal abundance of the cluster.

In order to tie our W' measurements to the well-calibrated and often utilized scale of R97a, we observed 41 red giants in four Galactic globular clusters. Table 3 lists the clusters, and gives the horizontal branch magnitude, the metallicity, the average W' and error for the cluster from R97a, and the W' from this investigation. Values of W' for NGC 1904 (M79), NGC 4590 (M68), and NGC 6171 (M107) are listed in R97a, but they did not include NGC 5272 in their study. However, B04 observed stars in NGC 5272 in the Ca II recalibration project at the UCO Lick and W.M. Keck Observatories and placed its measurements on the R97a scale. The [Fe/H] values for M79, M68 and M3 listed in Table 3 come from Bosler (2004; see section 6.2) and were determined from atmospheric abundance analysis of Fe II lines in high-dispersion spectra. The [Fe/H] value listed for M107 is from the R97b calibration of W' to [Fe/H] using the Carretta & Gratton (1997, hereafter CG97) metallicity scale. Table 2 lists the individual cluster stars and their measured equivalent widths in this study and in that of R97a/R97b. The data on $\sum W$ for individual stars in the R97a study was provided by J. Hesser (1999, private communication to T. Smecker-Hane). Note that because of geometrical constraints inherent in using slit masks, our sample of cluster stars is not identical to that observed by R97a.

Comparing W' for the 23 individual cluster stars that the two data sets have in common, we find

$$W'_{R97} = 1.006 (\pm 0.025) W'_{LRIS} + 0.267 (\pm 0.063), \quad (4)$$

where W'_{R97} is the value of W' on the scale of R97a and W'_{LRIS} is our observed value. The least-squares fitting technique incorporated the errors in both W'_{LRIS} and W'_{R97} . The data and fits are shown in Figure 9. The small differences in the equivalent widths measured by us and R97a are not surprising, because the spectral resolution of our observations are significantly different (our resolution is 1.55 \AA compared to their resolution of 4 \AA), and the Ca II lines are pressure broadened and partially resolved at this resolution. In addition, the equivalent widths are measured relative to the pseudo-continuum (neither their spectra nor ours were flux calibrated) and thus are slightly sensitive to the spectrograph’s efficiency. The differences we find are comparable to those R97a find between their work and others (e.g., Table 6 in R97a).

The W' values for Leo I and Leo II were determined using V_{HB} values from the literature, and the final W' values were placed on the scale of R97a to remain consistent with other literature on the Ca II triplet. For the Leo I dSph, we assumed

$V_{HB} = 22.60 \pm 0.12 \text{ mag}$ based on the RR Lyrae work of Held, et al. (2001), and for the Leo II dSph, we assumed $V_{HB} = 22.17 \pm 0.14 \text{ mag}$ based on the RR Lyrae work of Siegel & Majewski (2000). Note that V_{HB} does change with the age of a stellar population, but this change is small as long as the ages are $\gtrsim 3 \text{ Gyr}$. This is true for the Leo II dSph, where ages are $\gtrsim 7 \text{ Gyr}$ (Mighell & Rich 1996), but the Leo I dSph does have a few stars as young as $\sim 2 \text{ Gyr}$ (Gallart et al. 1999b, Dolphin 2002). The HB clump in Leo I has a V magnitude that is ~ 0.15 magnitudes brighter than the RR Lyrae stars. Thus adopting the RR Lyrae magnitude will only result in a 0.05 dex systematic metallicity error, in the sense that the true metallicity of a younger stars would be more metal-rich than that inferred. This error is small relative to the other errors, and hence is not taken into account in the present analysis.

Note that although the Ca II lines are easy to observe in low resolution and low signal-to-noise spectra, abundances *cannot accurately be derived from modelling the the Ca II lines* due to the complexity of their formation. Additionally, high dispersion spectra can resolve the weaker iron and neutral calcium lines. These lines can be accurately modelled to derive stellar abundances, but these observations require long exposure times and become impractical for surveying large numbers of faint, distant stars. Thus, if one intends to use observations of the Ca II lines to determine stellar abundances, an empirical relationship must exist between the equivalent widths of the Ca II lines are actual stellar abundances.

6.2 Metallicity Calibration

Though the R97b calibration is widely used to derive abundances from the Ca II triplet, Rut97b points out that the two metallicity scales for which calibrations were derived (CG97 and ZW84) can yield dramatically different values of [Fe/H] for a given W' . Additionally, R97b points out that there is no reason to assume that the relationship should be linear (as in the case of the CG97 metallicity scale) or non-linear (as in the case of the ZW84 metallicity scale). They discussed an apparent non-linearity between the metallicity scales of ZW84 and also of Cohen (compilation in Frogel et al. 1983), who examined more metal-rich stars than were examined in other metallicity literature data. Kraft & Ivans (2004, hereafter KI04) also found a possible non-linearity in the Ca II to [Fe/H] relationship for metal-rich stars in their investigation. In Cole et al. 2004, the effects of line fitting on the equivalent widths of the Ca II lines for metal-rich stars also caused slight shifts in the empirical relationship between Ca II and [Fe/H]. One of the possibilities noted in R97b for a non-linear relationship between W' and [Fe/H] for metal-rich stars is a changing [Ca/Fe] as a function of [Fe/H].

Figure 10 plots [Ca/Fe] versus [Fe/H] for Galactic clusters from B04 and Galactic field stars observed by Edvardsson et al. (1993) and Fulbright (2000, 2002). The [Ca/Fe] in Milky Way stars changes as a function of [Fe/H], and at [Fe/H] ≈ -0.8 , the [Ca/Fe] value to change more rapidly as a function of [Fe/H].

One major problem with determining a standard relationship between Ca II and [Fe/H] for stars with a range of ages and metallicities is that the equivalent widths of the Ca II lines are a function of, among other things, [Ca/H] for RGB stars (see Jorgensen et al. 1992). When one uses the equivalent widths of the Ca II lines to infer [Fe/H], one assumes some constant or smooth [Ca/Fe] relationship. Applying the existing Ca II to [Fe/H] calibration to extragalactic stars is extremely dubious because one must assume that all observed stars have a constant [Ca/Fe] value of approximately 0.3 dex (that of the GGCs).

Bosler (2004) reinvestigated the widely-utilized relationship between W' and $[\text{Fe}/\text{H}]$ for 21 Galactic cluster with a wide range of ages (2 to 14 Gyrs) and metallicities ($-2.5 \leq [\text{Fe}/\text{H}] \leq +0.2$). W' values, as mentioned in the previous section, were measured for stars in the same 21 clusters to build an internally self-consistent data set, and equivalent widths were transformed to the scale of the R97a data because their Ca II measurements are so widely utilized. Figure 11 illustrates the empirical relationship between W' and $[\text{Fe}/\text{H}]$ for the B04 clusters along with the residuals for each of three different fits to the data - a linear fit to only the globular clusters (analogous to the R97b fit to the CG97 metallicity scale) and a linear and quadratic fit to all clusters.

Note that the relationship found by R97b using the metallicity scale of CG97, was based solely on Galactic globular cluster (GGC) stars; the relationship they found, for comparison, was

$$[\text{Fe}/\text{H}]_{\text{CG97}} = -2.66(\pm 0.08) + 0.42(\pm 0.02) \times W'. \quad (5)$$

This fit is similar to the fit to our GGCs (see Table 4). The relationship appears fairly smooth and linear, but the addition of the younger, metal-rich Galactic open clusters (GOCs) with $[\text{Fe}/\text{H}] > -0.8$, indicates that $[\text{Fe}/\text{H}]$ is not truly a linear function of W' . Since most work on the Ca II triplet calibration was done using GGCs, mostly with $[\text{Fe}/\text{H}] < -0.8$, a linear fit is indicated by a solid line in Figure 11. If this calibration based on only the GGCs is used to infer the abundances of the metal-rich open clusters the derived metallicity would be lower by approximately 0.3 dex.

In fact, the relationship is linear up to $[\text{Fe}/\text{H}] \approx -0.08$, but if all of the data are included, the relationship becomes quadratic. The linear fit to only the GGCs, the linear fit to all clusters, and the quadratic fit to all of the clusters are listed in Table 4 along with the mean error of unit weight, m.e.1³, rms and the Chi-squared per degree of freedom, χ_ν^2 , values for the regressions. Notice that linear fit to all of the clusters has the largest m.e.1 value implying that the either the errors have been underestimated or the fit to the W' to $[\text{Fe}/\text{H}]$ relationship is really non-linear and is most likely effected by the varying $[\text{Ca}/\text{Fe}]$ values for the different clusters (ie. it is dependent upon star formation history).

In order to circumvent the fundamental dependence on $[\text{Ca}/\text{Fe}]$ ratios built into the current Ca II calibrations, B04 derived an empirical relationship between Ca II and $[\text{Ca}/\text{H}]$. It is important to note that the $[\text{Ca}/\text{H}]$ values *were not derived from the Ca II lines*. The $[\text{Ca}/\text{H}]$ values were determined from atmospheric abundance analysis of neutral calcium (Ca I) lines measured in high-dispersion spectra. The abundances derived for the Ca I lines were also corrected for non-LTE effects in the analysis. In B04, non-LTE effects on the Ca I, Fe I and Fe II lines were closely examined. These effects on derived abundances arise from the fact that some high energy UV photons from deep within the stellar atmosphere penetrate the upper levels of the atmosphere and break the LTE assumption used in the modelling the line formation. The changes in temperature between the model and the 'true' atmosphere effects the abundances derived by the neutral lines more strongly than the abundances derived by ionized lines. As a result, abundances derived from Fe II lines best represent the 'true' abundances, while

³ The m.e.1 = $(\sum \epsilon^2/\sigma^2)^{0.5} (N-1)^{-0.5}$, where ϵ is the deviation of the $[\text{Fe}/\text{H}]$ value for each cluster from the predicted value based on the fit, σ is the uncertainty in W' and $[\text{Fe}/\text{H}]$ values, N is the total number of clusters. A value of one indicates that the scatter is consistent with the observational errors, and a higher value implies that the errors have been underestimated or that the relationship is nonlinear

those from Fe I and Ca I lines will be effected by the non-LTE atmosphere of the star. However, B04 found that the ratio of Ca I to Fe I ($[\text{Ca}/\text{Fe}]_{\text{I}}$) is not strongly effected by variations in stellar temperatures as both species are being effect similarly. Therefore, the 'true' $[\text{Ca}/\text{H}]$ value was defined as

$$[\text{Ca}/\text{H}] = [\text{Ca}/\text{Fe}]_{\text{I}} + [\text{Fe}/\text{H}]_{\text{II}}, \quad (6)$$

where $[\text{Fe}/\text{H}]_{\text{II}}$ is the iron abundance derived from Fe II lines. This 'true' value of $[\text{Ca}/\text{H}]$ is not affected by the non-LTE effects described above.

The calibration is based on stars in 15 Galactic globular and open clusters with ages from ≈ 2 to 14 Gyr and $-2.2 < [\text{Ca}/\text{H}] < +0.2$ making it an extremely robust calibration of the Ca II triplet to abundances. The regression between W' and $[\text{Ca}/\text{H}]$ is

$$[\text{Ca}/\text{H}] = -2.778(\pm 0.061) + 0.470(\pm 0.016) \text{ dex}/\text{\AA} \times W'. \quad (7)$$

This relationship is independent of the ages of the clusters for clusters older than a few Gyrs. It can be applied to Galactic and extragalactic stars without concern for the effects of variations in $[\text{Ca}/\text{Fe}]$ ratios in the stars. Therefore, it is independent of the star formation history of the system. Additionally, the new calibration includes stars from from both GGCs and GOCs to insure that it is valid over a wide range of ages and metallicities.

Figure 12 shows the linear fit to the calibration with a root-mean-square (rms) scatter of 0.13 dex, an mean error of unit weight (m.e.1) = 1.06. The residual to the fit is also illustrated. The Chi-squared per degree of freedom, $\chi_\nu^2 = 1.87$. We also applied a quadratic fit to the data and found that the coefficient on W'^2 is statistically insignificant compared to the uncertainties in the fit, which are over twice as large. The values of Ca II and $[\text{Ca}/\text{H}]$ for clusters used in the calibration are shown in Table 5. Note that the $[\text{Ca}/\text{H}]$ values listed were derived from atmospheric abundances analysis of high dispersion spectra, while the value of W' were derived from low-dispersion spectra of stars in the same clusters.

6.3 Which is Preferable - A Ca II Calibration to $[\text{Ca}/\text{H}]$ or $[\text{Fe}/\text{H}]$?

As the star formation histories and the effect of galactic winds in the Leo I and Leo II are not yet well-defined, we do not yet know what the element ratio, $[\text{Ca}/\text{Fe}]$, is as a function of metallicity. Thus it would be inappropriate to assume that they follow the same $[\text{Ca}/\text{Fe}]$ verses $[\text{Fe}/\text{H}]$ relationship as that found for the Galactic Globular clusters used by R97 to calibrate the Ca II equivalent widths to $[\text{Fe}/\text{H}]$. The new calibration to $[\text{Ca}/\text{H}]$ has a very small RMS that can be explained mostly by observational error rather than systematic variations that depend on $[\text{Ca}/\text{Fe}]$ and is also independent of stellar ages (for ages ≥ 3 Gyrs) and star formation history. Therefore, the new calcium calibration will be used to derive abundances in this work; however, $[\text{Fe}/\text{H}]$ values on the scale of CG97 will also be listed for reference to those still compelled to use the existing calibration.

As an aside, there is really no compelling reason that stellar metallicities should be specified in terms of $[\text{Fe}/\text{H}]$. The iron abundance became the observational spectroscopist's way of characterizing the overall metallicity of a star in a one-dimensional way, because iron and iron-peak elements are the most plentiful lines and are easiest to measure in optical and near-IR spectra. In fact, stellar opacities are controlled by the entire range of elements; the iron and iron-peak elements whose outer electrons are most easily ionized, but, more importantly, the CNO and alpha-elements, which are most abundant by number highest and which provide the

majority of the transition electrons. Additionally, the abundance ratios [CNO/H] in high metallicity stars is an important parameter because it also controls the amount of energy generated from the CNO cycle.

7 RESULTS

7.1 Metallicity Distribution of Leo I

The observed range in reduced equivalent widths for Leo I dSph stars is $0.83 \leq W' \leq 4.63 \text{ \AA}$. Tables 6 and 8 list the parameters of each star (V, V-B, Ra, Dec, SNR and V_{Helio}) and the spectroscopic values (W' , $[\text{Fe}/\text{H}]_{\text{CG97}}$, and $[\text{Ca}/\text{H}]$), respectively. Note that the W' values have been scaled to the work of R97a, which has been used as a standard in the literature.

As shown in Figure 13, the inferred metallicities range from $-2.39 \leq [\text{Ca}/\text{H}] \leq -0.60$ for 102 stars. The average metallicity is $[\text{Ca}/\text{H}] = -1.34 \pm 0.02$, and the observed spread is 1.20 dex. The median random $[\text{Ca}/\text{H}]$ error is 0.10 dex, and the median total error is 0.17 dex per star. Placing our Ca II values on the $[\text{Fe}/\text{H}]$ scale of CG97, Leo I has a mean $[\text{Fe}/\text{H}]_{\text{CG97}} = -1.34$. Calcium abundances have not been studied extensively in Leo I. However, Shetrone et al. (2003) found $[\text{Ca}/\text{Fe}] = +0.15$ and $+0.02$ dex ($\sigma \approx 0.15$ dex) and $[\text{Fe}/\text{H}] = -1.52$ and -1.06 dex, respectively, ($\sigma \approx 0.1$ dex) for two stars in Leo I based on abundance analysis of high-dispersion spectra. This implies $[\text{Ca}/\text{H}] = -1.20$, which is slightly more metal-rich than the average we found for 102 stars, but the intrinsic spread we see and the small number of stars used by Shetrone et al. could account for the difference.

Suntzeff et al. (1986) found an average metallicity of $[\text{Fe}/\text{H}] = -1.5 \pm 0.25$ from the strengths of the Ca H and K lines in low dispersion spectra of two red giants, and this corresponds to $[\text{Ca}/\text{H}] = -1.41$ assuming an average $[\text{Ca}/\text{Fe}]$ from Shetrone et al. (2003)'s two stars. This value is more metal-poor than the Shetrone et al. value, and it is in agreement with our observed values given the small number of stars used. More recently, Koch et al. (2006b) examined a very similar sample of Leo I stars and derived $[\text{Fe}/\text{H}]$ from the Ca II triplet for 58 red giant stars and found $[\text{Fe}/\text{H}]_{\text{CG97}} = -1.31 \pm 0.02$ and a metallicity spread of 1 dex, which agrees very well with our observations. The lack of overlap between the two data sets does not allow for comparison of individual stars, but the trend in the Leo I abundances is constant between the two data set.

Leo I has a roughly Gaussian-shaped metallicity distribution with an asymmetric over-abundance at the metal-rich end and a slightly extended metal-poor tail. This distribution is very similar to that of Koch et al. (2006b) with a slightly higher resolution due to the larger number of stars used in this sample. We fit the metallicity distribution function with a Gaussian distribution of the form:

$$N(m) \propto \exp\left(-\frac{(m - m_0)^2}{2\sigma_m^2}\right), \quad (8)$$

where $m = [\text{Ca}/\text{H}]$, in order to determine the centroid of the distribution, m_0 , and the observed dispersion, σ_m . For Leo I, a non-linear least-squares fit gives $m_0 = -1.35 \pm 0.02$, and $\sigma_m = 0.24 \pm 0.03$. The fit is shown in Figure 13. Given that the median random measurement error is $\sigma_{\text{rand}} = 0.10 \pm 0.03$ dex, the intrinsic metallicity dispersion in Leo I is equal to

$$\sigma_{m,i} = (\sigma_m^2 - \sigma_{\text{rand}}^2)^{\frac{1}{2}} = 0.26 \pm 0.03 \text{ dex} \quad (9)$$

The implied intrinsic spread in metallicity in Leo I is approximately 2 FWHM = $4.71 \sigma_{m,i} = 1.22 \pm 0.08$ dex.

Figure 14 shows the position of stars in the CMD as a function of their metallicity. The fiducials for the GGCs M5 = NGC 5904 ($[\text{Ca}/\text{H}] = -0.96$, age = 14 Gyr) and M68 ($[\text{Ca}/\text{H}] = -1.78$, age = 14 Gyr) are plotted for reference in the CMD. The most metal-poor stars tend to lie along the blue half of the RGB, but stars with $[\text{Ca}/\text{H}] \gtrsim -1.5$ occupy a wide swath in color. At any given color, there are stars with a mix of metallicities, which probably reflects the fact that the red giants in Leo I have a large range in ages (many Gyrs).

A large spread in metallicity has not been assumed in most studies of the Leo I CMD (Lee, et al. 1993, Gallart, et al. 1999b, Siegel & Majewski 2000), which either assumed a constant metallicity or a much narrower range. Including a 1.2 dex metallicity spread will dramatically affect the inferred star-formation history.

Dolphin (2000) did include metallicity evolution as a variable in his CMD modelling of the Leo I and Leo II CMDs. He photometered archival WFPC2 images and obtained a CMD that spanned the tip of the RGB to the oldest main-sequence turnoff. (The photometric errors at the level of the oldest MSTO are much larger in the Leo I data, and hence the SFH for ages $\gtrsim 9$ Gyr in the Leo I dSph was not as well determined as for the Leo II dSph.) Dolphin modelled the Hess diagram—the density of stars in the CMD—using Padova isochrones (Girardi, et al. 2000), which he interpolated on a finer grid of metallicity (0.15 dex binning). He has kindly provided the simulated data from his best fit models.

We have applied to Dolphin's model CMD the same color and magnitude selection criteria used to select the Leo I spectroscopic sample (note that the color selection did not eliminate any RGB stars), computed the metallicity distribution, and convolved it with our median random $[\text{Ca}/\text{H}]$ errors. The resulting metallicity distribution function is shown in Figure 15. The shapes of the model and observed distributions are similar, with both having slight excesses at the metal-rich end and a metal-poor tail, however, there is a deficiency in metal-poor stars in the model distribution compared to the observations. More recent photometry from Held et al. (2000) indicates a significant metal-poor population based on the existence of an extended blue horizontal branch that had not been previously observed. The exclusion of this metal-poor population in the synthetic CMD used to predict the dispersion may account for the missing metal-poor stars. Interestingly, the peak of the model is significantly more metal-rich than the observed distribution. A Gaussian fit to the model gives $m_0 = -1.0$ and $\sigma_m = 0.17$ dex, although a Gaussian is obviously a poor assumption for this model distribution.

Dolphin did examine $[\text{Fe}/\text{H}]$ values rather than $[\text{Ca}/\text{H}]$, but the peak of the distribution does not account for potential $[\text{Ca}/\text{Fe}]$ differences that may exist in the stars. What could be the cause of the discrepancy? In the CMD modelling, the best fitting values of the metallicity and star-formation rate as a function of time are determined by matching the density of stars in finely-binned magnitude and color intervals in the observed and modelled CMD. In the process, the portions of the CMD with the largest numbers of stars are given the greatest weight. These are the main-sequence turnoff and unevolved main-sequence regions. The width in color of the main-sequence turnoff and upper main sequence is governed by the spread of ages, metallicities, and the assumed fraction and characteristics of unresolved binary systems. A high fraction of binaries causes a spread in the color of the unevolved main sequence, which could be interpreted as an intrinsic spread in metallicity. Thus the assumptions made about the unresolved binaries could affect the inferred distribution of metallicities. In addition, the models themselves could be source of problems because the color-temperature

relationships used to transform from the theoretical to observed plane are still controversial.

More recently, Koch et al. (2006c) examined simple chemical evolution models to the observed Leo I distribution. They used a modified simple closed-box model and a model using Prompt Initial Enrichment scaled to the number of stars they observed. Their model distributions yielded similar average abundances for Leo I, but the closed-box model severely over estimated the metallicity spread while underestimating the number of stars near the center of the distribution. The Prompt Initial Enrichment model did a better job at predicting the height of the distribution peak, but it underestimated the metallicity spread in the galaxy. See in Koch et al. (2006c) (Figure 12) for a more detailed discussion.

7.2 Metallicity Distribution of Leo II

The observed range in the reduced equivalent widths for Leo II stars is $0.36 \leq W' \leq 4.65 \text{ \AA}$. Tables 7 and 9 list the parameters of each star (V, V-B, Ra, Dec, SNR and V_{Heli0}) and the spectroscopic values (W' , $[\text{Fe}/\text{H}]_{\text{CG97}}$, and $[\text{Ca}/\text{H}]$), respectively. Note that the W' values have been scaled to the work of R97a. Figure 16 shows the range in metallicities is $-2.61 \leq [\text{Ca}/\text{H}] \leq -0.59$, and the observed spread is 1.29 dex. The average metallicity in the Leo II dSph is $[\text{Ca}/\text{H}] = -1.65 \pm 0.02$, much more metal-poor than the median in the Leo I dSph. Placing our Ca II values on the $[\text{Fe}/\text{H}]$ scale of CG97, Leo II has a mean $[\text{Fe}/\text{H}]_{\text{CG97}} = -1.59$. The median random error is 0.10 dex and the median total error is 0.17 dex per star, and the intrinsic metallicity dispersion is 1.01 dex. Leo II also has an asymmetric distribution with a steep cut off on the metal-rich end, excesses at the metal-poor end, and an indication of metal-rich and metal-poor tails.

Suntzeff, et al. (1986) found an average $[\text{Fe}/\text{H}] = -1.9 \pm 0.2$ based on the Ca H and K strengths of 3 red giants. With an unknown typical $[\text{Ca}/\text{Fe}]$ value for the Leo II stars, it is impossible to directly compare the two results. However, assuming an average $[\text{Fe}/\text{H}] \approx -1.90$ from Suntzeff and our $[\text{Ca}/\text{H}]$ would imply $[\text{Ca}/\text{Fe}] \approx +0.3$, which is similar to the values for older stars in Milky Way globular clusters and field stars. Mighell & Rich (1996) inferred an average $[\text{Fe}/\text{H}] = -1.60 \pm 0.25$ using the shape of the RGB in the V, I-band CMD. From interpolating globular cluster fiducial RGBs, they derived an intrinsic spread in $[\text{Fe}/\text{H}]$ of 0.9 dex, which is similar to the spread in $[\text{Ca}/\text{H}]$ of 1.0 dex derived here. This agreement is understandable because the color and shape of the RGB are much more sensitive to metallicity than age for ages $\gtrsim 7$ Gyr, the age of the youngest stars in the Leo II dSph. Koch et al. (2006b) observed 52 Leo II stars and found $[\text{Fe}/\text{H}]_{\text{CG97}} = -1.74 \pm 0.02$ and a spread of 1.3 dex. Though the average metallicity is more metal-poor than out observations, the distribution of the stars in both data sets are very similar (see Figure 16 in this paper and Figure 7 in Koch et al. 2006b for comparison).

Figure 17 illustrates the range in $[\text{Ca}/\text{H}]$ across the RGB. Again, the large dispersion in metallicity at a given color indicates the stars span a range of ages.

We also compared the observed metallicity distribution of the Leo II dSph with predictions of CMD modelling from Dolphin (2002). Since both the model and observations have a very non-Gaussian distribution, we did not attempt to compute Gaussian fits. Figures 16 and 18 show that the shape of the model and observed distributions are similar with excesses at the metal-poor end and a steeper drop at the metal-rich end. Leo II is the smaller of the two dSphs, having $M_V = -9.6$ compared to $M_V = -11.9$ for Leo I. The decreased number of stars at high metallicities in Leo II may

be due to its greater inability to retain gas after star formation had progressed for a while. Analyzing the CMD from the same set of WFPC2 images, Mighell & Rich (1996) and Dolphin (2002) both inferred that Leo II stopped forming stars ≈ 7 Gyr ago, compared to the Leo I dSph which only stopped forming stars ~ 2 Gyr ago.

Though the shapes of the distributions are similar, the model has a median which is more metal-rich than the median of the observed distribution. Assuming the $[\text{Ca}/\text{H}]$ from this work and $[\text{Fe}/\text{H}]$ values from Dolphin are taken to be typical values of the Leo II stars, it would imply a $[\text{Ca}/\text{Fe}] \approx -0.49$. The large discrepancy between the abundances derived from CMD modelling and the observations also exists for Leo II stars, and it is even larger than those of the Leo I stars and much lower than the predicted abundance ratios from Type Ia supernovae. Again, if we compare our $[\text{Fe}/\text{H}]_{\text{CG97}}$ values with those of Dolphin, the discrepancy still exists, and is approximately the same size. Though there are no available data on abundance ratio of Leo II, the extremely low $[\text{Ca}/\text{Fe}]$ value from comparing the model results is dramatically different than those derived by comparing $[\text{Ca}/\text{H}]$ to spectroscopic $[\text{Fe}/\text{H}]$ abundances (Shetrone et al. 2003), which yields $[\text{Ca}/\text{Fe}]$ more typical of Galactic and Local Group stars.

Koch et al. (2006b) compared a simple closed-box chemical evolution model (valid only for long-lived stars) with their Leo II distribution and found agreement with central $[\text{Fe}/\text{H}]$ values, but the model severely underestimated the number of stars in the central metallicity range and over estimated the metallicity spread by over estimating the number of metal-poor stars in the galaxy. Additionally, Koch et al. (2006b) compared the models from Lanfranchi and Matteucci (2004) for other Local Group dSphs to the observed Leo II distribution. The Carina, Draco, Sagittarius, Sextans, Sculptor and Ursa Minor dSphs were compared, and they found that Leo II and Carina were the two most similar dSphs in the set using a very simplified comparison. Not surprisingly, they found that the Leo II SFH is as unique and distinct from the other dSphs in the Local Group, reflecting the fact that one global explanation for the formation of these seemingly simple galaxies does not reflect their observed complexities.

8 SUMMARY

We have determined calcium abundances for 102 RGB stars in the Leo I dSph galaxy and 74 RGB stars in the Leo II dSph galaxy using the equivalent widths of the near infrared Ca II triplet lines. The metallicity scale used to convert the Ca II measurements is based on our calibration of Ca II to $[\text{Ca}/\text{H}]$ from Galactic cluster stars with ages from ≈ 2 to 14 Gyr and $-2.2 \lesssim [\text{Ca}/\text{H}] \lesssim +0.2$. Unlike the calibration of Ca II to $[\text{Fe}/\text{H}]$ developed by R97b, the Ca II to $[\text{Ca}/\text{H}]$ is independent of star-to-stars variations in $[\text{Ca}/\text{Fe}]$ with $[\text{Fe}/\text{H}]$. Defying the tradition of using “metallicity” interchangeably with iron abundances, $[\text{Ca}/\text{H}]$ was taken as the relevant metallicity in this investigation.

The Leo I dSph has a average metallicity of $[\text{Ca}/\text{H}] = -1.34 \pm 0.02$ ($\sigma = 0.21$) and an intrinsic spread in metallicity of 1.2 dex. The average metallicity of the Leo II dSph is more metal-poor with $[\text{Ca}/\text{H}] = -1.65 \pm 0.02$ ($\sigma = 0.17$) and has a 1.0 dex spread in metallicity.

The metallicity distribution function is different for the two dSphs. Leo I has an approximately Gaussian distribution with a slight excess at the metal-rich end, while Leo II has a steeper cut-off at the metal-rich end at $[\text{Ca}/\text{H}] \approx -1.4$. The differences in the shape of the distributions may be caused by greater mass loss in

the less massive Leo II dSph, whose star formation ended approximately 7 Gyr ago, compared to the more massive Leo I dSph, whose star formation ended only ~ 1 to 2 Gyr ago. Significant differences, on the order of -0.5 dex, exist between the observed metallicity distribution functions and those derived by sophisticated modelling of Hess diagrams in CMDs obtained with HST. However, the assumption of a Galactic range of $[\text{Ca}/\text{Fe}]$ values show our results to be consistent with the $[\text{Fe}/\text{H}]$ values derived in other spectroscopic and photometric studies.

9 ACKNOWLEDGMENTS

We gratefully acknowledge financial support from the NSF through grant AST-0070895 to T. Smeecker-Hane. T. Bosler would like to thank the ARCS Foundation for a graduate student fellowship and Sigma Xi for a Grant in Aid of Research (2001) as well as ANdy McWilliam, Virginia Trimble, Jay Gallagher and Linda Sparke for their inspiration and interest in this publication. We thank the staff at Keck Observatory, in particular, Paola Amico and Greg Wirth, for their excellent support, and we thank Bev Oke, Judy Cohen and their collaborators for an extremely useful spectrograph. In addition, we extend special thanks to the people of Hawai‘ian ancestry on whose sacred mountain, Mauna Kea, we were privileged to be guests. Our research was expedited by the wide range of data made available at Canadian Astronomy Data Center (CADC), which is part of the Herzberg Institute of Astrophysics, a facility of the National Research Council of Canada. P. Stetson is extremely grateful to Howard E. Bond, Enrico V. Held, Giampaolo Piotto, Edward W. Olszewski, Ivo Saviane, Robert A. Schommer, and Nicholas B. Suntzeff, as well as to the CADC and the Isaac Newton Group Archives, for providing much of the CCD imagery used in this paper.

REFERENCES

- Alcaino, G., Liller, W., Alvarado, F., Wenderoth, E. 1990, AJ, 99, 1831
 Armandroff, T. E. & Zinn, R., 1988, AJ, 96, 92
 Barkana, R. & Loeb, A. ApJ, 523, 54
 Bosler, T.L., 2004 PhD Dissertation, University of California Irvine
 Carretta, E. & Gratton, R. G. 1997, A&AS, 121, 95
 Carney, B.W 1996, PASP, 108, 900
 Catelan, M. 2000, ApJ, 531, 826
 Cenarro, A.J., Gorgas, J., Cardiel, N., Vazdekis, A. & Peletier, R.F. 2002, MNRAS, 329, 863
 Cohen, J. G., Briley, M. M., and Stetson, P. B. 2002, AJ, 123, 2525
 Cudworth, K. M. 1979, AJ, 84, 1312
 Da Costa, G.S. & Armandroff, T.E. 1990, AJ, 100, 162
 D’Antona, F. 2001, in Extragalactic Star Clusters, IAU Symp. 207, eds. E. W. Grebel, D. Geisler & D. Minniti, (ASP: San Francisco), ASP Conf. Series (astro-ph/0105480)
 Díaz, A. I., Terlevich, E., Roberto, T., 1989, MNRAS, 239, 325
 Dean, J.F., Warren, P.R. & Cousins, A.W.J. 1978, 183, 569
 Dolphin, A. E. 2002, MNRAS, 332, 91
 Fulbright, J.P. 2000, AJ, 120, 184
 Fulbright, J.P. 2002, AJ, 123, 404
 Fullton, L.K. 1996, PASP, 108, 545
 Gallart, Carme, Freedman, W. L., Mateo, M., Chiosi, C., Thompson, I. B., Aparicio, A., Bertelli, G., Hodge, P. W., Lee, M. G., Olszewski, E. W., Saha, A., Stetson, P. B., Suntzeff, N. B. 1999a, ApJ, 514, 665
 Gallart, C., Freedman, W. L., Aparicio, A., Bertelli, G. & Chiosi, C. 1999b, ApJ, 118, 2245
 Grebel, E. K. 2000, in *Star Formation from the Small to the Large Scale*, Proc. 33rd ESLAB Symp., ESA SP-445, eds. F. Favata, A.A. Kaas, & Wilson (Noordwijk: ESA), 87 (astro-ph/0007001)
 Girardi, L., Bressan, A., Bertelli, G., & Chiosi, C. 2000, A&AS, 141, 371
 Harris, W. E. 1975, ApJ, 292, 397
 Held, E. V., Saviane, I., Momany, Y. & Carraro, G. 2000, ApJ, 530, L85
 Held, E. V., Clementini, G., Rizzi, L., Momany, Y., Saviane, I., Di Fabrizio, L. ApJ, 562, L39
 Hernandez, X., Gilmore, G., Valls-Gabaud, D. 2000, MNRAS, 317, 831
 Hurley-Keller, D., Mateo, M & Nemeč, J. 1998, AJ, 115, 1840
 Johnson, H. L., Sandage, A. R. 1956, ApJ, 124, 379
 Jorgensen, U.G., Carlsson, M. & Johnson, H. R. 1992, A&A, 254, 258
 Klypin, A. A., Kravtsov, A. V., Valenzuela, O. & Prada, F. 1999, ApJ, 522, 82
 Koch, A., Grebel, E.K., Wyse, R.F.G., Kleyna, J.T., Wilkinson, M.I., Harbeck, D.R., Gilmore, G.F., & Evans, N.W., 2006a, AJ, 131, 895.
 Koch, A., Grebel, E.K., Kleyna, J.T., Wilkinson, M.I., Harbeck, D.R., Gilmore, G.F., Wyse, R.F.G., & Evans, N.W., 2006b AJ in press (astro-ph/06090700)
 Koch, A., Wilkinson, M.I., Kleyna, J.T., Gilmore, G.F., Grebel, E.K., Mackey, A.D., Evans, N.W., & Wyse, R.F.G., 2006c APJ in press (astro-ph/0611372).
 Landolt, A.U. 1992, AJ, 104, 340.
 Lanfranchi, G.A. & Matteucci, F., 2004, MNRAS, 351, 1338.
 Lee, M. G., Freedman, W., Mateo, M., Thompson, I., Roth, M., & Ruiz, M. 1993, AJ, 106, 1420
 Massey, P., Valdes, F., & Barnes, J. 1992, User’s Guide to Reducing Slit Spectra with IRAF (Tucson: NOAO)
 Mateo, M. 1998, ARAA, 36, 435
 Mateo, M., Olszewski, E.W., Vogt, S.S. & Keane, M.J. 1998, AJ, 116, 2315
 McClure, R.D., Hesser, J. E., Stetson, P. B., Vandenberg, D. A. & Bell, R. A. 1987, AJ, 93, 1144
 McWilliam, A. 1997, ARA&A, 35, 503
 Mighell, K. J. & Rich, R. M. 1996, AJ, 111, 777
 Monet, D. G., et al. 1998, USNO-A2.0 Catalog (Flagstaff: USNO)
 Oke, J.B., Cohen, J.G., Carr, M., Cromer, J., Dungizian, A., Harris, F. H., Labrecque, S., Lucinio, R. & Schall, W. 1995, PASP, 107, 375
 Osterbrock, D.E. et al. 1996, PASP, 108, 277
 Obserbrock, D.E. & Fulbright, J.P. 1997, PASP, 109, 614
 Rutledge, G. A., Hesser, J. E., & Stetson, P. B., Mateo, M., Simard, L., Bolte, M., Friel, E. D., Copin, Y. 1997, PASP 109 883 (Rut97a)
 Rutledge, G. A., Hesser, J. E., & Stetson, P. B. 1997, PASP, 109, 907 (Rut97b)
 Sandquist, E. L., Bolte, M.; Stetson, P. B.; Hesser, J. E. 1996, ApJ, 470, 910
 Salaris, M., Chieffi, A., & Straniero, O. 1992, ApJ, 414, 580
 Schlegel, A. J., Finkbeiner, D. P., & Davies, M. 1998, ApJ, 500, 525
 Shetrone, M.D., Côte, P., & Sargent, W.L.W. 2001, ApJ, 548, 592
 Siegel, M.H. & Majewski, S.R. 2000, AJ, 120, 284
 Smeecker-Hane, T. A. & McWilliam, A. 1999, in *Spectro-Photometric Dating of Stars and Galaxies*, eds. I. Hubeny, S. Heap & R. Cornett, (ASP: San Francisco), ASP Conf. Series, vol. 192, 150
 Smeecker-Hane, T. A., Stetson, P. B., Hesser, J. E. & Vandenberg, D. A., 1996, in *From Stars to Galaxies: The Impact of Stellar Physics on Galaxy Evolution*, eds. C. Leitherer, U. Fritze-von Alvensleben and J. Huchra, (ASP: San Francisco), ASP Conf. Series, 98, 328 (astro-ph/9601020)
 Smeecker-Hane, T. A., Mandushev, G., Hesser, J. E., Stetson, P. B., Da Costa, G. S. & Hatzidimitriou, D. 1999, in *Spectro-Photometric Dating of Stars and Galaxies*, eds. I. Hubeny, S. Heap & R. Cornett, (ASP: San Francisco), ASP Conf. Series, vol. 192, 150 (astro-ph/9910211)
 Sneden, C., Kraft, R.P., Shetrone, M.D., Smith, G.H., Langer, G.E. & Prosser, C.F. 1997, AJ, 114, 1964
 Stetson, P.B. 2000, PASP, 112, 925
 Stetson, P.B. & Harris, W.E. 1977, AJ, 82, 854
 Stetson, P. B., Hesser, J. E., & Smeecker-Hane, T. A. 1998, PASP, 110, 533
 Thielemann, F.-K., Nomoto, K. & Yokoi, K. 1986, A&A, 158, 17
 Timmes, F.X., Woosley, S.E., & Weaver, T.A. 1995, ApJS, 98, 617
 Tonry, J. & Davis, M. 1979, AJ, 84, 1511
 Tolstoy, E. 1996, ApJ, 462, 684

Tolstoy, E., Irwin, M. J., Cole, A. A., Pasquini, L., Gilmozzi, R., & Gal-
lagher, J. S. 2001, MNRAS, 327, 918

Vogt, S.S., Mateo, M.M., Olszewski, E.W. & Keane, M.J. 1995, AJ, 109,
151

Wheeler, J.C., Sneden, C., & Truran, J.W. 1989, ARA&A, 27, 279

Zinn, R. & West, M.J. 1984, ApJS, 55, 45

Table 1. Galaxy Properties

	Leo I	Leo II	
Right Ascension (J2000)	$\alpha = 10:08.5$	$\alpha = 11:13.5$	1
Declination (J2000)	$\delta = +12:18.5$	$\delta = +22:09.2$	1
Total Absolute Magnitude, M_V (mag)	-11.9	-9.6	1
Core and Tidal Radii (arcmin)	3.3, 12.6	2.9, 8.7	1
Distance (kpc)	273	204	2, 3
Distance Modulus, $(m - M)_0$ (mag)	22.18	21.55	2, 3
Horizontal Branch Magnitude, V_{HB} (mag)	22.70	22.17	4, 5
Foreground Reddening, $E(B-V)$ (mag)	0.040	0.027	6, 3

(1) Mateo 1998; (2) Lee, et al. 1993; (3) Mighell & Rich 1998; (4) Held, et al. 2001; (5) Siegel & Majewski 2000; (6) Schlegel, Finkbeiner & Davis 1998.

Table 2. Galactic Globular Cluster Stars

Cluster-Star ID	$V - V_{HB}$ (mag)	$\sum W$ (\AA)	$\sigma_{\sum W}$ (\AA)	$\sum W_{\text{Rut97a}}$ (\AA)	$\sigma_{W \sum_{\text{Rut97a}}}$ (\AA)	Ref.
NGC 1904 - 52	-2.09	3.84	0.12	4.15	0.15	1, 2
NGC 1904 - 131	-2.54	4.27	0.17	4.71	0.14	1, 2
NGC 1904 - 223	-2.96	4.25	0.15	4.80	0.16	1, 2
NGC 1904 - 160	-3.13	4.13	0.15	—	—	1, 2
NGC 1904 - 181	-2.20	3.72	0.11	—	—	1, 2
NGC 1904 - 89	-1.44	3.61	0.10	—	—	1, 2
NGC 1904 - 241	-2.54	4.36	0.16	—	—	1, 2
NGC 1904 - 294	-1.93	3.97	0.14	—	—	1, 2
NGC 4590 - AL81	-1.89	2.90	0.16	2.64	0.07	3, 5
NGC 4590 - HI239	-1.42	2.31	0.07	2.62	0.07	4, 5
NGC 4590 - HI119	-2.04	2.44	0.05	2.76	0.06	4, 5
NGC 4590 - HQ ^a	-2.11	2.56	0.07	3.00	0.04	4, 5
NGC 4590 - HII47	-0.55	2.18	0.13	2.36	0.10	4, 5
NGC 4590 - HII28	-1.97	2.90	0.05	2.99	0.06	4, 5
NGC 4590 - HI30	-1.53	2.50	0.10	2.70	0.07	4, 5
NGC 4590 - HI35	-1.13	2.33	0.11	2.24	0.10	4, 5
NGC 4590 - 38	-1.11	2.12	0.05	—	—	5, 6
NGC 4590 - 31	-1.32	2.23	0.06	—	—	5, 6
NGC 4590 - 36	-1.10	2.13	0.04	—	—	5, 6
NGC 4590 - 22 ^a	-1.59	4.58	0.13	—	—	5, 6
NGC 4590 - HI82	-2.99	3.26	0.08	—	—	4, 5
NGC 4590 - 23	-1.48	2.14	0.05	—	—	5, 6
NGC 4590 - A53	-2.78	2.98	0.08	—	—	3, 5
NGC 4590 - HI49	-1.08	1.84	0.11	—	—	4, 5
NGC 5272 - 265	-2.39	4.541	0.137	4.47	0.12	7, 8
NGC 5272 - 334	-2.41	4.487	0.127	4.73	0.16	7, 8
NGC 5272 - 640	-2.38	4.488	0.126	4.28	0.07	7, 8
NGC 5272 - 885	-2.18	4.073	0.118	4.31	0.11	7, 8
NGC 5272 - 1217	-1.65	4.115	0.091	—	—	7, 8
NGC 5272 - 589	-2.78	4.624	0.129	—	—	7, 8
NGC 5272 - 250	-1.54	3.965	0.111	—	—	7, 8
NGC 5272 - 238	-3.03	4.679	0.099	—	—	7, 8
NGC 5272 - 345 ^a	-2.19	4.513	0.124	—	—	7, 8
NGC 6171 - SL	-1.66	5.00	0.16	4.75	0.11	5, 6
NGC 6171 - SR	-1.04	4.25	0.14	4.27	0.14	5, 6
NGC 6171 - S62	-1.73	4.81	0.14	5.13	0.07	5, 6
NGC 6171 - SF	-2.31	5.08	0.13	5.45	0.09	5, 6
NGC 6171 - SS	-0.91	4.72	0.16	4.88	0.15	5, 6
NGC 6171 - SU	-0.92	4.04	0.10	4.44	0.22	5, 6
NGC 6171 - SH	-1.86	5.01	0.14	5.16	0.09	5, 6
NGC 6171 - S203	-0.48	4.08	0.14	4.61	0.19	5, 6

NOTES: a: A non-member based upon its radial velocity

References:

- (1) ID: Stetson & Harris 1977
- (2) Photometry: Stetson & Harris 1977
- (3) ID: Alcaino & Liller 1990
- (4) ID: Harris 1975
- (5) Photometry: Stetson, P.B., private comm.
- (6) ID: Stetson, P.B., private comm.
- (7) ID: Johnson & Sadage 1956
- (8) Photometry: Cudworth 1979

Table 3. The Calibrating Globular Clusters

Cluster	V_{HB} (mag)	[Fe/H]	W'_{Rut} (Å)	$\sigma_{W'_{\text{Rut}}}$ (Å)	W' (Å)	$\sigma_{W'}$ (Å)	N
NGC 1904 = M79	16.15	-1.52	3.09	0.12	2.51	0.05	8
NGC 4590 = M68	15.68	-2.30	1.59	0.08	1.32	0.03	9
NGC 5272 = M3	15.65	-1.55	3.07	0.08	2.91	0.05	8
NGC 6171 = M107	15.70	-0.95	3.99	0.08	3.71	0.05	8

Table 4. Regressions for W' to Fe II Results

Line Style	$[\text{Fe}/\text{H}] = A + B * W' + C * W'^2$								
	A (dex)	σ_A	B (dex/Å)	σ_B	C (dex/Å) ²	σ_C	m.e.1	rms	χ^2
Dashed	-2.985	0.256	+0.329	0.145	+0.029	0.019	1.27	0.14	0.04
Dot-dash	-3.340	0.055	+0.549	0.015	1.40	0.18	4.52
Solid	-3.078	0.058	+0.440	0.020	1.25	0.10	0.31
KI03 ^a	-3.225	0.082	+0.537	0.024

Dot-dash=linear fit, Dashed=quadratic fit, Solid=linear fit to GGCs only

^a: Indicates the fit from KI03 based on Fe II abundances

Table 5. Abundances and Reduced Equivalent Widths for Clusters used in the Ca II \rightarrow [Ca/H] Calibration from Bosler, 2004

Group #	NGC #	Alt. ID	W' (Å)	$\sigma_{W'}$ (Å)	# of Stars	[Fe/H]	$\sigma_{[\text{Fe}/\text{H}]}$	[Ca/H]	$\sigma_{[\text{Ca}/\text{H}]}$	# of Stars
1	104	47 Tuc	4.53 ^b	0.07	31	-0.64	0.04	-0.50	0.04	12
	288		3.86	0.08	10	-1.53	0.06	-1.11	0.13	2
	1904	M79	3.14 ^b	0.14	9	-1.52	0.04	-1.24	0.07	6
	4590	M68	1.59 ^b	0.08	19	-2.30	0.04	-2.01	0.05	7
	5272	M3	3.10	0.07	9	-1.58	0.04	-1.31	0.06	6
	5904	M5	3.73 ^b	0.12	43	-1.38	0.06	-0.99	0.09	4
	6341	M92	1.77	0.08	6	-2.43	0.04	-2.04	0.06	7
	6638		4.31 ^b	0.12	12	-1.26	0.05	-0.98	0.08	4
	7089	M2	3.26	0.07	11	-1.72	0.08	-1.36	0.10	4
	7099	M30	1.89	0.09	5	-2.22	0.04	-1.83	0.06	5
2 ^a	6121	M4	3.87 ^b	0.07	33	-1.37	0.11	-1.11	0.11	24
	6254	M10	3.42 ^b	0.09	16	-1.67	0.11	-1.38	0.09	9
	6397		2.17 ^b	0.08	19	-2.11	0.11	-1.91	0.11	6
	6752		3.41 ^b	0.07	14	-1.72	0.12	-1.46	0.11	8
	6838	M71	4.64 ^b	0.17	11	-1.09	0.11	-0.66	0.09	10
	7078	M15	1.56 ^b	0.12	6	-2.45	0.11	-2.16	0.09	7
3	2141		5.41	0.09	10	-0.46	0.11	-0.42	0.11	5
	2420		5.21	0.10	6	-0.33	0.13	-0.41	0.14	3
	2682	M67	5.62	0.10	8	+0.03	0.10	-0.08	0.09	6
	6791		6.50	0.11	8	+0.07	0.29	+0.02	0.24	2
	7789		5.32	0.10	8	-0.37	0.11	-0.41	0.12	3

^a: The [Ca/H] values for Group 2 clusters have been derived using the [Ca/Fe] value found in the literature: Ivans et al. (1999) for M4, Kraft et al. (1995) for M10, Castillo et al. (2000) for N6397, Cavallo et al. (2004) for N6752, Ramirez et al. (2002) for M71 and Sneden et al. (1997) for M15. Since these values have not been transformed to the scale of this work, the calcium values are listed here but were not used in the final [Ca/H] calibration of the Ca II triplet.

^b: W' and $\sigma_{W'}$ come from R97a.

Table 6: Parameters for Stars in the Leo I dSph

ID	V (mag)	B-V (mag)	RA (J2000)	DEC (J2000)	SNR	v_{helio} (km/sec)
2195	19.78	1.45	10:7:59.14	12:17:17.6	18	303.0
2405	20.40	1.14	10:8:01.21	12:16:14.7	11	280.9
2488	19.92	1.33	10:8:01.89	12:17:55.6	26	287.1
2557	20.13	1.32	10:8:02.49	12:16:19.8	14	278.8
2655	20.30	1.39	10:8:03.24	12:19:11.0	17	282.7
2767	20.22	1.22	10:8:04.00	12:19:41.6	16	297.6
2907	20.20	1.20	10:8:04.91	12:17:53.3	17	279.1
3135	20.20	1.12	10:8:06.28	12:17:45.1	19	270.6
3499	20.15	1.33	10:8:08.02	12:19:24.3	16	281.9
3994	19.88	1.31	10:8:09.96	12:16:25.4	17	287.9
4173	20.08	1.12	10:8:10.59	12:17:07.9	19	257.6
4690	20.16	1.36	10:8:12.12	12:17:12.4	15	270.3
5496	19.89	1.01	10:8:14.19	12:17:36.1	18	302.9
6065	19.81	1.47	10:8:15.41	12:19:01.4	34	279.2
6119	20.16	1.29	10:8:15.52	12:16:41.8	16	300.0
6372	20.30	1.09	10:8:16.08	12:19:22.7	23	265.6
6581	20.25	1.10	10:8:16.48	12:15:51.4	15	296.1
6849	19.88	0.95	10:8:16.97	12:18:28.3	26	293.0
7239	20.21	1.13	10:8:17.61	12:16:30.4	22	266.4
7548	19.92	1.23	10:8:18.14	12:17:46.2	25	270.3
7752	20.23	1.01	10:8:18.47	12:19:51.1	12	241.5
7975	20.26	1.13	10:8:18.82	12:19:50.9	26	269.9
7984	20.15	1.18	10:8:18.83	12:19:04.5	13	274.1
8203	19.91	1.32	10:8:19.16	12:20:48.7	21	281.9
8391	20.26	1.01	10:8:19.44	12:16:34.2	13	282.1
8409	20.11	1.21	10:8:19.47	12:19:09.7	14	273.8
8608	19.76	1.27	10:8:19.75	12:16:55.0	33	298.8
8635	20.32	1.08	10:8:19.79	12:16:34.2	13	282.1
8885	19.65	1.13	10:8:20.13	12:17:02.8	27	288.0
8893	20.18	0.94	10:8:20.15	12:17:47.0	16	286.1
8937	19.78	1.08	10:8:20.21	12:17:56.0	14	266.8
9099	20.33	1.07	10:8:20.45	12:16:01.7	21	283.4
9187	20.24	0.98	10:8:20.55	12:15:47.2	14	263.7
9241	20.33	1.19	10:8:20.63	12:19:21.0	14	276.6
9683	19.93	1.36	10:8:21.23	12:17:41.3	15	283.5
9764	19.83	1.35	10:8:21.34	12:19:52.6	12	284.3
9782	19.56	1.17	10:8:21.36	12:16:22.8	23	279.7
9915	19.68	1.33	10:8:21.55	12:19:12.9	35	283.0
10190	20.09	1.30	10:8:21.87	12:19:33.2	17	271.2
10439	20.01	1.21	10:8:22.22	12:21:39.5	18	279.1
10670	20.12	1.21	10:8:22.50	12:22:40.1	26	275.6
10789	19.91	1.28	10:8:22.65	12:17:21.5	18	252.8
10914	19.80	1.19	10:8:22.80	12:17:59.9	29	290.3
11712	20.43	1.10	10:8:23.77	12:15:43.9	18	295.0
11758	19.63	1.20	10:8:23.83	12:17:10.7	36	273.6
11808	19.69	1.28	10:8:23.89	12:17:37.3	23	290.0
12171	20.33	0.89	10:8:24.35	12:18:27.4	11	296.4
12351	19.78	1.21	10:8:24.54	12:17:42.1	22	288.2
12515	19.87	1.40	10:8:24.71	12:17:24.2	28	276.0
12581	20.24	1.17	10:8:24.81	12:15:54.6	19	269.1
13094	20.02	1.37	10:8:25.39	12:16:53.3	18	284.1
13137	20.01	1.29	10:8:25.43	12:17:16.6	26	245.9
13158	19.88	1.24	10:8:25.46	12:16:36.3	25	288.6
13415	20.13	1.48	10:8:25.74	12:21:01.9	13	285.2
14095	19.81	1.34	10:8:26.49	12:19:11.2	34	279.6
14307	20.53	1.19	10:8:26.71	12:16:36.4	16	275.7

continued on next page

Table 6: Leo I *continued*

ID	V (mag)	B-V (mag)	RA (J2000)	DEC (J2000)	SNR	v_{helio} (km/sec)
14738	19.92	0.84	10:8:27.16	12:17:56.8	14	284.6
14927	19.73	1.25	10:8:27.36	12:16:17.6	23	282.6
16048	19.79	1.13	10:8:28.56	12:19:08.0	14	295.2
16088	20.12	1.20	10:8:28.59	12:16:20.6	25	280.8
16219	19.64	1.19	10:8:28.76	12:17:55.1	25	284.0
16248	20.33	1.05	10:8:28.79	12:20:33.6	16	272.8
16334	19.90	1.21	10:8:28.89	12:19:27.8	18	291.6
16635	19.78	1.25	10:8:29.20	12:16:12.2	33	283.3
17009	19.82	1.36	10:8:29.60	12:18:07.5	32	289.7
17226	20.32	1.13	10:8:29.86	12:19:14.6	22	298.1
17437	20.12	0.96	10:8:30.08	12:18:12.6	15	265.3
17620	20.40	0.98	10:8:30.29	12:17:13.5	12	300.6
17854	19.74	1.11	10:8:30.56	12:16:27.5	34	293.8
18030	19.56	1.12	10:8:30.76	12:17:29.8	26	285.6
18214	19.77	1.35	10:8:30.97	12:16:40.6	27	286.4
18315	19.69	1.28	10:8:31.09	12:18:35.8	30	270.8
18323	20.08	0.94	10:8:31.09	12:18:02.6	21	298.4
18509	20.03	1.19	10:8:31.31	12:20:21.9	19	297.2
18588	19.87	1.46	10:8:31.40	12:15:55.8	26	288.6
18676	20.44	1.14	10:8:31.50	12:21:49.1	13	274.4
18765	20.03	1.34	10:8:31.58	12:17:26.4	24	287.0
18801	19.74	1.29	10:8:31.62	12:18:50.3	18	287.5
18812	20.13	1.13	10:8:31.64	12:16:52.4	16	293.0
18880	20.05	1.16	10:8:31.71	12:18:38.6	11	271.7
19040	20.08	1.20	10:8:31.88	12:22:30.9	14	291.4
19080	19.71	1.18	10:8:31.93	12:18:41.9	31	275.1
19262	20.11	1.22	10:8:32.14	12:18:38.5	11	293.9
19667	19.73	1.22	10:8:32.62	12:18:09.0	31	265.8
19881	20.02	1.15	10:8:32.87	12:17:35.2	27	290.1
20470	19.75	1.18	10:8:33.57	12:18:25.7	28	279.5
20882	19.96	1.33	10:8:34.06	12:23:16.7	15	275.8
21026	20.06	1.23	10:8:34.24	12:16:11.4	16	292.1
21192	20.28	1.19	10:8:34.45	12:21:23.0	14	286.8
21196	20.54	1.13	10:8:34.46	12:20:06.5	11	302.1
21325	19.70	1.33	10:8:34.64	12:18:56.2	26	297.3
21348	20.29	1.11	10:8:34.67	12:17:16.7	33	270.4
22001	20.35	1.20	10:8:35.55	12:16:59.1	23	279.1
22513	20.07	1.30	10:8:36.25	12:19:12.1	26	298.3
22788	19.73	1.34	10:8:36.65	12:17:50.6	11	271.5
23074	20.08	1.25	10:8:37.06	12:16:56.3	23	282.2
23518	20.35	0.99	10:8:37.68	12:19:49.6	18	267.9
24095	20.26	0.99	10:8:38.65	12:18:51.8	17	263.8
25113	19.70	1.38	10:8:40.45	12:16:37.9	26	287.1
25440	20.38	0.90	10:8:41.10	12:17:36.5	17	292.1
25820	20.20	1.23	10:8:41.92	12:18:39.5	21	251.9

Table 7: Parameters for Stars in the Leo I dSph

ID	V (mag)	B-V (mag)	RA (J2000)	DEC (J2000)	SNR	v_{helio} (km/sec)
156	18.58	1.79	11:13:20.9	22:08:22.9	19	103.2
166	18.87	1.17	11:13:38.9	22:10:18.2	38	92.7
180	19.08	1.47	11:13:23.2	22:10:55.9	42	84.7
195	19.08	1.08	11:13:33.2	22:08:12.5	36	88.2
209	19.16	1.42	11:13:31.1	22:06:30.4	42	98.6
230	19.23	1.41	11:13:34.8	22:09:42.4	27	108.0
233	19.22	1.34	11:13:24.5	22:06:13.5	18	75.6
234	19.26	1.21	11:13:20.8	22:08:34.4	21	75.1
235	19.24	1.44	11:13:23.4	22:08:54.3	22	94.6
236	19.21	1.37	11:13:40.5	22:12:18.4	37	101.1
237	19.26	1.04	11:13:39.8	22:10:23.1	30	100.0
248	19.31	1.20	11:13:27.7	22:10:13.0	29	98.7
249	19.32	1.16	11:13:19.3	22:07:41.6	22	106.8
254	19.35	1.34	11:13:32.1	22:07:29.8	34	84.8
255	19.30	1.35	11:13:34.5	22:11:42.5	38	86.7
256	19.34	1.23	11:13:27.7	22:10:39.7	30	99.7
258	19.35	1.35	11:13:19.8	22:09:20.3	37	91.1
259	19.35	1.37	11:13:30.8	22:10:51.0	18	100.2
260	19.32	1.29	11:13:26.6	22:07:26.3	33	113.4
271	19.37	1.37	11:13:19.9	22:09:45.9	40	74.2
277	19.39	1.26	11:13:37.8	22:09:27.2	22	85.2
280	19.45	1.12	11:13:23.8	22:05:32.8	28	90.7
281	19.42	1.09	11:13:32.7	22:07:04.7	35	82.1
282	19.38	1.48	11:13:39.5	22:09:16.8	34	95.3
285	19.43	1.31	11:13:33.9	22:06:08.2	34	79.3
293	19.37	1.29	11:13:25.7	22:06:37.8	37	60.4
296	19.46	1.05	11:13:21.4	22:10:37.7	35	64.6
302	19.46	1.17	11:13:30.9	22:08:11.5	30	117.2
304	19.47	1.25	11:13:30.3	22:06:57.6	35	82.9
320	19.47	1.30	11:13:29.7	22:06:46.5	18	87.3
331	19.56	1.12	11:13:37.1	22:09:33.2	33	101.7
333	19.56	1.20	11:13:26.5	22:11:07.4	33	76.4
336	19.56	1.18	11:13:23.3	22:10:05.2	37	91.0
341	19.59	1.24	11:13:29.6	22:08:57.7	32	87.4
351	19.59	1.25	11:13:31.0	22:11:21.9	39	79.1
352	19.55	1.36	11:13:23.1	22:10:22.6	17	92.4
370	19.64	0.93	11:13:33.3	22:09:44.3	21	88.2
377	19.65	1.19	11:13:29.6	22:07:16.1	27	84.3
379	19.67	1.29	11:13:31.2	22:08:24.6	33	72.5
392	19.70	1.13	11:13:28.8	22:08:47.0	12	106.0
395	19.73	1.14	11:13:33.1	22:07:37.6	23	91.7
396	19.71	0.95	11:13:27.9	22:08:15.4	18	85.2
397	19.73	1.17	11:13:34.5	22:08:09.8	19	80.6
402	19.74	1.19	11:13:31.0	22:08:44.6	24	86.5
409	19.74	1.06	11:13:27.9	22:08:29.5	11	78.5
420	19.82	1.11	11:13:30.9	22:09:32.6	28	79.7
422	19.79	1.10	11:13:16.6	22:08:58.9	21	80.0
429	19.73	1.22	11:13:25.6	22:07:44.1	19	79.4
430	19.79	1.18	11:13:28.5	22:08:43.2	19	79.9
432	19.83	0.97	11:13:15.5	22:09:00.9	14	82.4
434	19.81	1.14	11:13:31.7	22:07:46.8	21	67.0
435	19.78	1.20	11:13:36.0	22:12:20.8	21	99.5
441	19.83	1.01	11:13:31.6	22:08:34.2	20	88.4
471	19.88	0.95	11:13:38.5	22:09:47.3	12	90.4
493	19.96	1.04	11:13:35.9	22:09:27.7	16	99.5
495	19.95	1.14	11:13:32.5	22:11:22.8	22	92.7

continued on next page

Table 7: Leo I *continued*

ID	V (mag)	B-V (mag)	RA (J2000)	DEC (J2000)	SNR	v_{helio} (km/sec)
508	19.97	1.11	11:13:23.7	22:07:07.2	22	86.9
524	20.04	1.18	11:13:35.1	22:11:34.7	17	95.6
526	20.06	1.12	11:13:36.2	22:10:18.6	16	86.9
533	20.06	1.03	11:13:26.8	22:08:24.8	15	70.7
541	20.10	1.08	11:13:23.7	22:09:12.6	15	60.7
549	20.13	1.07	11:13:18.2	22:08:29.3	15	88.5
552	20.15	1.01	11:13:32.8	22:10:53.3	22	103.5
556	20.14	1.00	11:13:38.0	22:11:17.4	13	105.4
558	20.20	0.95	11:13:23.3	22:05:23.3	24	57.9
569	20.15	1.06	11:13:23.4	22:06:18.1	22	85.3
570	20.17	1.09	11:13:34.7	22:11:01.9	12	111.8
573	20.18	1.16	11:13:36.2	22:08:51.2	24	92.6
576	20.20	1.04	11:13:30.5	22:08:24.9	16	86.0
584	20.20	1.04	11:13:32.3	22:06:55.9	17	78.6
588	20.22	1.00	11:13:33.8	22:10:03.3	15	83.6
604	20.24	1.05	11:13:37.9	22:08:13.3	14	74.2
614	20.30	0.99	11:13:34.5	22:11:05.5	18	86.9
623	20.26	1.22	11:13:26.1	22:06:48.2	17	83.0

Table 8: Spectroscopic Data for Stars in the Leo I dSph

ID	W'_{α} (Å)	$\sigma_{W'}$ (Å)	[Fe/H] CG97	$\sigma_{[\text{Fe}/\text{H}]}$ Total	$\sigma_{[\text{Fe}/\text{H}]}$ Random	[Ca/H]	$\sigma_{[\text{Ca}/\text{H}]}$ Total	$\sigma_{[\text{Ca}/\text{H}]}$ Random
2195	3.76	0.20	-1.08	0.16	0.08	-1.01	0.15	0.09
2405	3.17	0.30	-1.33	0.21	0.11	-1.29	0.22	0.14
2488	2.92	0.19	-1.43	0.15	0.06	-1.41	0.15	0.09
2557	2.90	0.23	-1.44	0.17	0.08	-1.42	0.17	0.11
2655	1.99	0.21	-1.82	0.16	0.07	-1.84	0.16	0.10
2767	2.50	0.24	-1.61	0.18	0.09	-1.60	0.18	0.11
2907	2.84	0.22	-1.47	0.17	0.08	-1.44	0.16	0.10
3135	3.03	0.24	-1.39	0.18	0.09	-1.35	0.18	0.11
3499	3.79	0.23	-1.07	0.17	0.09	-1.00	0.17	0.11
3994	2.59	0.19	-1.57	0.15	0.06	-1.56	0.15	0.09
4173	2.77	0.21	-1.50	0.16	0.07	-1.48	0.16	0.10
4690	3.81	0.26	-1.06	0.19	0.10	-0.99	0.19	0.12
5496	2.50	0.22	-1.61	0.17	0.08	-1.60	0.16	0.10
6065	3.50	0.19	-1.19	0.15	0.07	-1.13	0.15	0.09
6119	2.56	0.22	-1.58	0.17	0.08	-1.57	0.16	0.10
6372	1.86	0.20	-1.88	0.15	0.06	-1.90	0.15	0.09
6581	3.66	0.36	-1.12	0.25	0.15	-1.06	0.26	0.17
6849	2.34	0.23	-1.68	0.17	0.08	-1.68	0.17	0.11
7239	2.58	0.19	-1.57	0.15	0.06	-1.57	0.15	0.09
7548	4.04	0.23	-0.96	0.17	0.09	-0.88	0.17	0.11
7752	1.77	0.28	-1.92	0.20	0.10	-1.95	0.20	0.13
7975	3.64	0.21	-1.13	0.16	0.08	-1.07	0.16	0.10
7984	3.85	0.20	-1.04	0.16	0.07	-0.97	0.15	0.09
8203	3.72	0.20	-1.10	0.16	0.07	-1.03	0.15	0.09
8391	2.92	0.35	-1.41	0.15	0.12	-1.41	0.25	0.16
8409	3.09	0.24	-1.36	0.18	0.09	-1.33	0.18	0.11
8608	2.83	0.24	-1.47	0.18	0.09	-1.45	0.18	0.11
8635	3.13	0.23	-1.13	0.22	0.11	-1.31	0.17	0.11
8885	2.22	0.21	-1.73	0.16	0.07	-1.73	0.16	0.10
8893	3.58	0.26	-1.16	0.19	0.10	-1.10	0.19	0.12
8937	4.21	0.28	-0.89	0.20	0.11	-0.80	0.20	0.13
9099	3.40	0.20	-1.23	0.16	0.07	-1.18	0.15	0.09
9187	3.28	0.28	-1.28	0.20	0.11	-1.24	0.20	0.13
9241	2.84	0.24	-1.47	0.18	0.09	-1.44	0.18	0.11
9683	3.01	0.22	-1.40	0.17	0.08	-1.36	0.17	0.10
9764	2.40	0.29	-1.65	0.21	0.11	-1.65	0.21	0.14
9782	2.25	0.18	-1.71	0.15	0.05	-1.72	0.14	0.08
9915	3.95	0.21	-1.00	0.16	0.08	-0.92	0.16	0.10
10190	2.70	0.21	-1.53	0.16	0.07	-1.51	0.16	0.10
10439	3.27	0.19	-1.28	0.15	0.07	-1.24	0.15	0.09
10670	3.40	0.23	-1.23	0.17	0.08	-1.18	0.17	0.11
10789	3.36	0.22	-1.25	0.17	0.08	-1.20	0.17	0.10
10914	3.09	0.21	-1.36	0.16	0.07	-1.33	0.16	0.10
11712	2.25	0.26	-1.72	0.19	0.09	-1.72	0.19	0.12
11758	2.70	0.19	-1.53	0.15	0.06	-1.51	0.15	0.09
11808	3.45	0.20	-1.21	0.16	0.07	-1.16	0.15	0.09
12171	3.24	0.30	-1.30	0.21	0.12	-1.26	0.22	0.14
12351	3.00	0.22	-1.40	0.17	0.08	-1.37	0.17	0.10
12515	2.80	0.24	-1.49	0.18	0.09	-1.46	0.18	0.11
12581	3.02	0.20	-1.39	0.16	0.07	-1.36	0.15	0.09
13094	2.87	0.21	-1.45	0.16	0.07	-1.43	0.16	0.10
13137	3.21	0.22	-1.31	0.17	0.08	-1.27	0.17	0.10
13158	3.78	0.21	-1.07	0.16	0.08	-1.00	0.16	0.10
13415	3.04	0.21	-1.38	0.16	0.07	-1.35	0.16	0.10
14095	3.19	0.17	-1.32	0.14	0.06	-1.28	0.13	0.08
14307	4.63	0.26	-0.72	0.19	0.11	-0.60	0.19	0.12

continued on next page

Table 8: Leo I *continued*

ID	W' ^a (Å)	$\sigma_{W'}$ (Å)	[Fe/H] CG97	$\sigma_{[\text{Fe}/\text{H}]}$ Total	$\sigma_{[\text{Fe}/\text{H}]}$ Random	[Ca/H]	$\sigma_{[\text{Ca}/\text{H}]}$ Total	$\sigma_{[\text{Ca}/\text{H}]}$ Random
14738	3.16	0.24	-1.33	0.18	0.09	-1.29	0.18	0.11
14927	3.25	0.20	-1.29	0.16	0.07	-1.25	0.15	0.09
16048	2.35	0.24	-1.67	0.18	0.08	-1.67	0.18	0.11
16088	2.97	0.21	-1.41	0.16	0.07	-1.38	0.16	0.10
16219	3.11	0.21	-1.35	0.16	0.07	-1.32	0.16	0.10
16248	4.42	0.29	-0.80	0.21	0.12	-0.70	0.21	0.14
16334	3.42	0.23	-1.22	0.17	0.08	-1.17	0.17	0.11
16635	3.14	0.21	-1.34	0.16	0.07	-1.30	0.16	0.10
17009	2.78	0.21	-1.49	0.16	0.07	-1.47	0.16	0.10
17226	4.00	0.23	-0.98	0.17	0.09	-0.90	0.17	0.11
17437	2.94	0.26	-1.43	0.19	0.10	-1.40	0.19	0.12
17620	3.53	0.26	-1.18	0.19	0.10	-1.12	0.19	0.12
17854	0.83	0.19	-2.31	0.15	0.05	-2.39	0.14	0.09
18030	3.89	0.19	-1.03	0.15	0.07	-0.95	0.15	0.09
18214	2.10	0.20	-1.78	0.16	0.06	-1.79	0.15	0.09
18315	2.93	0.17	-1.43	0.14	0.05	-1.40	0.13	0.08
18323	3.04	0.22	-1.38	0.17	0.08	-1.35	0.17	0.10
18509	3.88	0.21	-1.03	0.16	0.08	-0.95	0.16	0.10
18588	3.45	0.20	-1.21	0.16	0.07	-1.16	0.15	0.09
18676	3.65	0.27	-1.13	0.19	0.10	-1.06	0.20	0.13
18765	3.52	0.20	-1.18	0.16	0.07	-1.12	0.15	0.09
18801	3.22	0.22	-1.31	0.17	0.08	-1.26	0.17	0.10
18812	2.32	0.23	-1.68	0.17	0.08	-1.69	0.17	0.11
18880	3.21	0.37	-1.31	0.26	0.15	-1.27	0.26	0.17
19040	3.14	0.26	-1.34	0.19	0.10	-1.30	0.19	0.12
19080	2.09	0.18	-1.78	0.15	0.05	-1.80	0.14	0.08
19262	3.76	0.23	-1.08	0.18	0.09	-1.01	0.17	0.11
19667	1.90	0.17	-1.86	0.14	0.04	-1.89	0.13	0.08
19881	3.41	0.22	-1.23	0.17	0.08	-1.18	0.17	0.10
20470	3.50	0.22	-1.19	0.17	0.08	-1.13	0.17	0.10
20882	3.08	0.26	-1.36	0.19	0.10	-1.33	0.19	0.12
21026	2.78	0.21	-1.49	0.16	0.07	-1.47	0.16	0.10
21192	2.73	0.22	-1.52	0.17	0.08	-1.49	0.16	0.10
21196	2.63	0.28	-1.56	0.20	0.11	-1.54	0.20	0.13
21325	3.15	0.20	-1.34	0.16	0.07	-1.30	0.15	0.09
21348	3.91	0.17	-1.02	0.14	0.06	-0.94	0.14	0.08
22001	3.56	0.19	-1.16	0.15	0.07	-1.10	0.15	0.09
22513	3.00	0.19	-1.40	0.15	0.06	-1.37	0.15	0.09
22788	4.11	0.32	-0.93	0.23	0.13	-0.85	0.23	0.15
23074	3.05	0.17	-1.38	0.14	0.05	-1.34	0.13	0.08
23518	3.40	0.20	-1.23	0.16	0.07	-1.18	0.15	0.09
24095	3.09	0.20	-1.36	0.16	0.07	-1.33	0.15	0.09
25113	3.56	0.19	-1.17	0.15	0.07	-1.10	0.15	0.09
25440	1.55	0.25	-2.01	0.18	0.09	-2.05	0.18	0.12
25820	3.40	0.20	-1.23	0.16	0.07	-1.18	0.15	0.09

^a The W' values listed here have been scaled to the work of R97a.

Table 9: Spectroscopic Data for Stars in the Leo II dSph

ID	W' ^a (Å)	$\sigma_{W'}$ (Å)	[Fe/H] CG97	$\sigma_{[\text{Fe}/\text{H}]}$ Total	$\sigma_{[\text{Fe}/\text{H}]}$ Random	[Ca/H]	$\sigma_{[\text{Ca}/\text{H}]}$ Total	$\sigma_{[\text{Ca}/\text{H}]}$ Random
156	2.87	0.19	-1.45	0.15	0.06	-1.45	0.15	0.09
166	2.71	0.18	-1.52	0.15	0.06	-1.53	0.14	0.08
180	2.52	0.19	-1.60	0.15	0.06	-1.61	0.15	0.09
195	2.53	0.19	-1.60	0.15	0.06	-1.61	0.15	0.09
209	2.54	0.18	-1.59	0.15	0.06	-1.60	0.14	0.08
230	2.61	0.21	-1.56	0.16	0.07	-1.57	0.16	0.10
233	2.49	0.19	-1.62	0.15	0.06	-1.63	0.15	0.09
234	2.05	0.19	-1.80	0.15	0.05	-1.83	0.15	0.09
235	3.26	0.25	-1.29	0.18	0.09	-1.28	0.18	0.11
236	1.81	0.19	-1.90	0.15	0.05	-1.94	0.15	0.09
237	0.36	0.22	-2.51	0.16	0.06	-2.59	0.16	0.10
248	2.74	0.18	-1.51	0.14	0.05	-1.51	0.14	0.08
249	0.77	0.25	-2.34	0.18	0.08	-2.41	0.18	0.11
254	2.94	0.19	-1.43	0.15	0.06	-1.42	0.15	0.09
255	2.38	0.18	-1.66	0.14	0.05	-1.68	0.14	0.08
256	2.68	0.20	-1.54	0.16	0.07	-1.54	0.15	0.09
258	2.59	0.18	-1.57	0.15	0.06	-1.58	0.14	0.08
259	3.54	0.29	-1.17	0.21	0.11	-1.15	0.21	0.13
260	2.60	0.18	-1.57	0.14	0.05	-1.58	0.14	0.08
271	2.82	0.18	-1.48	0.15	0.06	-1.48	0.14	0.08
277	2.20	0.23	-1.74	0.17	0.08	-1.76	0.17	0.10
280	2.76	0.19	-1.50	0.15	0.06	-1.50	0.15	0.09
281	1.46	0.20	-2.05	0.15	0.06	-2.09	0.15	0.09
282	2.72	0.18	-1.52	0.15	0.06	-1.52	0.14	0.08
285	2.76	0.19	-1.50	0.15	0.06	-1.50	0.15	0.09
293	1.95	0.18	-1.84	0.14	0.05	-1.87	0.14	0.08
296	1.53	0.19	-2.02	0.15	0.05	-2.06	0.15	0.09
302	1.97	0.19	-1.83	0.15	0.05	-1.86	0.15	0.09
304	2.01	0.17	-1.81	0.14	0.04	-1.84	0.14	0.08
320	2.96	0.18	-1.42	0.15	0.06	-1.41	0.14	0.08
331	0.90	0.19	-2.28	0.15	0.04	-2.35	0.15	0.09
333	2.89	0.21	-1.45	0.16	0.07	-1.45	0.16	0.10
336	1.50	0.18	-2.03	0.14	0.05	-2.08	0.14	0.08
341	2.93	0.22	-1.43	0.17	0.08	-1.43	0.17	0.10
351	3.01	0.19	-1.40	0.15	0.07	-1.39	0.15	0.09
352	3.23	0.22	-1.31	0.17	0.08	-1.29	0.17	0.10
370	1.80	0.21	-1.90	0.16	0.07	-1.94	0.16	0.10
377	2.22	0.20	-1.73	0.16	0.06	-1.75	0.15	0.09
379	2.72	0.20	-1.52	0.16	0.07	-1.52	0.15	0.09
392	2.19	0.24	-1.74	0.18	0.09	-1.76	0.18	0.11
395	2.24	0.19	-1.72	0.15	0.06	-1.74	0.15	0.09
396	2.10	0.33	-1.78	0.23	0.13	-1.80	0.23	0.15
397	2.47	0.21	-1.62	0.16	0.07	-1.64	0.16	0.10
402	2.28	0.21	-1.70	0.16	0.07	-1.72	0.16	0.10
409	1.97	0.30	-1.83	0.21	0.11	-1.86	0.21	0.14
420	2.85	0.18	-1.46	0.15	0.06	-1.46	0.14	0.08
422	1.32	0.21	-2.11	0.16	0.06	-2.16	0.16	0.10
429	2.65	0.21	-1.55	0.16	0.07	-1.55	0.16	0.10
430	2.38	0.19	-1.66	0.15	0.06	-1.68	0.15	0.09
432	3.84	0.35	-1.05	0.24	0.14	-1.02	0.25	0.16
434	2.40	0.16	-1.65	0.14	0.04	-1.67	0.13	0.07
435	2.44	0.28	-1.64	0.20	0.11	-1.65	0.20	0.13
441	2.72	0.23	-1.52	0.17	0.08	-1.52	0.17	0.10
471	3.31	0.65	-1.27	0.43	0.27	-1.26	0.44	0.29
493	2.24	0.23	-1.72	0.17	0.08	-1.74	0.17	0.10
495	2.45	0.21	-1.63	0.16	0.07	-1.65	0.16	0.10

continued on next page

Table 9: Leo I *continued*

ID	W' ^a (Å)	$\sigma_{W'}$ (Å)	[Fe/H] CG97	$\sigma_{[\text{Fe}/\text{H}]}$ Total	$\sigma_{[\text{Fe}/\text{H}]}$ Random	[Ca/H]	$\sigma_{[\text{Ca}/\text{H}]}$ Total	$\sigma_{[\text{Ca}/\text{H}]}$ Random
508	2.90	0.22	-1.44	0.17	0.08	-1.44	0.17	0.10
524	0.81	0.22	-2.32	0.16	0.06	-2.39	0.16	0.10
526	2.76	0.22	-1.50	0.17	0.08	-1.50	0.17	0.10
533	2.83	0.23	-1.47	0.17	0.08	-1.47	0.17	0.10
541	2.24	0.23	-1.72	0.17	0.08	-1.74	0.17	0.10
549	2.70	0.24	-1.53	0.18	0.09	-1.53	0.18	0.11
552	2.41	0.26	-1.65	0.19	0.10	-1.66	0.19	0.12
556	4.65	0.41	-0.71	0.28	0.17	-0.65	0.29	0.19
558	1.86	0.21	-1.88	0.16	0.07	-1.91	0.16	0.10
569	2.17	0.23	-1.75	0.17	0.08	-1.77	0.17	0.10
570	2.84	0.32	-1.47	0.23	0.13	-1.47	0.23	0.14
573	3.34	0.21	-1.26	0.16	0.07	-1.24	0.16	0.10
576	3.00	0.26	-1.40	0.19	0.10	-1.40	0.19	0.12
584	2.55	0.22	-1.59	0.17	0.08	-1.60	0.17	0.10
588	3.12	0.26	-1.35	0.19	0.10	-1.34	0.19	0.12
604	2.28	0.21	-1.70	0.16	0.07	-1.72	0.16	0.10
614	3.02	0.21	-1.39	0.16	0.08	-1.39	0.16	0.10
623	2.06	0.21	-1.79	0.16	0.07	-1.82	0.16	0.10

^a The W' values listed here have been scaled to the work of R97a.

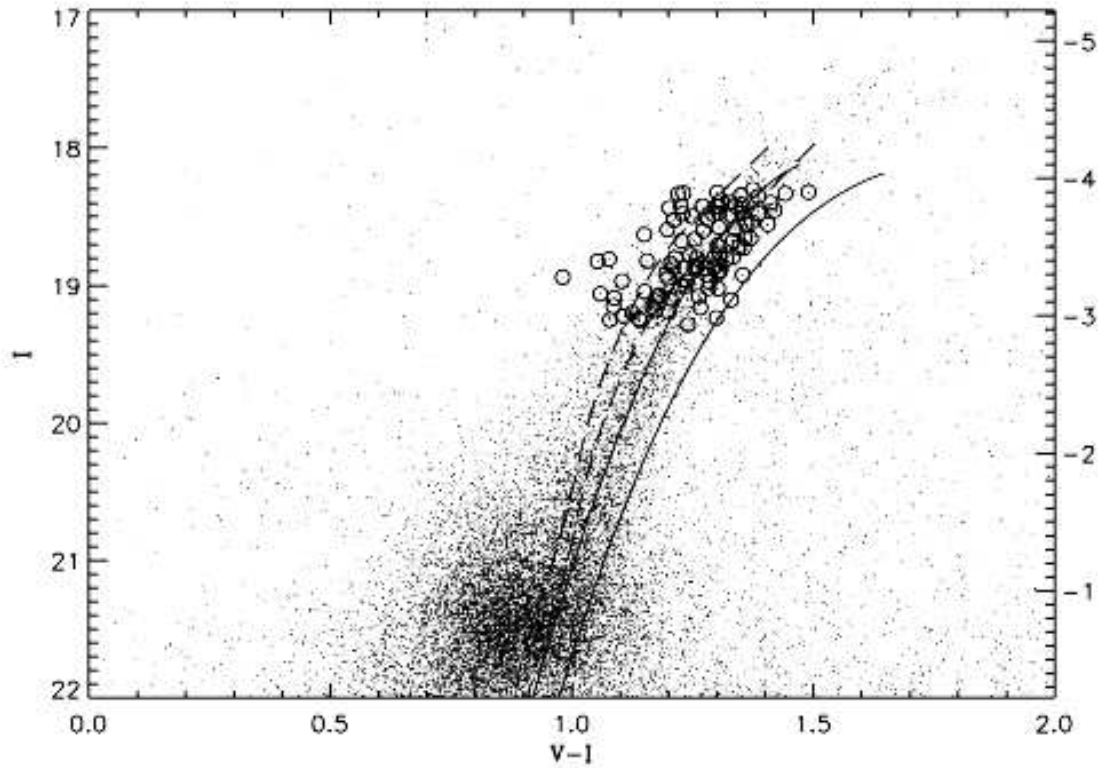


Figure 1. The color-magnitude diagram for the Leo I dSph with the spectroscopic targets shown as large circles. Solid lines show fiducials for Galactic globular clusters, from left to right, M15 with $[Fe/H] = -2.0$ and M2 with $[Fe/H] = -1.31$ (Da Costa & Armandroff 1990). The range in ages for the selected stars is demonstrated with the dashed lines representing Yale isochrones with $[Fe/H] = -1.28$ and with ages 2 and 4 Gyrs, from left to right, respectively; stars bluer than the M2 fiducial are likely younger. Note that, for convenience, we adopted the M15 fiducial to describe the shape of the Leo I RGB in selecting our spectroscopic targets.

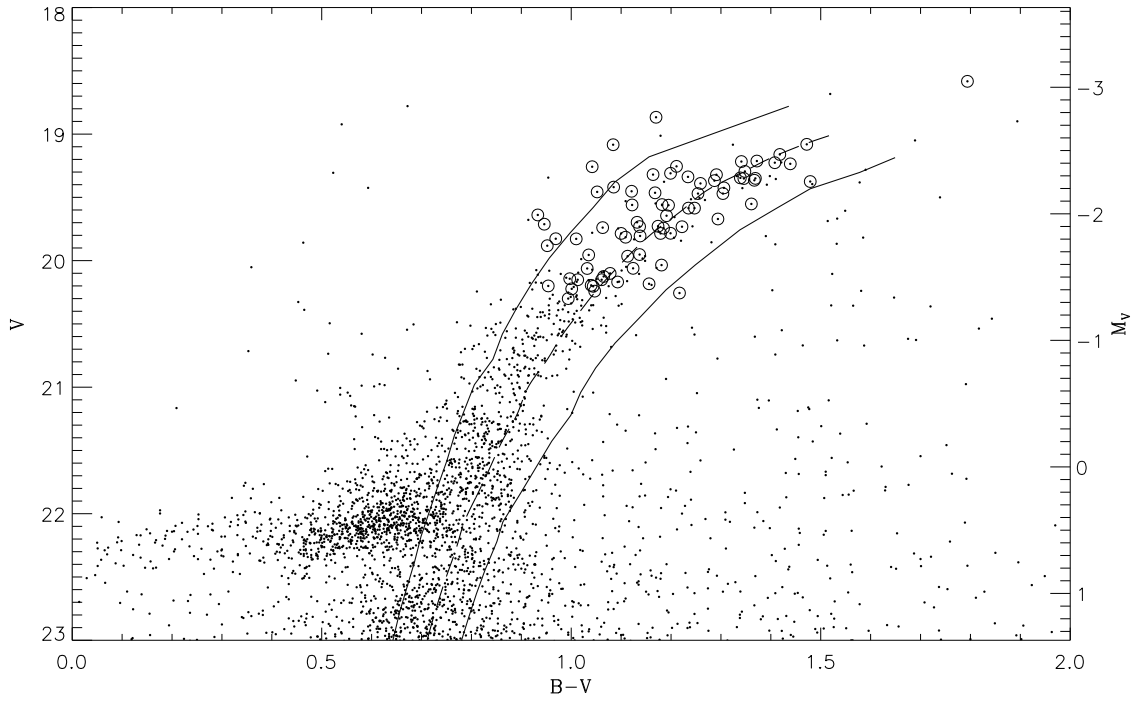


Figure 2. The color-magnitude diagram for the Leo II dSph with the spectroscopic targets shown as large circles. Solid lines show fiducials for Galactic globular clusters, from left to right, M68 with $[Fe/H] = -1.92$ (McClure et al. 1987) and M5 with $[Fe/H] = -1.17$ (Sandquist et al. 1996). The dashed line shows the adopted fiducial for the RGB of Leo II.

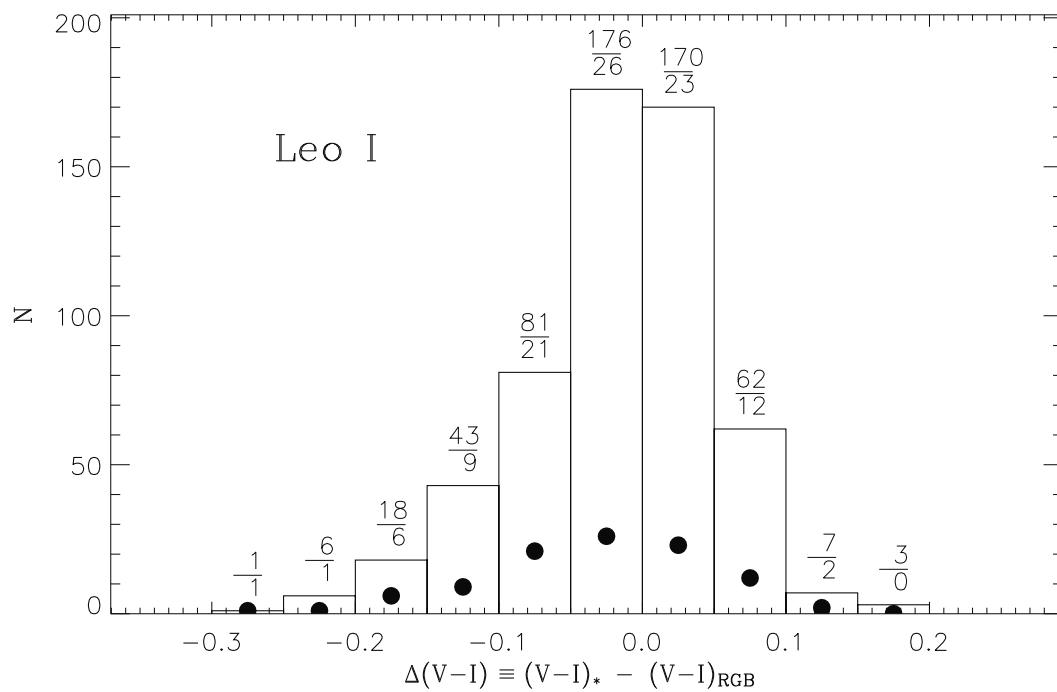


Figure 3. The histogram of the entire sample of RGB stars in the Leo I dSph (histogram) and the stars for which spectra were obtained (filled circles). Above each bin is given the number of stars in the bin in the total sample divided by the number of stars in the bin in the spectroscopic sample.

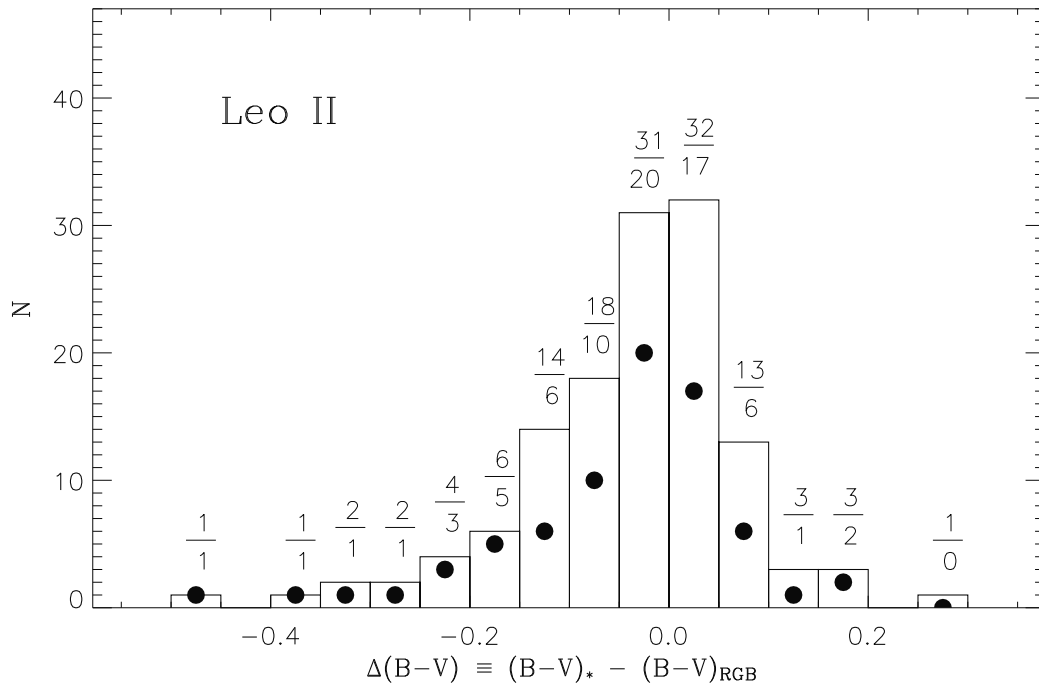


Figure 4. The histogram of the entire sample of RGB stars in the Leo II dSph (histogram) and the stars for which spectra were obtained (filled circles). Above each bin is given the number of stars in the bin in the total sample divided by the number of stars in the bin in the spectroscopic sample.

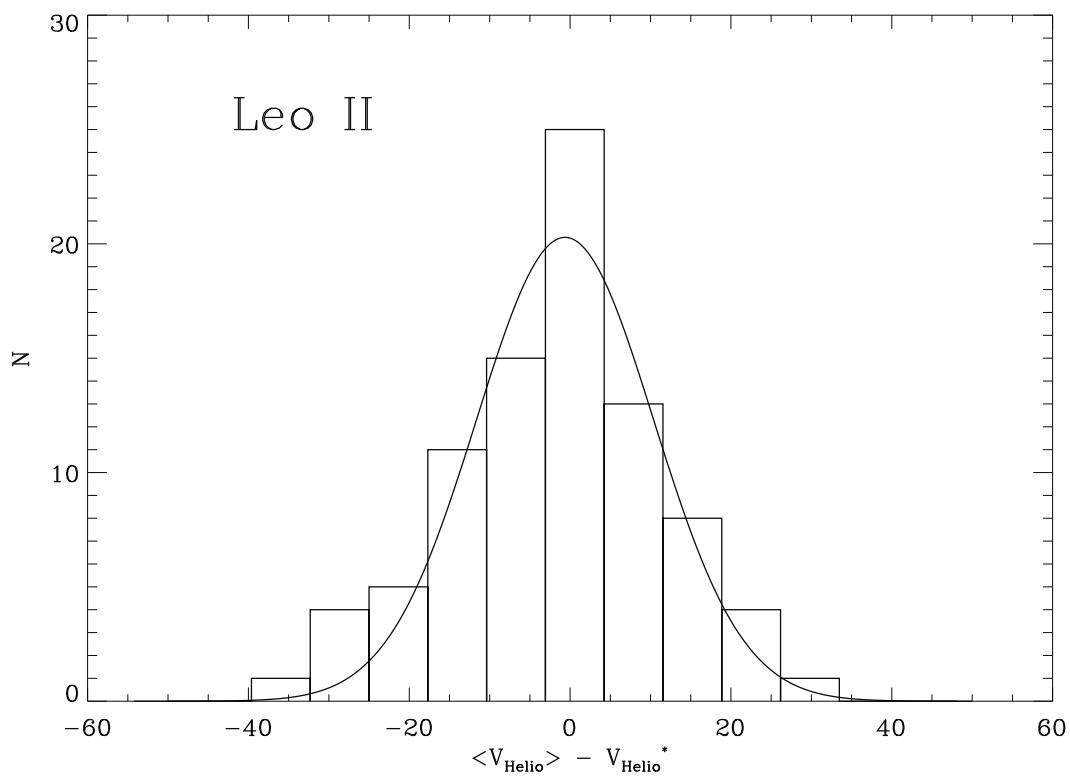
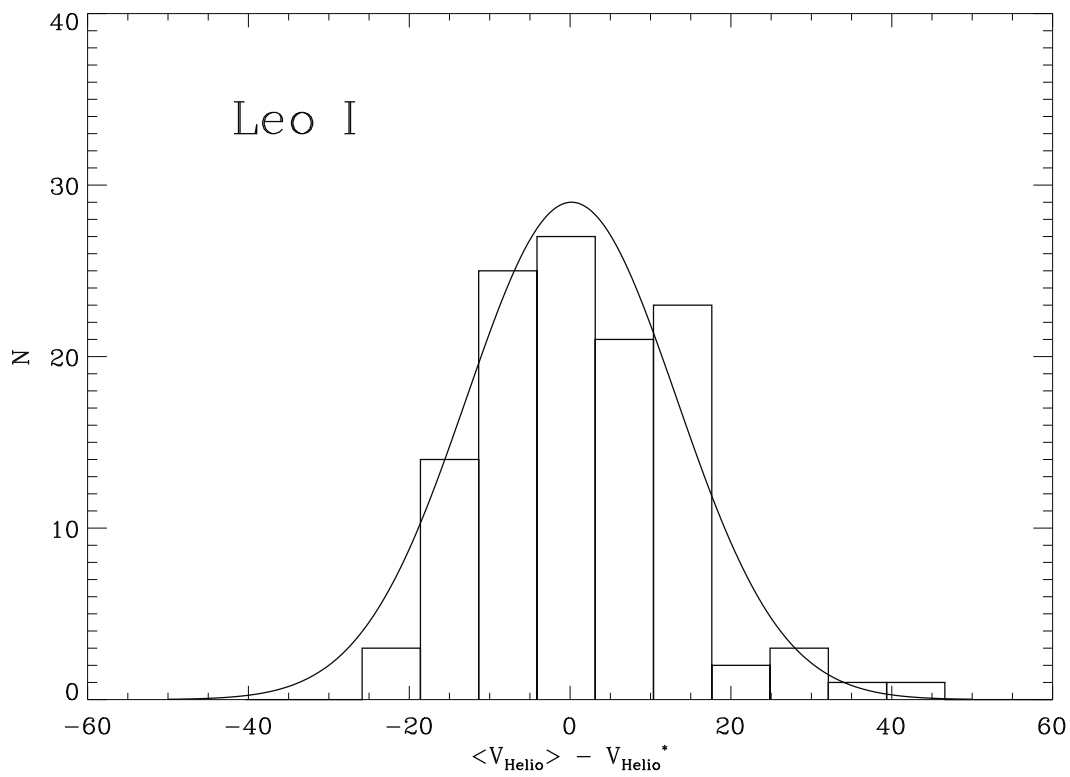


Figure 5. Velocity distributions of Leo I and Leo II overlaid with a Gaussian.

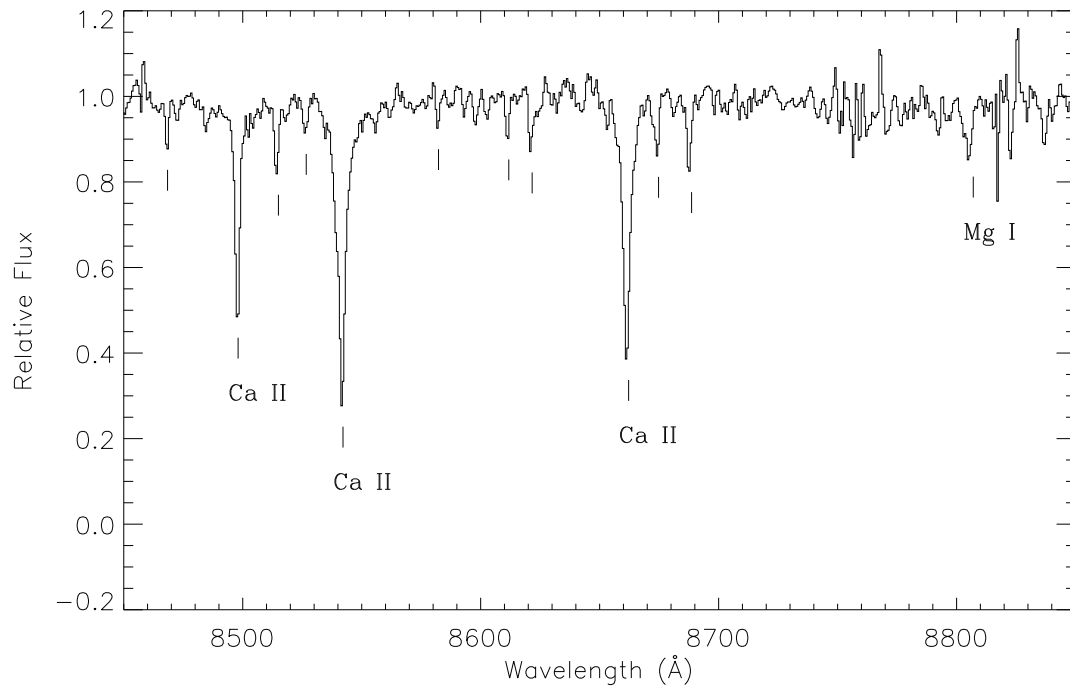


Figure 6. Low-dispersion spectrum of Star #9915 in the Leo I dSph with $[Ca/H] = -0.97$ and $SNR = 35$. For clarity, Fe I lines are marked but not labelled. Note that the Ca II lines are resolved but the weak Fe I lines are not. Indeed many of the Fe I lines are actually blends at this resolution ($R=14,000$).

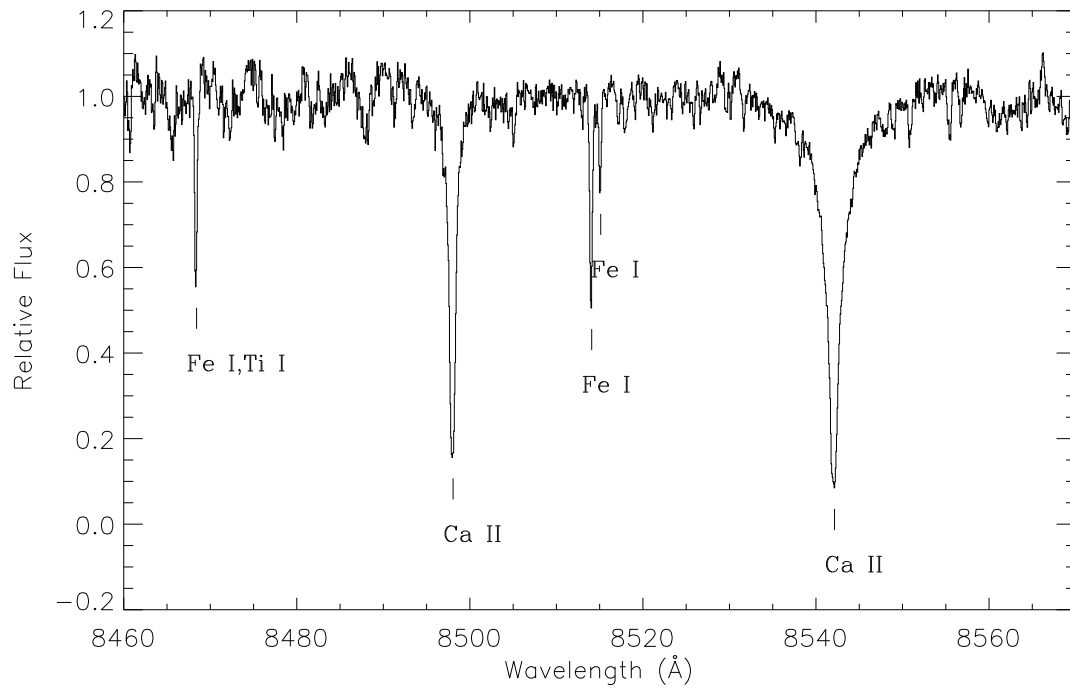


Figure 7. High-dispersion spectrum of calibration star HD135148, which as $[Fe/H] = -1.81$ and spectral type K0III (Bosler 2004). The wavelength coverage is much narrower than that of Fig 6. Note how the two Fe I lines blended in the low dispersion spectrum are resolved at higher resolution ($R=40,000$) while the Ca II lines are resolved at both resolutions (see Figure 6).

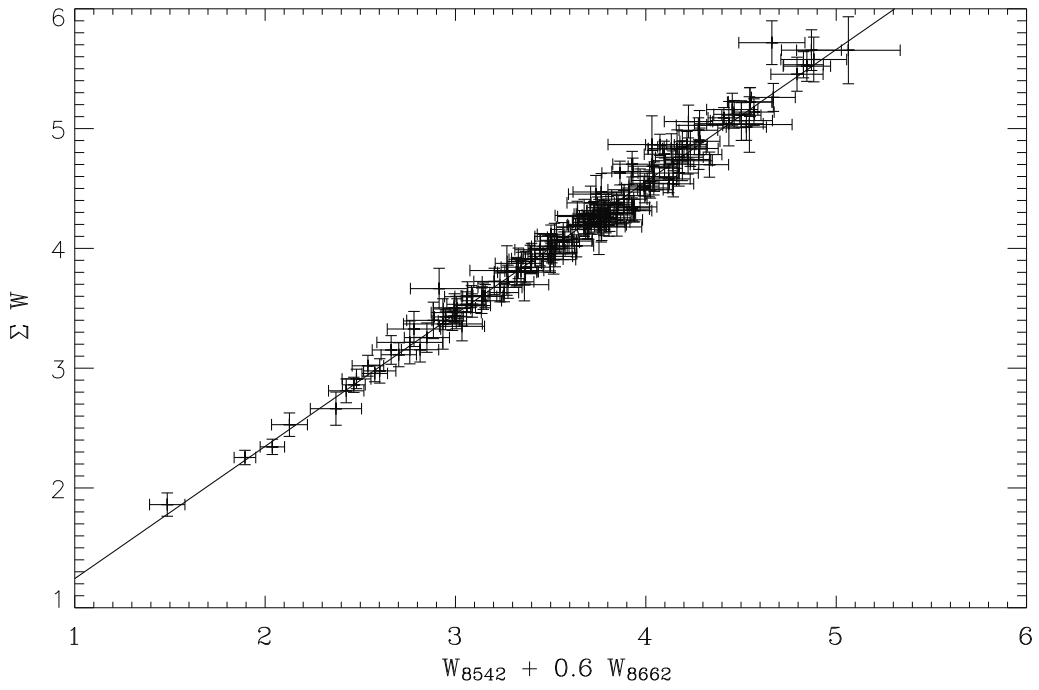


Figure 8. The relationship between the weighted sum of the two strongest Ca II lines and the weighted sum of all three Ca II lines in the globular cluster stars.

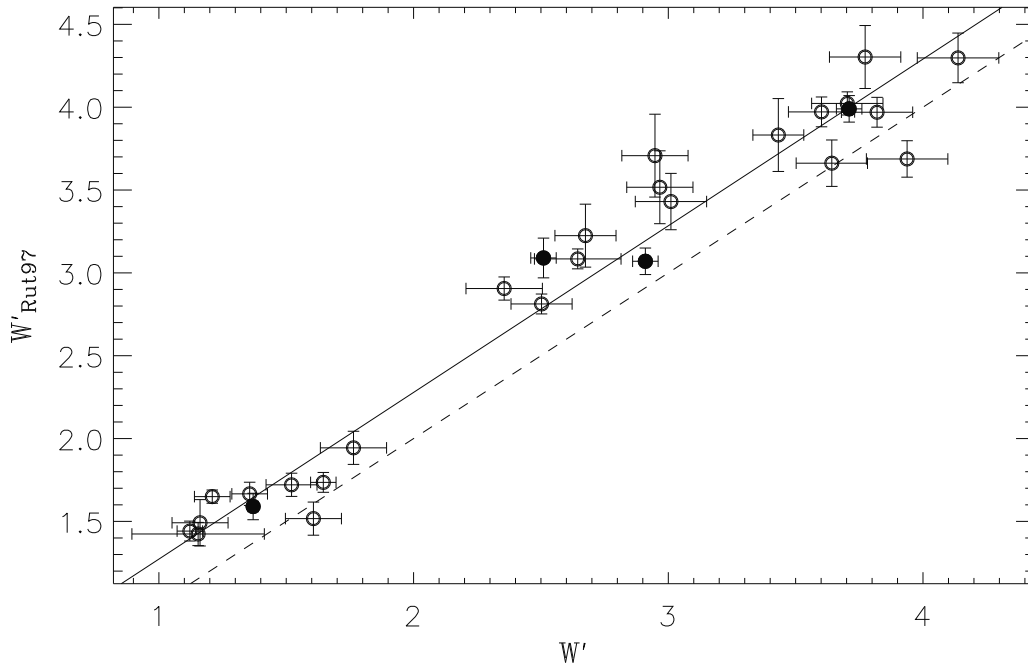


Figure 9. The reduced equivalent width measured by us and R97a for individual globular cluster stars in NGC 1904, NGC 4590, NGC 5272, and NGC 6171 (open circles), and the averages for the clusters (filled circles). The dashed line shows the line of equivalence. The solid line shows the regression using the W' values for individual stars.

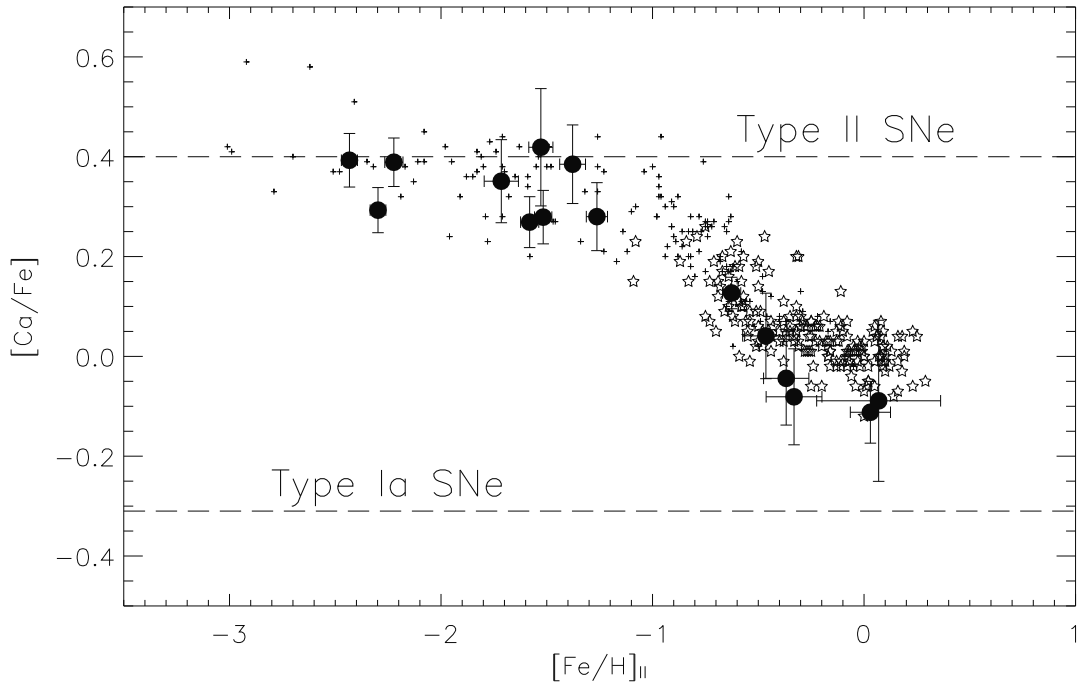


Figure 10. The $[Ca/Fe]$ ratio as a function of $[Fe/H]$ for all Galactic clusters from Bosler(2004; large filled circles) and individual Milky Way field stars from Fulbright (2000; pluses) and Edvardsson et al. (1993; open stars). Dashed horizontal lines indicate the predicted abundance ratios from Type II and Type Ia SNe (+0.4 from McWilliam, 1997 and -0.31 from Thielemann et al. 1986, respectively).

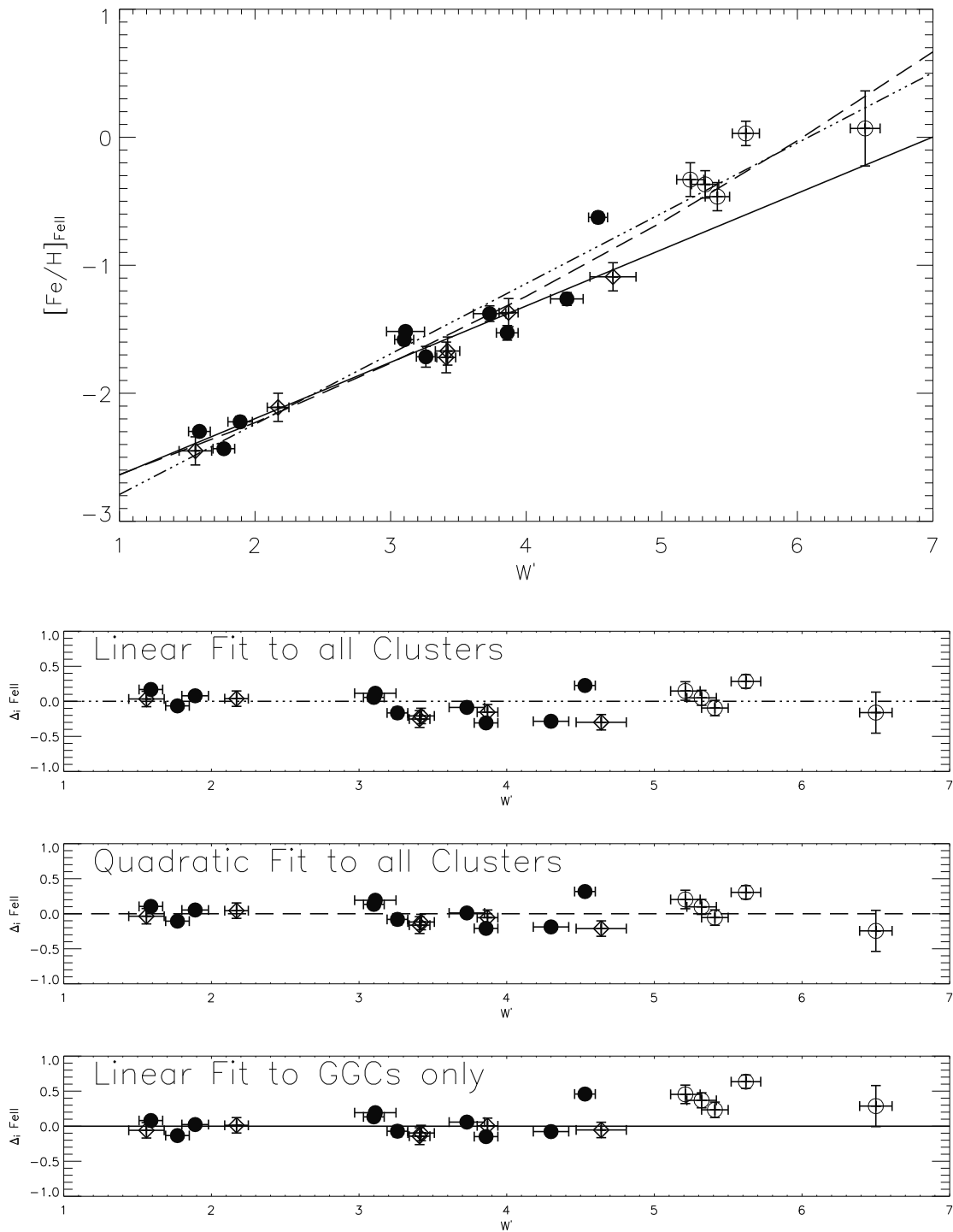


Figure 11. Iron abundances from singly-ionized lines versus reduced equivalent width and residuals for all of the clusters. Solid circles indicate GGCs; open circles indicate GOCs; and the KI03 clusters scaled to this data set are indicated with open diamonds. The dotted-dashed line indicates a linear fit to all stars, the dashed line is a 2nd order polynomial, and the solid line indicates a linear fit to the GGCs with $[\text{Fe}/\text{H}] < -0.8$, see text for details.

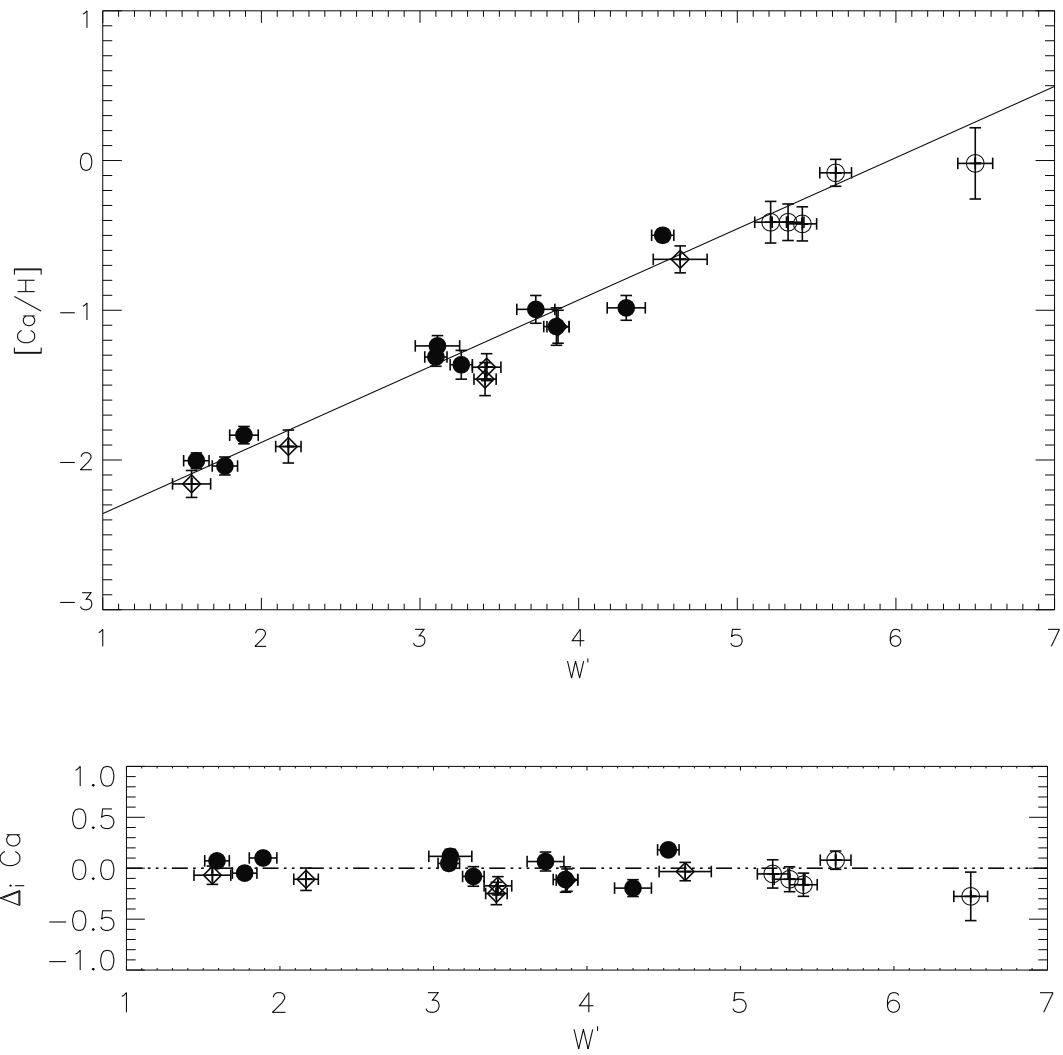


Figure 12. $[Ca/H]$ versus W' and residuals for all observed clusters. Solid circles indicate GGCs; open circles indicate GOCs; and the KI03 clusters scaled to this data set are indicated with open diamonds

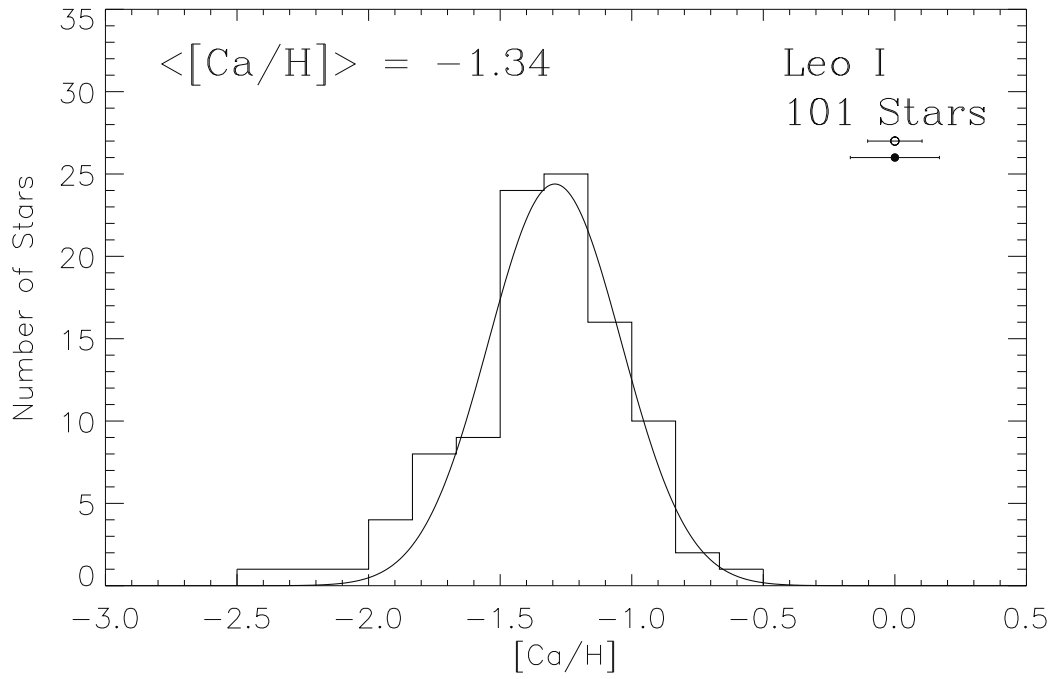


Figure 13. The metallicity distribution function in the Leo I dSph. Typical $1-\sigma$ errors shown in the upper right; random and total errors are shown as open and filled circles, respectively. The Gaussian fit to the distribution is shown as a solid line.

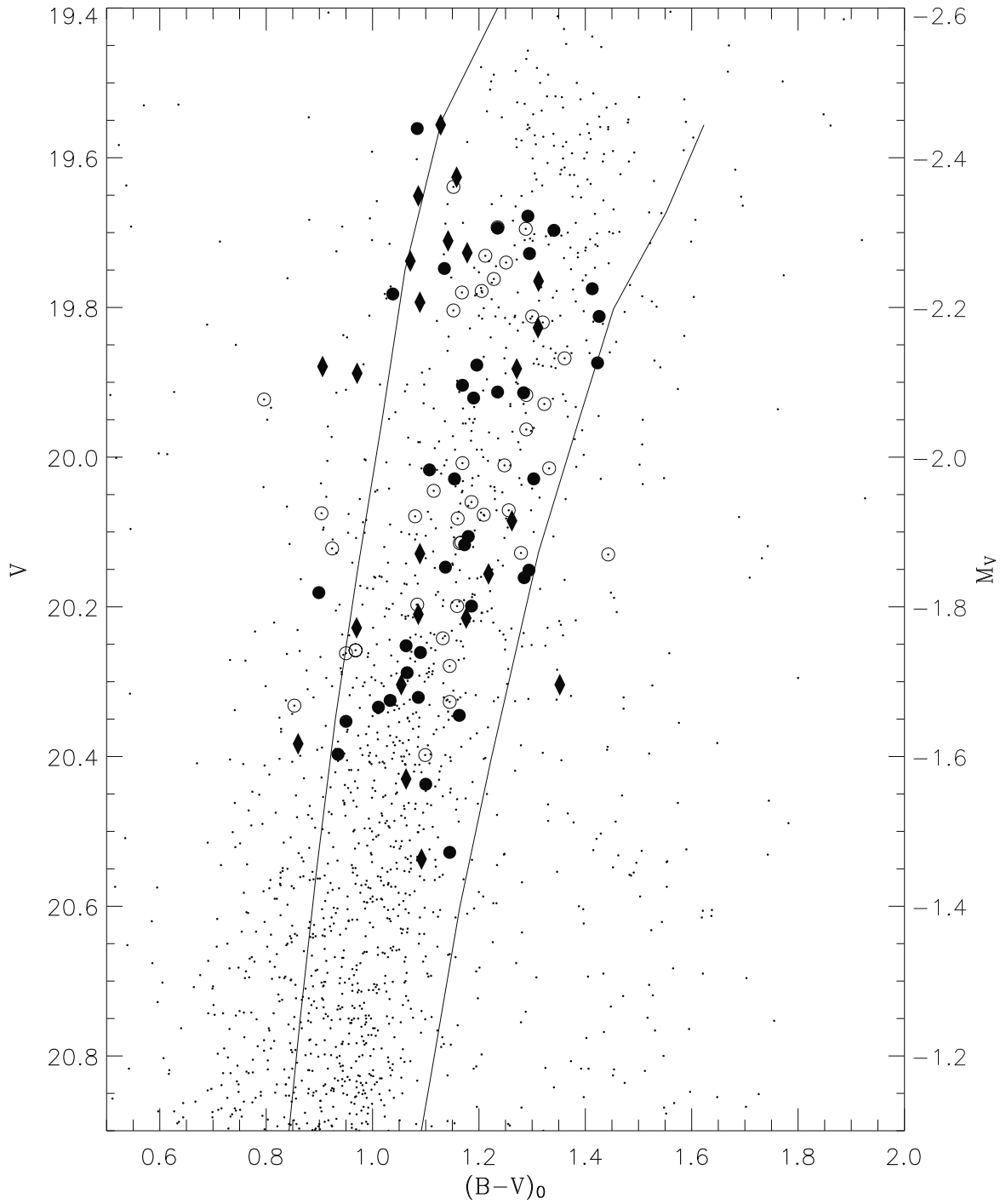


Figure 14. The CMD of Leo I showing the metallicities of the stars. V, B-V rather than I, V-I is shown for ease of comparison with the Leo II CMD. Stars are coded based on their derived metallicity: filled diamonds for stars with $[Ca/H] < -1.5$; open circles for stars with $-1.5 \leq [Ca/H] < -1.2$; filled circles for stars with $[Ca/H] \geq -1.2$. The fiducials for GGCs M5 ($[Ca/H] = -0.96$) and M68 ($[Ca/H] = -1.78$) are over-plotted for reference.

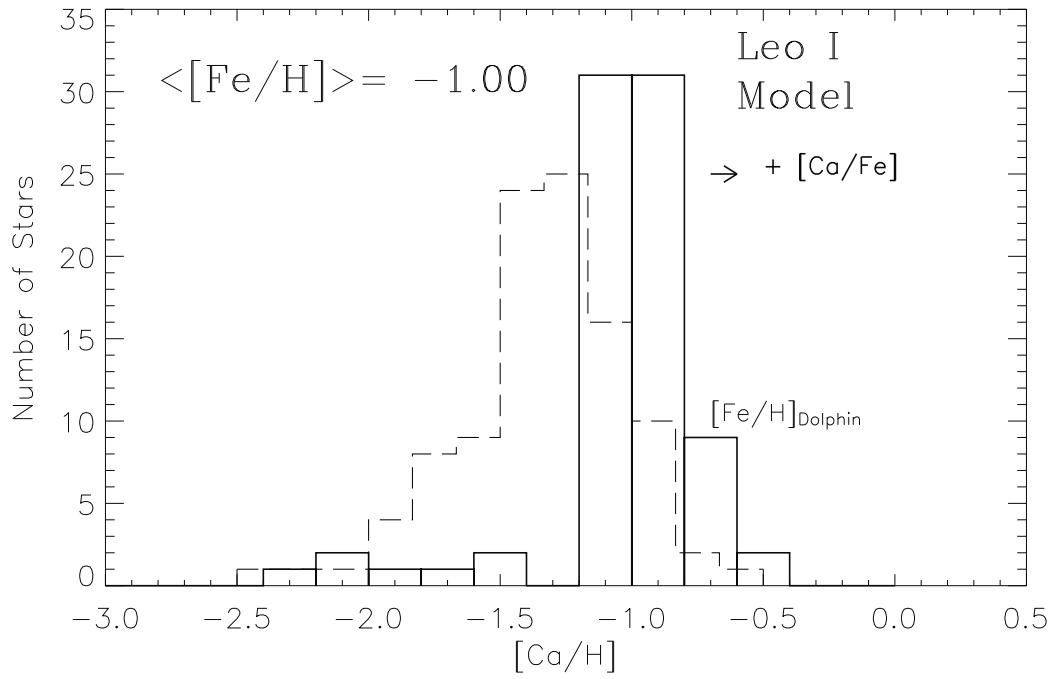


Figure 15. The predicted metallicity distribution from Dolphin’s CMD modelling of the Leo I dSph (solid lines) along with the observed distribution (dashed lines). Note that Dolphin derived $[Fe/H]$ and a significant offset exists between the two distributions. If $[Ca/Fe]$ from Shetrone et al. (2003) is added to Dolphin’s $[Fe/H]$ values yield $[Ca/H]$ (indicated with an arrow of length 0.1 dex), the theoretical histogram shifts even further from the observed distribution (see text for discussion).

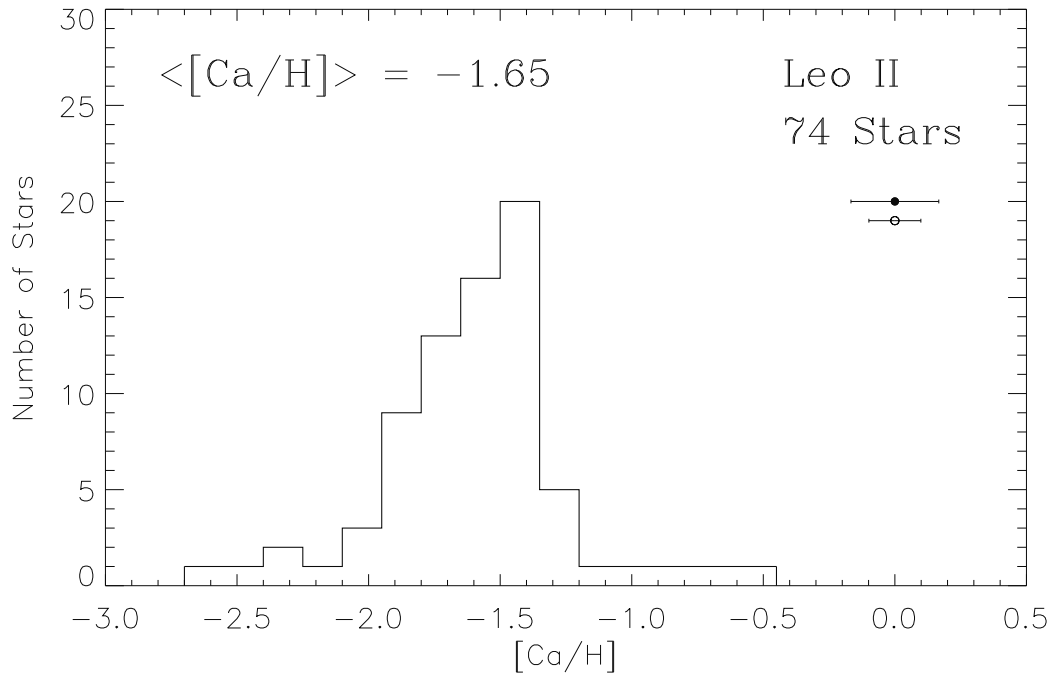


Figure 16. The observed metallicity distribution function in the Leo II dSph. Typical $1\text{-}\sigma$ errors are shown in the upper right; median random and total errors are shown as open and filled circles, respectively.

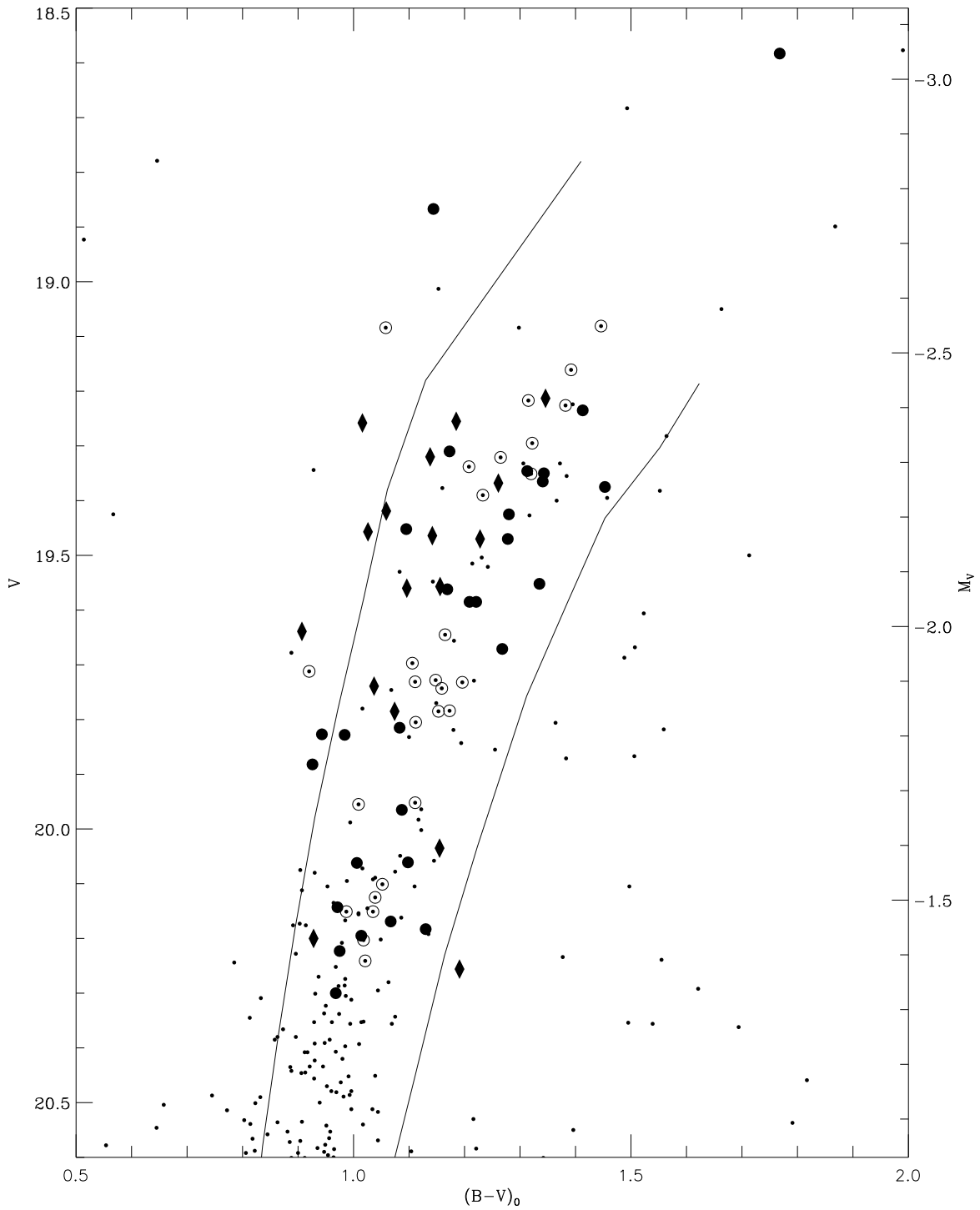


Figure 17. The CMD of Leo II showing the metallicities of the stars. Stars are coded based on their derived metallicity: filled diamonds for stars with $[Ca/H] < -1.8$; open circles for stars with $-1.8 \leq [Ca/H] < -1.5$; filled circles for stars with $[Ca/H] \geq -1.5$. The fiducials for GGCs M5 ($[Ca/H] = -0.96$) and M68 ($[Ca/H] = -1.78$) are over-plotted for reference.

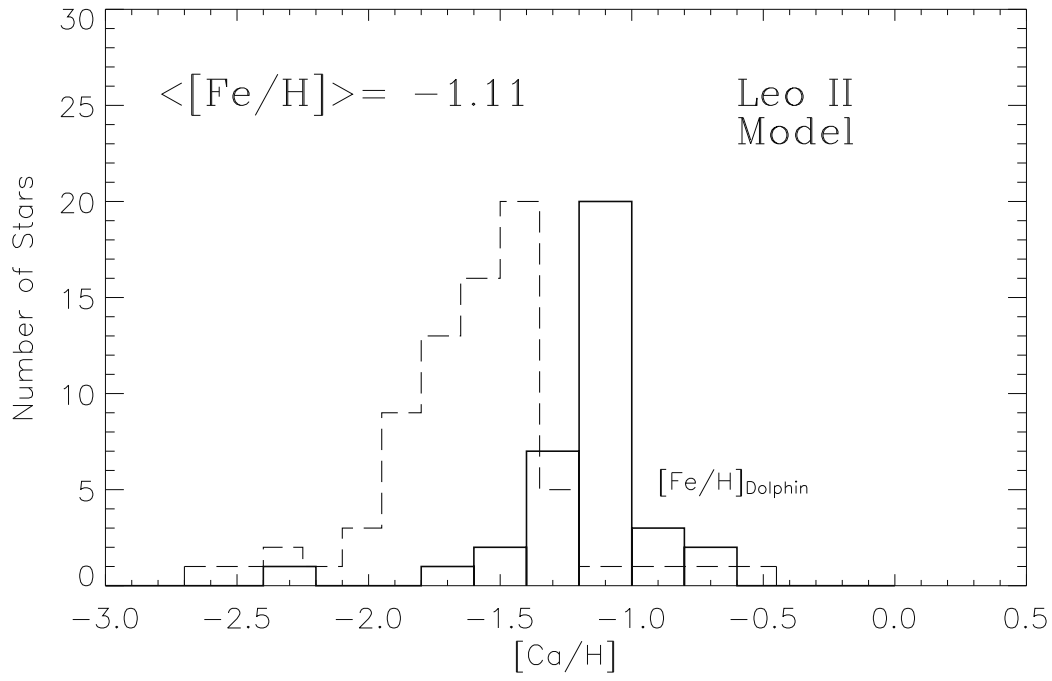


Figure 18. The predicted metallicity distribution from Dolphin's CMD modelling of the Leo II dSph (solid lines) along with the observed distribution (dashed lines). Note that Dolphin derived $[Fe/H]$ rather than $[Ca/H]$ values, and a significant offset exists between the central values of the two distributions (see text for discussion).

The Chemical Abundances of the Stellar Populations in the Leo I and Leo II dSph Galaxies^{*}

Tammy L. Bosler,¹ Tammy A. Smecker-Hane², Peter B. Stetson³

¹National Science Foundation, 4201 Wilson Boulevard, Arlington, Virginia 22230, USA.

²Department of Physics & Astronomy, 4129 Frederick Reines Hall, University of California, Irvine, CA, 92697–4575, USA.

³National Research Council of Canada, Herzberg Inst. of Astrophysics, Dominion Astrophysical Observatory, 5071 West Saanich Road, Victoria, BC V9E 2E7, Canada.

28 August 2018

ABSTRACT

We have obtained spectra of 102 red giant branch (RGB) stars in the Leo I dwarf spheroidal galaxy (dSph) and 74 RGB stars in the Leo II dSph using the Low Resolution Spectrograph (LRIS) on the Keck I 10-meter Telescope. We report on the calcium abundances $[\text{Ca}/\text{H}]$ derived from the strengths of the Ca II triplet absorption lines at 8498, 8542, 8662 Å in the stellar spectra using a new Ca II triplet calibration to $[\text{Ca}/\text{H}]$. The two galaxies have different average $[\text{Ca}/\text{H}]$ values of -1.34 ± 0.02 for Leo I and -1.65 ± 0.02 for Leo II with intrinsic abundance dispersions of 1.2 and 1.0 dex, respectively. The typical random and total errors in derived abundances are 0.10 and 0.17 dex per star. For comparison to existing literature, we also converted our Ca II measurements to $[\text{Fe}/\text{H}]$ on the scale of Carretta and Gratton (1997) though we discuss why this may not be the best determinant of metallicity; Leo I has a mean $[\text{Fe}/\text{H}] = -1.34$ and Leo II has a mean $[\text{Fe}/\text{H}] = -1.59$. The metallicity distribution function of Leo I is approximately Gaussian in shape with an excess at the metal-rich end, while that of Leo II shows an abrupt cutoff at the metal-rich end. The lower mean metallicity of Leo II is consistent with the fact that it has a lower luminosity, hence lower total mass, than Leo I; thus the evolution of Leo II may have been affected more by mass lost in galactic winds. We compare our observed metallicity distribution functions to those inferred by Dolphin (2002) from modelling of deep color-magnitude diagrams (CMDs) obtained with the Hubble Space Telescope (HST). The models predict a median metallicity that is systematically more metal-rich than observed, by 0.36 dex in the Leo I dSph, and by 0.49 dex in the Leo II dSph. We show that differences this large are not likely caused by non-solar $[\text{Ca}/\text{Fe}]$ in the dSph stars. Our direct and independent measurement of the metallicity distributions in these dSph will allow a more accurate star-formation histories to be derived from future analysis of their CMDs.

Key words: stars: abundances — galaxies: abundances — galaxies: evolution — galaxies: dwarf — galaxies: individual (Leo I dSph, Leo II dSph)

1 INTRODUCTION

The goal of this project is to map the chemical abundance distribution of the stellar populations of the Leo I and Leo II dwarf spheroidal (dSph) galaxies in order to constrain the physical processes that regulate their evolution. Table 1 lists the properties of each galaxy for reference.

Dwarf spheroidal galaxies (dSphs) are low luminosity ($M_V \leq -14$ mag), low surface brightness ($\Sigma_V \lesssim 22$ mag/arcsec²), and

low mass ($M_{\text{tot}} \lesssim 10^7 M_\odot$) systems. They have little or no interstellar gas ($M_{\text{HI}} \lesssim 10^5 M_\odot$), and are dark-matter dominated. For recent reviews, see Mateo (1998), Smecker-Hane & McWilliam (1999), and Grebel (2000). Their stellar velocity dispersions are typically ~ 10 km/sec, and therefore galactic winds from the first generation of supernovae are expected to efficiently rid them of gas and prevent extended or multiple epochs of star formation. Although they seem to lack the mass and material to sustain star formation for a significant fraction of the Hubble time, the CMDs of the dSph satellites of the Milky Way have shown that most dSphs have *very complex* star formation histories (SFHs) and chemical evolution. Cold dark matter hierarchical galaxy formation models have difficulty explaining extended epochs of star formation in dSphs. They are predicted to begin forming stars at early epochs, but lose a significant amount of gas due to photoevaporation during

^{*} Data presented herein were obtained at the W.M. Keck Observatory, which is operated as a scientific partnership among the California Institute of Technology, the University of California and the National Aeronautics and Space Administration. The Observatory was made possible by the generous financial support of the W.M. Keck Foundation.

reionization, which curtails their star formation activity (Barkana & Loeb 1999). Klypin et al. (1999) also points out that CDM models vastly over predict the number of low mass halos; the Milky Way and M31 have only one-tenth the number of low mass satellites. Are these “missing” satellites dark because they never accreted gas, or were the dark matter halos stripped of their baryons through supernovae-driven winds? Determining the age of the oldest stars in the outer halo satellites such as the Leo I and Leo II dSphs, whose Galactocentric distances are 270 and 204 kpc, respectively, is important because CDM models predict that these should form later than the Milk Way’s inner halo globular clusters and dSphs.

Almost every dSph in the Local Group appears to have had a unique SFH. From analysis of a CMD obtained with WFPC2 aboard the HST, Mighell & Rich (1996) have shown that the Leo II dSph formed essentially all of its stars from ~ 7 to 14 Gyr ago with 50% of its stars formed in a 4 Gyr period. In striking contrast, most of the stars in the Leo I dSph are younger than this; 87% of its star formation occurred from 1 to 7 Gyr ago and only 12% occurred $\gtrsim 10$ Gyr ago (Gallart et al. 1999a and 1999b). More recent photometry from Held et al. (2000), which includes a much larger radial coverage than the HST data, also shows an extended blue horizontal-branch in Leo I indicating the existence of an old, metal-poor population. Held et al. (2001) also report the discovery of candidate RR Lyrae stars in the system, further strengthening the case for an old population in Leo I.

Defining the chemical evolution of the dSphs will be key to understanding their complex SFHs because the chemical abundances constrain the inflow and outflow of gas from the systems. Did some dSphs accrete fresh gas that fuelled subsequent star formation? Were outflows driven by supernovae so extensive that today’s dSphs have only a small fraction of their former mass? The chemical abundances of dSph stars – the mean metallicity as well as the detailed distribution in metallicity – can be determined from spectroscopy of individual red giant stars in the dSphs. Measuring the metallicity distribution of individual stars will greatly improve the SFHs derived from analysis of CMDs.

In order to understand the true spread in stellar chemical abundances more precise abundance indicators than can be inferred from CMD analysis are needed. We, therefore, measured the abundance distribution of the Leo I and Leo II dSphs from spectroscopy of individual red giant stars using the Ca II absorption lines in the near infrared (8498, 8542, and 8662 Å). We utilized the new calibration of Ca II to [Ca/H] from Bosler (2004, hereafter B04¹) to derive abundances with random and total errors of 0.10 and 0.17 dex, respectively. Additionally, we calculated the [Fe/H] values of the stars based on earlier empirical calibrations between Ca II and [Fe/H] simply for comparison with existing work using this method; however, we discuss the pitfalls of using the Ca II triplet to determine [Fe/H]. The new Ca II calibration to [Ca/H] is completely independent of star to star variations in [Ca/Fe] unlike previously utilized Ca II abundance calibrations.

2 THE SAMPLE

The photometry and astrometry for Leo I and Leo II were obtained as part of a larger program to provide homogeneous photometry for star clusters and nearby resolved galaxies (e.g., Stetson,

Hesser & Smecker-Hane 1998, Stetson 2000). The present photometry is based upon a large database of CCD images acquired by ourselves and collaborators, images obtained from the archives of the Canada-France-Hawaii Telescope and the Isaac Newton Group, and images privately donated by other astronomers. In the present case, the Leo I photometric database contains some 30,000 different stars recorded in 449 individual CCD images taken in the UBVR filters (4 in U, 96 in B, 257 in V, 72 in R, and 20 in I) covering an irregular area spanning an extreme range of 40.7’ in the east-west direction by 40.6’ north-south. For Leo II, some 17,000 stars were measured in 124 CCD images taken in UBVR filters (2 in U, 30 in B, 81 in V, 5 in R, and 6 in I) spanning an area with extreme dimensions 16.9’ by 16.5’. All observations were transformed to the UBVR photometric system of Landolt (1992; see also Stetson 2000) based on observations of primary (Landolt) and secondary (Stetson) standard stars obtained during the same nights with the same equipment.

The astrometry for the Leo I and II photometric catalogs was based on positions of reference stars taken from the United States Naval Observatory Guide Star Catalogue A2.0; (henceforth USNOGSC, Monet et al. 1998), access to which was obtained through the services of the Canadian Astronomy Data Center. The authors of the USNOGSC claim a typical astrometric error of 0.25 arcsec, which they believe is dominated by systematic errors in the calibration procedure. When transforming relative (x, y) positions from large-format CCD images to absolute right ascensions and declinations from the USNOGSC for stars in common, the typical root-mean-square difference is 0.3 to 0.4 arcsec in each coordinate. Some of this is clearly due to proper-motion displacements accumulated during the forty-plus years between the obtaining of the first Palomar Observatory Sky Survey and these CCD data. However, a significant part of the differences is also due to the lower angular resolution of the Schmidt plates as scanned by the Precision Measuring Machine (built and operated by the U. S. Naval Observatory Flagstaff): particularly in crowded fields such as these, a single entry in the USNOGSC is occasionally found to correspond to the photocenter of a close pair or a clump of several stars in the CCD imagery.

As a result of these non-Gaussian errors (i.e., proper motions and blending), astrometric transformations were performed using an iterative procedure wherein 20-constant cubic polynomials are used to approximate the transformation of the (x, y) positions measured in the CCD images to standard coordinates obtained from the USNOGSC (see Cohen, Briley, & Stetson 2002 for more details). When this procedure has been completed 706 detections common to the USNOGSC were found and the data set in the field of Leo I show positional differences with a dispersion of 0.37 arcsec in both the right ascension and declination directions; for Leo II, 292 stars show positional agreement with a dispersion of 0.32 arcsec in each direction.

The systematic errors of right ascensions and declinations on the system of the USNOGSC are expected to be of order $\sigma/\sqrt{N-20} \sim 0.02$ arcsec where N is the number of stars used in the astrometric solution. We can provide no independent information on the accuracy with which the USNOGSC coordinate system is referred to an absolute inertial reference frame of right ascension and declination. Individual *random* errors in the coordinate measurements are probably not much better than 0.02 arcsec on a star-by-star basis, the errors becoming somewhat worse where crowding is an issue. The logarithm of the observed flux in the stellar spectra is very well correlated with our V-band magnitudes for the stars, and thus there is no evidence of sizable relative position

¹ ftp://sculptor.ps.uci.edu/pub/smecker/bosler_thesis.pdf

errors compared to the size of the 1.0 arcsec-wide slits. However while aligning LRIS slit masks on the stars in a given field, one rotates the field of view to get the best possible alignment, and thus the flux measurements do not rule out possible systematic rotations of the coordinate system with respect to the true inertial frame. Still, these should not be present at levels much greater than the 0.02-arcsec precision claimed above. A comprehensive catalog of positions and photometry for these two galaxies is in preparation.

Our current CMDs for the Leo I and Leo II dSphs are shown in Figures 1 and 2, respectively. The stars in the spectroscopic sample are marked with large open circles. On each CMD, fiducials for two Galactic globular clusters with different metallicities are plotted for comparison. For Leo I, we have assumed a reddening of $E(V-I) = 1.25[1 + 0.06(B-V)_0 + 0.014E(B-V)]$ $E(B-V) = 0.054$ mag using the reddening relationship derived by Dean, Warren & Cousins (1978) and assuming the mean color of the red giant branch (RGB) stars is $(B-V)_0 = 1.2$. We have defined fiducial RGBs for each dSph, which were used to quantify the color distribution in each dSph and ensure that the spectroscopic targets span the color range, and thus the selection is as representative in metallicity as possible. For the Leo I fiducial, we simply adopted the fiducial for M15 = NGC 7078 (Da Costa & Armandroff 1990), which has $[Fe/H] = -2.02$, because it lies roughly along the middle of the Leo I RGB. Because of the age-metallicity degeneracy in the CMD, the old (14 Gyr), metal-poor M15 RGB fiducial lies along the same part of the CMD as the RGB of the younger (4 Gyr), intermediate-metallicity Leo I RGB fiducial. Yale isochrones with $[Fe/H] = -1.28$ and ages 2 and 4 Gyrs have been plotted on the Leo I CMD to illustrate the young ages of the stars on blue edge of the RGB. For the Leo II fiducial, we adopted the fiducial of the Galactic globular cluster M68 = NGC 4590 (McClure, et al. 1987), which has $[Fe/H] = -1.92$, with an additional shift of 0.1 mag in $(B-V)$ so that it ran along the middle of the Leo II RGB.

All dSph stars selected for observation have $-3 \leq V - V_{HB} \leq -2$ and $1.0 \leq V - I \leq 1.5$, where V_{HB} is the V-band magnitude of the horizontal branch. In order to have the spectroscopic sample be as representative as possible with respect to color and metallicity, we chose stars with the aim of spanning the same distribution in color as the entire sample. To quantify this, we defined the color difference, $\Delta_{(B-V)}$, to be the B-V color of an individual star minus the B-V color of the fiducial RGB at the V-magnitude of the star. We used B and V-band photometry to select Leo II stars, and V and I-band photometry to select Leo I stars for spectroscopy. Note that the images in the RI filters of the Leo II fields were taken under non-photometric conditions and remain uncalibrated. In designing the slit mask configurations, we attempted to match the distribution in $\Delta_{(V-I)}$ and $\Delta_{(B-V)}$ for Leo I and Leo II, respectively. The histograms of color differences are illustrated in Figures 3 and 4.

Candidate red giants in the Leo I and Leo II dSphs were chosen for spectroscopic observations based on their location in the CMD and position in the slit mask field-of-view, which was $4' \times 7'$ on the sky. Using five slit mask orientations for Leo I we covered the core radius of the galaxy and 83% of the tidal radius along the east-west axis; only 56% of the tidal radius was covered along the north-south axis. Leo II was observed with four slit mask orientations, which covered an area of $7' \times 7'$ on the sky; this covered all of the core radius of the galaxy and approximately 80% of the tidal radius.

3 OBSERVATIONS

We obtained low-dispersion spectra of red giants in Leo I and Leo II dSphs using the Keck I 10-meter telescope and LRIS (Oke et al. 1995) during 2 runs; run 1 was on 8 February 2002, and run 2 was on 5 March 2003 (UT). The pixel scale of the CCD in the spatial direction was $0.215''/\text{pixel}$. The CCD was read out using two amplifiers with gains of 1.97 and $2.10 e^-/\text{adu}$, and readnoises of 6.3 and $6.6 e^-$, for the left and right amplifiers, respectively. We used the 1200 l/mm grating blazed at 7500 \AA , which gave a dispersion of $0.62 \text{ \AA}/\text{pix}$ and resolution of 1.55 \AA ($R \approx 14,000$). The GG495 filter was used to block second-order light. In multi-slit mode, the available field of view was $4' \times 7'$ for a minimum spectral coverage extending from 8355 – 8890 \AA . The slit widths were $1.0''$ and the minimum slit length was $6.0''$. We were able to observe approximately 20 to 30 stars per multi-slit mask. In the long-slit mode which was used for some of the calibration stars, the slit was $1.0'' \times 3.0'$. The typical seeing was $0.8''$ as measured by the FWHM of the profile of the spectra along the spatial direction.

Exposure times were 4×900 sec for most masks. Observations of one field in Leo I was only 2×900 sec due to a pointing problem which caused the stars to be off center of the slits for 2 exposures which were not used in the analysis. Due to LRIS's sizable flexure, we obtained spectra of the Ne-Ar arc lamp and a halogen flat after the final exposure on each target for calibration purposes. In addition, a radial velocity standard and telluric standards (rapidly rotating, B-type stars) were observed in long-slit mode. Spectra of red giants in four Galactic globular clusters were also taken using the slit mask configuration to place our equivalent width measurements on the well-defined scale of Rutledge et al. (1997a and 1997b; hereafter R97a and R97b).

4 DATA REDUCTION

The usual CCD image reduction procedures of overscan fitting, overscan subtraction, and zero subtraction were done using routines we developed in the Interactive Data Language (IDL)². The two amplifiers have different zero levels, which needed to be taken into account when creating the zero image. Two bad pixels caused bleeding on the Amp 1 side and created structure in the zero image. Further reductions followed those outlined in the data reduction tutorial on the LRIS web page (<http://\alamoana.keck.hawaii.edu/inst/lris>) and Massey et al. (1992) with slight modification in reduction parameters. Cosmic ray removal, flat fielding in two dimensions, extraction of spectra from two dimensions to one dimension, and normalizing the continuum to unity were performed with tasks in the IMRED package of the Image Reduction and Analysis Facility (IRAF)³.

Distortion in both the dispersion direction (x axis) and spatial direction (y axis) had to be corrected in the 2-D spectra before the spectra were extracted to 1-D. We mapped and corrected distortions along the y axis of spectra using IRAF's IDENTIFY, REIDENTIFY and FITCOORDS tasks on halogen flats taken directly after each exposure. We applied the distortion correction to the arc and

² IDL is commercial software sold by Research Systems, Inc.

³ IRAF is freely distributed by the National Optical Astronomy Observatories, which is operated by the Association of Universities for Research in Astronomy, Inc., under cooperative agreement with the National Science Foundation.

object exposures using the TRANSFORM task. To correct the distortion along the x axis, we used the IRAF-based task XDISTOR (Greg Wirth 2002, private comm.) adapted to the specifications of the data set. This task uses the strong night sky lines in the object spectra, or arc lines in the Ne-Ar spectra, to map and correct the distortion in the spectral direction for each aperture. The distortion correction was very accurate; after correction, the shifts in the centroids of typical arc lines over the most distorted apertures at the top and bottom of an image were $\lesssim 0.05$ pixels, which is $\lesssim 1.6\%$ of the FWHM.

Because the spectrograph has sizable flexure over the 4×900 sec observation times, the wavelength solution for each aperture was determined using bright night sky lines in the spectra themselves rather than the arc lamps taken after each set of exposures. Most of the night sky lines were blended at our 0.62 \AA/pix dispersion so we did not adopt the wavelengths of the sky lines determined from high-dispersion spectra (e.g., Osterbrock et al. 1996, Osterbrock & Fulbright 1997). Instead, we calculated the central wavelength for approximately 40 bright, night-sky emission lines in 25 apertures using Ne-Ar spectra taken immediately after an exposure. Each stellar spectrum was wavelength calibrated by using 25 to 40 night sky lines fit with a spline3 (1st order) fit, which yielded wavelength solutions with typical RMS residuals of 0.03 \AA . Each slit had a unique wavelength coverage that fell somewhere in the range of $7770 - 9440 \text{ \AA}$.

Different spectra for individual targets were combined using the IRAF SCOMBINE task rejecting outliers at the 3σ level. The continua of all spectra were fit with cubic splines, rejecting absorption features, and normalized to unity with the CONTINUUM task to produce the final calibrated spectra. We measured the average signal-to-noise ratio per pixel (SNR) in each spectrum by calculating the RMS in two wavelength windows where absorption features are weak, $8580 - 8620 \text{ \AA}$ and $8700 - 8800 \text{ \AA}$, and averaged the results. The mean SNR was 18 for Leo I stars and 23 for Leo II stars, and the range was $6 \leq \text{SNR} \leq 42$ for all of the observed dSph stars. Abundances were only determined for stars with SNR greater than 10 and for which at least the two strongest Ca II lines were observed. These criteria reduced the number of stars analyzed from 121 to 102 for Leo I and from 90 to 74 for Leo II.

5 DATA ANALYSIS

In this section the measurement of heliocentric velocities, the reduced equivalent widths of the Ca II lines, and metallicities are discussed.

5.1 Heliocentric Velocities

We verified membership of the stars in each dSph by deriving their radial velocities because the intrinsic velocity dispersions of these galaxies are well-defined, $\sim 10 \text{ km/s}$, and very different than stars in the Milky Way. We computed heliocentric radial velocities, v_{helio} , by cross-correlation (e.g. Tonry & Davis 1979) with a spectrum of IAU radial velocity standard HD 12029 (K2III spectral type, $B-V = 1.24$, $v_{\text{helio}} = 40.0 \text{ km sec}^{-1}$) for Run 1 and HD 35410 (G9III spectral type, $B - V = 0.95$, $v_{\text{helio}} = 20.3 \text{ km sec}^{-1}$) for Run 2. We used our IRAF task RVITERATE to iterate the cross-correlation performed by the IRAF FXCOR task. RVITERATE changes the window of the observed wavelength in the object spectrum over which the correlation is performed until the rest frame window of $8200 - 9000 \text{ \AA}$ was used in both the template

and object spectrum. A ramp filter was used to filter out the large wavelength fluctuations from any telluric bands on scales $\approx 40 \text{ \AA}$, and small scale fluctuations from random noise.

For 121 stars observed in Leo I, the median velocity error is 9.2 km sec^{-1} . We found the average heliocentric velocity, weighted by the errors, is $\langle v_{\text{helio}} \rangle = +282.6 \pm 9.8 \text{ km sec}^{-1}$. Mateo, et al. (1998) found $\langle v_{\text{helio}} \rangle = +287.0 \pm 2.2 \text{ km sec}^{-1}$ based on high-dispersion spectra of 15 RGB stars. For 90 stars observed in Leo II, the median velocity error is 8.5 km sec^{-1} . We found $\langle v_{\text{helio}} \rangle = +85.8 \pm 8.4 \text{ km sec}^{-1}$. Vogt, et al. (1995) found $\langle v_{\text{helio}} \rangle = +76.0 \pm 1.3 \text{ km sec}^{-1}$ and a dispersion of $\sigma_{v_{\text{helio}}} = 6.7 \pm 1.1 \text{ km sec}^{-1}$ based on high-dispersion spectra of 31 red giants. The differences between the mean velocities for this work and those of earlier work are not significant given the differences in the spectral resolution between the data sets. Our velocity resolution is 54 km sec^{-1} while that of Vogt et al. (1995) and Mateo, et al. (1998) is 9 km sec^{-1} . For the case of Leo I, the great velocity dispersion (see Figure 5) as well as the small number of stars observed by Mateo et al. could also contribute to the differences in derived average velocities. As we are more concerned with the deviations from the average rather than the true velocities of the galaxies, we have used our mean velocities for membership determination.

There can be systematic shifts in the radial velocities of stars observed through multi-slit masks (e.g., Tolstoy et al. 2001) if stars are not centered on the slits. Since our computed velocity dispersions are similar to those determined from long slit work, we can assume that our stars were typically well-centered on the slits. There are no obvious correlations between a star's velocity residual from the average v_{helio} and its magnitude, color or radial position within the galaxy.

Of the 121 stars in Leo I, 90 have v_{helio} within 3σ of the average velocity, and all stars have v_{helio} within 5σ . Of the 90 stars observed in Leo II, 83 have v_{helio} within 3σ of the average velocity, and all stars have v_{helio} within 5σ . Figure 5 illustrates the velocity distributions for each galaxy; as no obvious velocity outliers are apparent, we can assume each star observed is a dSph member.

6 CHEMICAL ABUNDANCE ANALYSIS

6.1 The Reduced Equivalent Widths of the Ca II Triplet

The Ca II triplet absorption lines at 8498 , 8542 and 8662 \AA are very strong in spectra of red giant stars, with equivalent widths of order a few Angstroms. Figures 6 and 7 show how the strengths of the Ca II lines compare to strengths of the Fe I lines in low and high-dispersion spectra. The most widely used method of relating the equivalent widths of the Ca II triplet to metallicity is given by Rutledge et al. (1997a and 199b; R97a and R97b, respectively). R97a measured the reduced equivalent widths, W' (defined below) of the Ca II triplet for stars in 52 Globular clusters and, in R97b, found the empirical relationship between W' and $[\text{Fe}/\text{H}]$ for the metallicity scales of Carretta & Gratton (1997, CG97) and Zinn & West (1984, ZW84).

We have followed the R97a definition of sum of the equivalent widths of the Ca II lines,

$$\sum W = 0.5 W_{8498} + W_{8542} + 0.6 W_{8662}. \quad (1)$$

Lower weight is given to the weaker lines to yield higher precision in the final index. The pseudo-equivalent widths and errors

of the Ca II lines were measured with an IRAF-based FORTRAN code named EW (G. Da Costa 1999, private comm.). The program assumes the same line window regions used by R97a and the continuum windows used by Armandroff & Zinn (1988).

We were able to measure all three Ca II lines in 155 of the observed spectra, but in 20 spectra we could only accurately measure the equivalent widths of the two strongest lines at 8542 Å and 8662 Å due to their lower SNRs. In order to obtain a measurement of $\sum W$ for these stars, we determined the relationship between $\sum W$ and the equivalent widths of the two strongest lines from the cluster stars with high SNR spectra. We found the relationship was linear with

$$\sum W = m (W_{8542} + 0.6 W_{8662}) + b, \quad (2)$$

where $m = 1.104 \pm 0.018$ and $b = 0.138 \pm 0.060$ Å were the coefficients derived from least-squares fitting analysis that incorporated errors on both values (The data and fit are shown in Figure 8).

The strengths of the Ca II lines are most sensitive to stellar gravity and abundance and much less sensitive to effective temperature (e.g. Díaz, Terlevich & Terlevich 1989, Jorgensen et al. 1992, and Cenarro et al. 2002). Using the “reduced equivalent width”, W' , as defined by Armandroff & Da Costa (1991) allows the effect of gravity to be removed to first order. The reduced equivalent width of a star is defined to be

$$W' = \sum W + 0.64(V - V_{\text{HB}}), \quad (3)$$

where V and V_{HB} are the V-band magnitudes of the observed stars and the cluster or dSph horizontal branch, respectively. R97a found a linear relationship existed between $(V - V_{\text{HB}})$ and $\sum W$ for stars of an individual globular cluster, and that the slope of 0.64 ± 0.02 Å/mag was insensitive to the metal abundance of the cluster.

In order to tie our W' measurements to the well-calibrated and often utilized scale of R97a, we observed 41 red giants in four Galactic globular clusters. Table 3 lists the clusters, and gives the horizontal branch magnitude, the metallicity, the average W' and error for the cluster from R97a, and the W' from this investigation. Values of W' for NGC 1904 (M79), NGC 4590 (M68), and NGC 6171 (M107) are listed in R97a, but they did not include NGC 5272 in their study. However, B04 observed stars in NGC 5272 in the Ca II recalibration project at the UCO Lick and W.M. Keck Observatories and placed its measurements on the R97a scale. The [Fe/H] values for M79, M68 and M3 listed in Table 3 come from Bosler (2004; see section 6.2) and were determined from atmospheric abundance analysis of Fe II lines in high-dispersion spectra. The [Fe/H] value listed for M107 is from the R97b calibration of W' to [Fe/H] using the Carretta & Gratton (1997, hereafter CG97) metallicity scale. Table 2 lists the individual cluster stars and their measured equivalent widths in this study and in that of R97a/R97b. The data on $\sum W$ for individual stars in the R97a study was provided by J. Hesser (1999, private communication to T. Smecker-Hane). Note that because of geometrical constraints inherent in using slit masks, our sample of cluster stars is not identical to that observed by R97a.

Comparing W' for the 23 individual cluster stars that the two data sets have in common, we find

$$W'_{\text{R97}} = 1.006 (\pm 0.025) W'_{\text{LRIS}} + 0.267 (\pm 0.063), \quad (4)$$

where W'_{R97} is the value of W' on the scale of R97a and W'_{LRIS} is our observed value. The least-squares fitting technique incorporated the errors in both W'_{LRIS} and W'_{R97} . The data and fits are shown in Figure 9. The small differences in the equivalent widths

measured by us and R97a are not surprising, because the spectral resolution of our observations are significantly different (our resolution is 1.55 Å compared to their resolution of 4 Å), and the Ca II lines are pressure broadened and partially resolved at this resolution. In addition, the equivalent widths are measured relative to the pseudo-continuum (neither their spectra nor ours were flux calibrated) and thus are slightly sensitive to the spectrograph’s efficiency. The differences we find are comparable to those R97a find between their work and others (e.g., Table 6 in R97a) and are attributed to differences in line fitting technique as well as slight differences in the instrumental resolution and throughput properties of the spectrographs and detectors used in acquiring the two different data sets.

The W' values for Leo I and Leo II were determined using V_{HB} values from the literature, and the final W' values were placed on the scale of R97a to remain consistent with other literature on the Ca II triplet. For the Leo I dSph, we assumed $V_{\text{HB}} = 22.60 \pm 0.12$ mag based on the RR Lyrae work of Held, et al. (2001), and for the Leo II dSph, we assumed $V_{\text{HB}} = 22.17 \pm 0.14$ mag based on the RR Lyrae work of Siegel & Majewski (2000). Note that V_{HB} does change with the age of a stellar population, but this change is small as long as the ages are $\gtrsim 3$ Gyr. This is true for the Leo II dSph, where ages are $\gtrsim 7$ Gyr (Mighell & Rich 1996), but the Leo I dSph does have a few stars as young as ~ 2 Gyr (Gallart et al. 1999b, Dolphin 2002). The HB clump in Leo I has a V magnitude that is ~ 0.15 magnitudes brighter than the RR Lyrae stars. Thus adopting the RR Lyrae magnitude will only result in a 0.05 dex systematic metallicity error, in the sense that the true metallicity of a younger stars would be more metal-rich than that inferred. This error is small relative to the other errors, and hence is not taken into account in the present analysis.

Note that although the Ca II lines are easy to observe in low resolution and low signal-to-noise spectra, abundances *cannot accurately be derived from modelling the the Ca II lines* due to the complexity of their formation. Additionally, high dispersion spectra can resolve the weaker iron and neutral calcium lines. These lines can be accurately modelled to derive stellar abundances, but these observations require long exposure times and become impractical for surveying large numbers of faint, distant stars. Thus, if one intends to use observations of the Ca II lines to determine stellar abundances, an empirical relationship must exist between the equivalent widths of the Ca II lines are actual stellar abundances.

6.2 Metallicity Calibration

Though the R97b calibration is widely used to derive abundances from the Ca II triplet, Rut97b points out that the two metallicity scales for which calibrations were derived (CG97 and ZW84) can yield dramatically different values of [Fe/H] for a given W' . Additionally, R97b points out that there is no reason to assume that the relationship should be linear (as in the case of the CG97 metallicity scale) or non-linear (as in the case of the ZW84 metallicity scale). They discussed an apparent non-linearity between the metallicity scales of ZW84 and also of Cohen (compilation in Frogel et al. 1983), who examined more metal-rich stars than were examined in other metallicity literature data. Kraft & Ivans (2003, hereafter KI03) also found a possible non-linearity in the Ca II to [Fe/H] relationship for metal-rich stars in their investigation. In Cole et al. 2004, the effects of line fitting on the equivalent widths of the Ca II lines for metal-rich stars also caused slight shifts in the empirical relationship between Ca II and [Fe/H]. One of the possibilities noted in R97b for a non-linear relationship between W' and

[Fe/H] for metal-rich stars is a changing [Ca/Fe] as a function of [Fe/H].

Figure 10 plots [Ca/Fe] versus [Fe/H] for Galactic clusters from B04 and Galactic field stars observed by Edvardsson et al. (1993) and Fulbright (2000, 2002). The [Ca/Fe] in Milky Way stars changes as a function of [Fe/H], and at [Fe/H] ≈ -0.8 , the [Ca/Fe] value to change more rapidly as a function of [Fe/H].

One major problem with determining a standard relationship between Ca II and [Fe/H] for stars with a range of ages and metallicities is that the equivalent widths of the Ca II lines are a function of, among other things, [Ca/H] for RGB stars (see Jorgensen et al. 1992). When one uses the equivalent widths of the Ca II lines to infer [Fe/H], one assumes some constant or smooth [Ca/Fe] relationship. Applying the existing Ca II to [Fe/H] calibration to extragalactic stars is extremely dubious because we have very little information about the star formation histories and star to star variations in abundance ratios for these galaxies.

Bosler (2004) reinvestigated the widely-utilized relationship between W' and [Fe/H] for 21 Galactic cluster with a wide range of ages (2 to 14 Gyrs) and metallicities ($-2.5 \leq [\text{Fe}/\text{H}] \leq +0.2$). W' values, as mentioned in the previous section, were measured for stars in the same 21 clusters to build an internally self-consistent data set, and equivalent widths were transformed to the scale of the R97a data because their Ca II measurements are so widely utilized. Figure 12 illustrates the empirical relationship between W' and [Fe/H] for the B04 clusters along with the residuals for each of three different fits to the data - a linear fit to only the globular clusters (analogous to the R97b fit to the CG97 metallicity scale) and a linear and quadratic fit to all clusters.

Note that the relationship found by R97b using the metallicity scale of CG97, was based solely on Galactic globular cluster (GGC) stars; the relationship they found, for comparison, was

$$[\text{Fe}/\text{H}]_{\text{CG97}} = -2.66(\pm 0.08) + 0.42(\pm 0.02) \times W'. \quad (5)$$

This fit is similar to the fit to our GGCs (see Table 4). The relationship appears fairly smooth and linear, but the addition of the younger, metal-rich Galactic open clusters (GOCs) with [Fe/H] > -0.8 , indicates that [Fe/H] is not truly a linear function of W' . Since most work on the Ca II triplet calibration was done using GGCs, mostly with [Fe/H] < -0.8 , a linear fit is indicated by a solid line in Figure 12. If this calibration based on only the GGCs is used to infer the abundances of the metal-rich open clusters the derived metallicity would be lower by approximately 0.3 dex.

In fact, the relationship is linear up to [Fe/H] ≈ -0.08 , but if all of the data are included, the relationship becomes quadratic. The linear fit to only the GGCs, the linear fit to all clusters, and the quadratic fit to all of the clusters are listed in Table 4 along with the mean error of unit weight, m.e.1⁴, rms and the Chi-squared per degree of freedom, χ_ν^2 , values for the regressions. Notice that linear fit to all of the clusters has the largest m.e.1 value implying that the either the errors have been underestimated or the fit to the W' to [Fe/H] relationship is really non-linear and is most likely effected by the varying [Ca/Fe] values for the different clusters (ie. it is dependent upon star formation history).

⁴ The m.e.1 = $(\sum \epsilon^2/\sigma^2)^{0.5} (N-1)^{-0.5}$, where ϵ is the deviation of the [Fe/H] value for each cluster from the predicted value based on the fit, σ is the uncertainty in W' and [Fe/H] values, N is the total number of clusters. A value of one indicates that the scatter is consistent with the observational errors, and a higher value implies that the errors have been underestimated or that the relationship is nonlinear

In order to circumvent the fundamental dependence on [Ca/Fe] ratios built into the current Ca II calibrations, B04 derived an empirical relationship between Ca II and [Ca/H]. It is important to note that the [Ca/H] values *were not derived from the Ca II lines*. The [Ca/H] values were determined from atmospheric abundance analysis of neutral calcium (Ca I) lines measured in high-dispersion spectra. The abundances derived for the Ca I lines were also corrected for non-LTE effects in the analysis. In B04, non-LTE effects on the Ca I, Fe I and Fe II lines were closely examined. These effects on derived abundances arise from the fact that some high energy UV photons from deep within the stellar atmosphere penetrate the upper levels of the atmosphere and break the LTE assumption used in the modelling the line formation. The changes in temperature between the model and the 'true' atmosphere effects the abundances derived by the neutral lines more strongly than the abundances derived by ionized lines. As a result, abundances derived from Fe II lines best represent the 'true' abundances, while those from Fe I and Ca I lines will be effected by the non-LTE atmosphere of the star. However, B04 found that the ratio of Ca I to Fe I ([Ca/Fe]_I) is not strongly effected by variations in stellar temperatures as both species are being effect similarly. Therefore, the 'true' [Ca/H] value was defined as

$$[\text{Ca}/\text{H}] = [\text{Ca}/\text{Fe}]_{\text{I}} + [\text{Fe}/\text{H}]_{\text{II}}, \quad (6)$$

where [Fe/H]_{II} is the iron abundance derived from Fe II lines. This 'true' value of [Ca/H] is not affected by the non-LTE effects described above.

The calibration is based on stars in 15 Galactic globular and open clusters with ages from ≈ 2 to 14 Gyr and $-2.2 < [\text{Ca}/\text{H}] < +0.2$ making it an extremely robust calibration of the Ca II triplet to abundances. The regression between W' and [Ca/H] is

$$[\text{Ca}/\text{H}] = -2.778(\pm 0.061) + 0.470(\pm 0.016) \text{ dex}/\text{\AA} \times W'. \quad (7)$$

This relationship is independent of the ages of the clusters for clusters older than a few Gyrs. It can be applied to Galactic and extragalactic stars without concern for the effects of variations in [Ca/Fe] ratios in the stars. Therefore, it is independent of the star formation history of the system. Additionally, the new calibration includes stars from from both GGCs and GOCs to insure that it is valid over a wide range of ages and metallicities.

Figure 11 shows the linear fit to the calibration with an root-mean-square (rms) scatter of 0.13 dex, an mean error of unit weight (m.e.1) = 1.06. The residual to the fit is also illustrated. The Chi-squared per degree of freedom, $\chi_\nu^2 = 1.87$. We also applied a quadratic fit to the data and found that the coefficient on W'^2 is statistically insignificant compared to the uncertainties in the fit, which are over twice as large. The values of Ca II and [Ca/H] for clusters used in the calibration are shown in Table 5. Note that the [Ca/H] values listed were derived from atmospheric abundances analysis of high dispersion spectra, while the value of W' were derived from low-dispersion spectra of stars in the same clusters.

6.3 Which is Preferable - the Calibration to [Ca/H] or [Fe/H]?

As the star formation histories and the effect of galactic winds in the Leo I and Leo II are not yet well-defined, we do not yet know what the element ratio, [Ca/Fe], is as a function of metallicity. Thus it would be inappropriate to assume that they follow the same [Ca/Fe] verses [Fe/H] relationship as that found for the Galactic Globular clusters used by R97 to calibrate the Ca II equivalent widths to [Fe/H]. The new calibration to [Ca/H] has a very small RMS that

can be explained mostly by observational error rather than systematic variations that depend on [Ca/Fe] and is also independent of stellar ages (for ages ≥ 3 Gyrs) and star formation history. Therefore, the new calcium calibration will be used to derive abundances in this work; however, [Fe/H] values on the scale of CG97 will also be listed for reference to those still compelled to use the existing calibration.

As an aside, there is really no compelling reason that stellar metallicities should be specified in terms of [Fe/H]. The iron abundance became the observational spectroscopist's way of characterizing the overall metallicity of a star in a one-dimensional way, because iron and iron-peak elements are the most plentiful lines and are easiest to measure in optical and near-IR spectra. In fact, stellar opacities are controlled by the entire range of elements; the iron and iron-peak elements whose outer electrons are most easily ionized, but, more importantly, the CNO and alpha-elements, which are most abundant by number highest and which provide the majority of the transition electrons. Additionally, the abundance ratios [CNO/H] in high metallicity stars is an important parameter because it also controls the amount of energy generated from the CNO cycle.

7 RESULTS

7.1 Metallicity Distribution of Leo I

The observed range in reduced equivalent widths for Leo I dSph stars is $0.83 \leq W' \leq 4.63 \text{ \AA}$. Tables 6 and 8 list the parameters of each star (V, V-B, Ra, Dec, SNR and V_{Helio}) and the spectroscopic values (W' , [Fe/H]_{CG97}, and [Ca/H]), respectively. Note that the W' values have been scaled to the work of R97a, which has been used as a standard in the literature. As shown in Figure 13, the inferred metallicities range from $-2.39 \leq [\text{Ca}/\text{H}] \leq -0.60$ for 102 stars. The average metallicity is $[\text{Ca}/\text{H}] = -1.34 \pm 0.02$, and the observed spread is 1.20 dex. The median random [Ca/H] error is 0.10 dex, and the median total error is 0.17 dex per star. Placing our Ca II values on the [Fe/H] scale of CG97, Leo I has a mean [Fe/H]_{CG97} = -1.34. Calcium abundances have not been studied extensively in Leo I. However, Shetrone et al. (2003) found [Ca/Fe] = +0.15 and +0.02 dex ($\sigma \approx 0.15$ dex) and [Fe/H] = -1.52 and -1.06 dex, respectively, ($\sigma \approx 0.1$ dex) for two stars in Leo I based on abundance analysis of high-dispersion spectra. This implies [Ca/H] = -1.20, which is slightly more metal-rich than the average we found for 102 stars, but the intrinsic spread we see and the small number of stars used by Shetrone et al. could account for the difference.

Suntzeff et al. (1986) found an average metallicity of [Fe/H] = -1.5 ± 0.25 from the strengths of the Ca H and K lines in low dispersion spectra of two red giants, and this corresponds to [Ca/H] = -1.41 assuming an average [Ca/Fe] from Shetrone et al. (2003)'s two stars. This value is more metal-poor than the Shetrone et al. value, and it is in agreement with our observed values given the small number of stars used.

Leo I has a roughly Gaussian-shaped metallicity distribution with an asymmetric over-abundance at the metal-rich end and a slightly extended metal-poor tail. We fit the metallicity distribution function with a Gaussian distribution of the form:

$$N(m) \propto \exp\left(-\frac{(m - m_0)^2}{2\sigma_m^2}\right), \quad (8)$$

where $m = [\text{Ca}/\text{H}]$, in order to determine the centroid of the distribution, m_0 , and the observed dispersion, σ_m . For Leo I, a non-

linear least-squares fit gives $m_0 = -1.35 \pm 0.02$, and $\sigma_m = 0.24 \pm 0.03$. The fit is shown in Figure 13. Given that the median random measurement error is $\sigma_{\text{rand}} = 0.10 \pm 0.03$ dex, the intrinsic metallicity dispersion in Leo I is equal to

$$\sigma_{m,i} = (\sigma_m^2 - \sigma_{\text{rand}}^2)^{\frac{1}{2}} = 0.26 \pm 0.03 \text{ dex} \quad (9)$$

The implied intrinsic spread in metallicity in Leo I is approximately $2 \text{ FWHM} = 4.71 \sigma_{m,i} = 1.22 \pm \text{dex}$.

Figure 14 shows the position of stars in the CMD as a function of their metallicity. The fiducials for the GGCs M5 = NGC 5904 ([Ca/H] = -0.96, age = 14 Gyr) and M68 ([Ca/H] = -1.78, age = 14 Gyr) are plotted for reference in the CMD. The most metal-poor stars tend to lie along the blue half of the RGB, but stars with [Ca/H] $\gtrsim -1.5$ occupy a wide swath in color. At any given color, there are stars with a mix of metallicities, which probably reflects the fact that the red giants in Leo I have a large range in ages (many Gyrs).

A large spread in metallicity has not been assumed in most studies of the Leo I CMD (Lee, et al. 1993, Gallart, et al. 1999b, Siegel & Majewski 2000), which either assumed a constant metallicity or a much narrower range. Including a 1.2 dex metallicity spread will dramatically affect the inferred star-formation history.

Dolphin (2000) did include metallicity evolution as a variable in his CMD modelling of the Leo I and Leo II CMDs. He photometered archival WFPC2 images and obtained a CMD that spanned the tip of the RGB to the oldest main-sequence turnoff. (The photometric errors at the level of the oldest MSTO are much larger in the Leo I data, and hence the SFH for ages $\gtrsim 9$ Gyr in the Leo I dSph was not as well determined as for the Leo II dSph.) Dolphin modelled the Hess diagram—the density of stars in the CMD—using Padova isochrones (Girardi, et al. 2000), which he interpolated on a finer grid of metallicity (0.15 dex binning). He has kindly provided the simulated data from his best fit models.

We have applied to Dolphin's model CMD the same color and magnitude selection criteria used to select the Leo I spectroscopic sample (note that the color selection did not eliminate any RGB stars), computed the metallicity distribution, and convolved it with our median random [Ca/H] errors. The resulting metallicity distribution function is shown in Figure 15. The shapes of the model and observed distributions are similar, with both having slight excesses at the metal-rich end and a metal-poor tail. There is a gap at approximately [Fe/H] = -1.3 in the predicted distribution that does not exist in the observed distribution. Note that comparing our [Ca/H] values or the inferred [Fe/H]_{DG97} yields the same discrepancy between the model and observations. More recent photometry from Held et al. (2000) indicates a significant metal-poor population based on the existence of an extended blue horizontal branch that had not been previously observed. The exclusion of this metal-poor population in the synthetic CMD used to predict the dispersion may account for the missing metal-poor stars. The peak of the model is significantly more metal-rich than the observed distribution. A Gaussian fit to the model gives $m_0 = -1.0$ and $\sigma_m = 0.17$ dex, although a Gaussian is obviously a poor assumption for this model distribution.

Dolphin did examine [Fe/H] values rather than [Ca/H], but the peak of the distribution does not account for potential [Ca/Fe] differences that may exist in the stars. Assuming the median [Ca/H] from our observations and [Fe/H] from Dolphin's model CMD, the typical abundance ratio would be [Ca/Fe] = -0.36, which is a much lower than the value established by Shetrone et al. (2003) for two stars. Additionally, this value is extremely low compared to the values of any Galactic or dSph stars previously observed; a [Ca/Fe]

of -0.36 is lower than the predicted ratio due to Type Ia supernovae alone, which is -0.31 (Thielemann et al. 1986; model W7). If the average $[\text{Ca}/\text{Fe}]$ from Shetrone et al. is added to the $[\text{Fe}/\text{H}]$ values of Dolphin to yield a representative $[\text{Ca}/\text{H}]$, the distribution is shifted more to the metal-rich end of the histogram causing an even *larger discrepancy* between the model and observation. Note that this discrepancy between the model and observations would still exist if the widely used Ca II to $[\text{Fe}/\text{H}]$ calibration were used to derive stellar abundances.

What could be the cause of the discrepancy? In the CMD modelling, the best fitting values of the metallicity and star-formation rate as a function of time are determined by matching the density of stars in finely-binned magnitude and color intervals in the observed and modelled CMD. In the process, the portions of the CMD with the largest numbers of stars are given the greatest weight. These are the main-sequence turnoff and unevolved main-sequence regions. The width in color of the main-sequence turnoff and upper main sequence is governed by the spread of ages, metallicities, and the assumed fraction and characteristics of unresolved binary systems. A high fraction of binaries causes a spread in the color of the unevolved main sequence, which could be interpreted as an intrinsic spread in metallicity. Thus the assumptions made about the unresolved binaries could affect the inferred distribution of metallicities. In addition, the models themselves could be source of problems because the color-temperature relationships used to transform from the theoretical to observed plane are still controversial.

7.2 Metallicity Distribution of Leo II

The observed range in the reduced equivalent widths for Leo II stars is $0.36 \leq W' \leq 4.65 \text{ \AA}$. Tables 7 and 9 list the parameters of each star (V , $V-B$, R_a , Dec , SNR and V_{Helio}) and the spectroscopic values (W' , $[\text{Fe}/\text{H}]_{\text{CG97}}$, and $[\text{Ca}/\text{H}]$), respectively. Note that the W' values have been scaled to the work of R97a. Figure 16 shows the range in metallicities is $-2.61 \leq [\text{Ca}/\text{H}] \leq -0.59$, and the observed spread is 1.29 dex. The average metallicity in the Leo II dSph is $[\text{Ca}/\text{H}] = -1.65 \pm 0.02$, much more metal-poor than the median in the Leo I dSph. Placing our Ca II values on the $[\text{Fe}/\text{H}]$ scale of CG97, Leo I has a mean $[\text{Fe}/\text{H}]_{\text{CG97}} = -1.59$. The median random error is 0.10 dex and the median total error is 0.17 dex per star, and the intrinsic metallicity dispersion is 1.01 dex. Leo II also has an asymmetric distribution with a steep cut off on the metal-rich end, excesses at the metal-poor end, and an indication of metal-rich and metal-poor tails.

Suntzeff, et al. (1986) found an average $[\text{Fe}/\text{H}] = -1.9 \pm 0.2$ based on the Ca H and K strengths of 3 red giants. With an unknown typical $[\text{Ca}/\text{Fe}]$ value for the Leo II stars, it is impossible to directly compare the two results. However, assuming an average $[\text{Fe}/\text{H}] \approx -1.90$ from Suntzeff and our $[\text{Ca}/\text{H}]$ would imply $[\text{Ca}/\text{Fe}] \approx +0.3$, which is similar to the values for older stars in Milky Way globular clusters and field stars. Mighell & Rich (1996) inferred an average $[\text{Fe}/\text{H}] = -1.60 \pm 0.25$ using the shape of the RGB in the V , I -band CMD. From interpolating globular cluster fiducial RGBs, they derived an intrinsic spread in $[\text{Fe}/\text{H}]$ of 0.9 dex, which is similar to the spread in $[\text{Ca}/\text{H}]$ of 1.0 dex derived here. This agreement is understandable because the color and shape of the RGB are much more sensitive to metallicity than age for ages $\gtrsim 7$ Gyr, the age of the youngest stars in the Leo II dSph.

Figure 17 illustrates the range in $[\text{Ca}/\text{H}]$ across the RGB. Again, the large dispersion in metallicity at a given color indicates the stars span a range of ages.

We also compared the observed metallicity distribution of the

Leo II dSph with predictions of CMD modelling from Dolphin (2002). Since both the model and observations have a very non-Gaussian distribution, we did not attempt to compute Gaussian fits. Figures 16 and 18 show that the shape of the model and observed distributions are similar with excesses at the metal-poor end and a steeper drop at the metal-rich end. Leo II is the smaller of the two dSphs, having $M_V = -9.6$ compared to $M_V = -11.9$ for Leo I. The decreased number of stars at high metallicities in Leo II may be due to its greater inability to retain gas after star formation had progressed for a while. Analyzing the CMD from the same set of WFPC2 images, Mighell & Rich (1996) and Dolphin (2002) both inferred that Leo II stopped forming stars ≈ 7 Gyr ago, compared to the Leo I dSph which only stopped forming stars ~ 2 Gyr ago.

Though the shapes of the distributions are similar, the model has a median which is more metal-rich than the median of the observed distribution. Assuming the $[\text{Ca}/\text{H}]$ from this work and $[\text{Fe}/\text{H}]$ values from Dolphin are taken to be typical values of the Leo II stars, it would imply a $[\text{Ca}/\text{Fe}] \approx -0.49$. The large discrepancy between the abundances derived from CMD modelling and the observations also exists for Leo II stars, and it is even larger than those of the Leo I stars and much lower than the predicted abundance ratios from Type Ia supernovae. Again, if we compare our $[\text{Fe}/\text{H}]_{\text{CG97}}$ values with those of Dolphin, the discrepancy still exists, and is approximately the same size. Though there are no available data on abundance ratio of Leo II, the extremely low $[\text{Ca}/\text{Fe}]$ value from comparing the model results is dramatically different than those derived by comparing $[\text{Ca}/\text{H}]$ to spectroscopic $[\text{Fe}/\text{H}]$ abundances (Shetrone et al. 2003), which yields $[\text{Ca}/\text{Fe}]$ more typical of Galactic and Local Group stars.

8 SUMMARY

We have determined calcium abundances for 102 RGB stars in the Leo I dSph galaxy and 74 RGB stars in the Leo II dSph galaxy using the equivalent widths of the near infrared Ca II triplet lines. The metallicity scale used to convert the Ca II measurements is based on our calibration of Ca II to $[\text{Ca}/\text{H}]$ from Galactic cluster stars with ages from ≈ 2 to 14 Gyr and $-2.2 \lesssim [\text{Ca}/\text{H}] \lesssim +0.2$. Unlike the calibration of Ca II to $[\text{Fe}/\text{H}]$ developed by R97b, the Ca II to $[\text{Ca}/\text{H}]$ is independent of star-to-stars variations in $[\text{Ca}/\text{Fe}]$ with $[\text{Fe}/\text{H}]$. Defying the tradition of using “metallicity” interchangeably with iron abundances, $[\text{Ca}/\text{H}]$ was taken as the relevant metallicity in this investigation.

The Leo I dSph has a average metallicity of $[\text{Ca}/\text{H}] = -1.34 \pm 0.02$ ($\sigma = 0.21$) and an intrinsic spread in metallicity of 1.2 dex. The average metallicity of the Leo II dSph is more metal-poor with $[\text{Ca}/\text{H}] = -1.65 \pm 0.02$ ($\sigma = 0.17$) and has a 1.0 dex spread in metallicity.

The metallicity distribution function is different for the two dSphs. Leo I has an approximately Gaussian distribution with a slight excess at the metal-rich end, while Leo II has a steeper cut-off at the metal-rich end at $[\text{Ca}/\text{H}] \approx -1.4$. The differences in the shape of the distributions may be caused by greater mass loss in the less massive Leo II dSph, whose star formation ended approximately 7 Gyr ago, compared to the more massive Leo I dSph, whose star formation ended only ~ 1 to 2 Gyr ago. Significant differences, on the order of -0.5 dex, exist between the observed metallicity distribution functions and those derived by sophisticated modelling of Hess diagrams in CMDs obtained with HST. However, the assumption of a Galactic range of $[\text{Ca}/\text{Fe}]$ values show

our results to be consistent with the [Fe/H] values derived in other spectroscopic and photometric studies.

9 ACKNOWLEDGMENTS

We gratefully acknowledge financial support from the NSF through grant AST-0070895 to T. Smeecker-Hane. T. Bosler would like to thank the ARCS Foundation for a graduate student fellowship and Sigma Xi for a Grant in Aid of Research (2001) as well as Andy McWilliam, Virginia Trimble, Jay Gallagher and Linda Sparke for their inspiration and interest in this publication. We thank the staff at Keck Observatory, in particular, Paola Amico and Greg Wirth, for their excellent support, and we thank Bev Oke, Judy Cohen and their collaborators for an extremely useful spectrograph. In addition, we extend special thanks to the people of Hawai'ian ancestry on whose sacred mountain, Mauna Kea, we were privileged to be guests. Our research was expedited by the wide range of data made available at Canadian Astronomy Data Center (CADC), which is part of the Herzberg Institute of Astrophysics, a facility of the National Research Council of Canada. P. Stetson is extremely grateful to Howard E. Bond, Enrico V. Held, Giampaolo Piotto, Edward W. Olszewski, Ivo Saviane, Robert A. Schommer, and Nicholas B. Suntzeff, as well as to the CADC and the Isaac Newton Group Archives, for providing much of the CCD imagery used in this paper.

REFERENCES

- Alcaino, G., Liller, W., Alvarado, F., Wenderoth, E. 1990, AJ, 99, 1831
 Armandroff, T. E. & Zinn, R., 1988, AJ, 96, 92
 Barkana, R. & Loeb, A. ApJ, 523, 54
 Bosler, T.L., 2004 PhD Dissertation, University of California Irvine
 Carretta, E. & Gratton, R. G. 1997, A&AS, 121, 95
 Carney, B.W 1996, PASP, 108, 900
 Catelan, M. 2000, ApJ, 531, 826
 Cenarro, A.J., Gorgas, J., Cardiel, N., Vazdekis, A. & Peletier, R.F. 2002, MNRAS, 329, 863
 Cohen, J. G., Briley, M. M., and Stetson, P. B. 2002, AJ, 123, 2525
 Cudworth, K. M. 1979, AJ, 84, 1312
 Da Costa, G.S. & Armandroff, T.E. 1990, AJ, 100, 162
 D'Antona, F. 2001, in Extragalactic Star Clusters, IAU Symp. 207, eds. E. W. Grebel, D. Geisler & D. Minniti, (ASP: San Francisco), ASP Conf. Series (astro-ph/0105480)
 Díaz, A. I., Terlevich, E., Roberto, T., 1989, MNRAS, 239, 325
 Dean, J.F., Warren, P.R. & Cousins, A.W.J. 1978, 183, 569
 Dolphin, A. E. 2002, MNRAS, 332, 91
 Fulbright, J.P. 2000, AJ, 120, 184
 Fulbright, J.P. 2002, AJ, 123, 404
 Fullton, L.K. 1996, PASP, 108, 545
 Gallart, Carme, Freedman, W. L., Mateo, M., Chiosi, C., Thompson, I. B., Aparicio, A., Bertelli, G., Hodge, P. W., Lee, M. G., Olszewski, E. W., Saha, A., Stetson, P. B., Suntzeff, N. B. 1999a, ApJ, 514, 665
 Gallart, C., Freedman, W. L., Aparicio, A., Bertelli, G. & Chiosi, C. 1999b, ApJ, 118, 2245
 Grebel, E. K. 2000, in *Star Formation from the Small to the Large Scale*, Proc. 33rd ESLAB Symp., ESA SP-445, eds. F. Favata, A.A. Kaas, & Wilson (Noordwijk: ESA), 87 (astro-ph/0007001)
 Girardi, L., Bressan, A., Bertelli, G., & Chiosi, C. 2000, A&AS, 141, 371
 Harris, W. E. 1975, ApJ, 292, 397
 Held, E. V., Saviane, I., Momany, Y. & Carraro, G. 2000, ApJ, 530, L85
 Held, E. V., Clementini, G., Rizzi, L., Momany, Y., Saviane, I., Di Fabrizio, L. ApJ, 562, L39
 Hernandez, X., Gilmore, G., Valls-Gabaud, D. 2000, MNRAS, 317, 831
 Hurley-Keller, D., Mateo, M & Nemeč, J. 1998, AJ, 115, 1840
 Johnson, H. L., Sandage, A. R. 1956, ApJ, 124, 379
 Jorgensen, U.G., Carlsson, M. & Johnson, H. R. 1992, A&A, 254, 258
 Kraft, Robert P.; Ivans, Inese I., 2003, PASP, 115, 143
 Klypin, A. A., Kravtsov, A. V., Valenzuela, O. & Prada, F. 1999, ApJ, 522, 82
 Landolt, A.U. 1992, AJ, 104, 340
 Lee, M. G., Freedman, W., Mateo, M., Thompson, I., Roth, M., & Ruiz, M. 1993, AJ, 106, 1420
 Massey, P., Valdes, F., & Barnes, J. 1992, User's Guide to Reducing Slit Spectra with IRAF (Tucson: NOAO)
 Mateo, M. 1998, ARAA, 36, 435
 Mateo, M., Olszewski, E.W., Vogt, S.S. & Keane, M.J. 1998, AJ, 116, 2315
 McClure, R. D., Hesser, J. E., Stetson, P. B., Vandenberg, D. A. & Bell, R. A. 1987, AJ, 93, 1144
 McWilliam, A. 1997, ARA&A, 35, 503
 Mighell, K. J. & Rich, R. M. 1996, AJ, 111, 777
 Monet, D. G., et al. 1998, USNO-A2.0 Catalog (Flagstaff: USNO)
 Oke, J.B., Cohen, J.G., Carr, M., Cromer, J., Dungizian, A., Harris, F. H., Labrecque, S., Lucinio, R. & Schall, W. 1995, PASP, 107, 375
 Osterbrock, D.E. et al. 1996, PASP, 108, 277
 Osterbrock, D.E. & Fulbright, J.P. 1997, PASP, 109, 614
 Rutledge, G. A., Hesser, J. E., & Stetson, P. B., Mateo, M., Simard, L., Bolte, M., Friel, E. D., Copin, Y. 1997, PASP 109 883 (Rut97a)
 Rutledge, G. A., Hesser, J. E., & Stetson, P. B. 1997, PASP, 109, 907 (Rut97b)
 Sandquist, E. L., Bolte, M.; Stetson, P. B.; Hesser, J. E. 1996, ApJ, 470, 910
 Salaris, M., Chieffi, A., & Straniero, O. 1992, ApJ, 414, 580
 Schlegel, A. J., Finkbeiner, D. P., & Davies, M. 1998, ApJ, 500, 525
 Shetrone, M.D., Côte, P., & Sargent, W.L.W. 2001, ApJ, 548, 592
 Siegel, M.H. & Majewski, S.R. 2000, AJ, 120, 284
 Smeecker-Hane, T. A. & McWilliam, A. 1999, in *Spectro-Photometric Dating of Stars and Galaxies*, eds. I. Hubeny, S. Heap & R. Cornett, (ASP: San Francisco), ASP Conf. Series, vol. 192, 150
 Smeecker-Hane, T. A., Stetson, P. B., Hesser, J. E. & Vandenberg, D. A., 1996, in *From Stars to Galaxies: The Impact of Stellar Physics on Galaxy Evolution*, eds. C. Leitherer, U. Fritze-von Alvensleben and J. Huchra, (ASP: San Francisco), ASP Conf. Series, 98, 328 (astro-ph/9601020)
 Smeecker-Hane, T. A., Mandushev, G., Hesser, J. E., Stetson, P. B., Da Costa, G. S. & Hatzidimitriou, D. 1999, in *Spectro-Photometric Dating of Stars and Galaxies*, eds. I. Hubeny, S. Heap & R. Cornett, (ASP: San Francisco), ASP Conf. Series, vol. 192, 150 (astro-ph/9910211)
 Sneden, C., Kraft, R.P., Shetrone, M.D., Smith, G.H., Langer, G.E. & Prosser, C.F. 1997, AJ, 114, 1964
 Stetson, P.B. 2000, PASP, 112, 925
 Stetson, P.B. & Harris, W.E. 1977, AJ, 82, 854
 Stetson, P. B., Hesser, J. E., & Smeecker-Hane, T. A. 1998, PASP, 110, 533
 Thielemann, F.-K., Nomoto, K. & Yokoi, K. 1986, A&A, 158, 17
 Timmes, F.X., Woosley, S.E., & Weaver, T.A. 1995, ApJS, 98, 617
 Tonry, J. & Davis, M. 1979, AJ, 84, 1511
 Tolstoy, E. 1996, ApJ, 462, 684
 Tolstoy, E., Irwin, M. J., Cole, A. A., Pasquini, L., Gilmozzi, R., & Gallegar, J. S. 2001, MNRAS, 327, 918
 Vogt, S.S., Mateo, M.M., Olszewski, E.W. & Keane, M.J. 1995, AJ, 109, 151
 Wheeler, J.C., Sneden, C., & Truran, J.W. 1989, ARA&A, 27, 279
 Zinn, R. & West, M.J. 1984, ApJS, 55, 45

Table 1. Galaxy Properties

	Leo I	Leo II	
Right Ascension (J2000)	$\alpha = 10:08.5$	$\alpha = 11:13.5$	1
Declination (J2000)	$\delta = +12:18.5$	$\delta = +22:09.2$	1
Total Absolute Magnitude, M_V (mag)	-11.9	-9.6	1
Core and Tidal Radii (arcmin)	3.3, 12.6	2.9, 8.7	1
Distance (kpc)	273	204	2, 3
Distance Modulus, $(m - M)_0$ (mag)	22.18	21.55	2, 3
Horizontal Branch Magnitude, V_{HB} (mag)	22.70	22.17	4, 5
Foreground Reddening, $E(B-V)$ (mag)	0.040	0.027	6, 3

(1) Mateo 1998; (2) Lee, et al. 1993; (3) Mighell & Rich 1998; (4) Held, et al. 2001; (5) Siegel & Majewski 2000; (6) Schlegel, Finkbeiner & Davis 1998.

Table 2. Galactic Globular Cluster Stars

Cluster-Star ID	$V - V_{HB}$ (mag)	$\sum W$ (\AA)	$\sigma_{\sum W}$ (\AA)	$\sum W_{\text{Rut97a}}$ (\AA)	$\sigma_{\sum W_{\text{Rut97a}}}$ (\AA)	Ref.
NGC 1904 - 52	-2.09	3.84	0.12	4.15	0.15	1, 2
NGC 1904 - 131	-2.54	4.27	0.17	4.71	0.14	1, 2
NGC 1904 - 223	-2.96	4.25	0.15	4.80	0.16	1, 2
NGC 1904 - 160	-3.13	4.13	0.15	—	—	1, 2
NGC 1904 - 181	-2.20	3.72	0.11	—	—	1, 2
NGC 1904 - 89	-1.44	3.61	0.10	—	—	1, 2
NGC 1904 - 241	-2.54	4.36	0.16	—	—	1, 2
NGC 1904 - 294	-1.93	3.97	0.14	—	—	1, 2
NGC 4590 - AL81	-1.89	2.90	0.16	2.64	0.07	3, 5
NGC 4590 - HI239	-1.42	2.31	0.07	2.62	0.07	4, 5
NGC 4590 - HI119	-2.04	2.44	0.05	2.76	0.06	4, 5
NGC 4590 - HQ ^a	-2.11	2.56	0.07	3.00	0.04	4, 5
NGC 4590 - HII47	-0.55	2.18	0.13	2.36	0.10	4, 5
NGC 4590 - HII28	-1.97	2.90	0.05	2.99	0.06	4, 5
NGC 4590 - HI30	-1.53	2.50	0.10	2.70	0.07	4, 5
NGC 4590 - HI35	-1.13	2.33	0.11	2.24	0.10	4, 5
NGC 4590 - 38	-1.11	2.12	0.05	—	—	5, 6
NGC 4590 - 31	-1.32	2.23	0.06	—	—	5, 6
NGC 4590 - 36	-1.10	2.13	0.04	—	—	5, 6
NGC 4590 - 22 ^a	-1.59	4.58	0.13	—	—	5, 6
NGC 4590 - HI82	-2.99	3.26	0.08	—	—	4, 5
NGC 4590 - 23	-1.48	2.14	0.05	—	—	5, 6
NGC 4590 - A53	-2.78	2.98	0.08	—	—	3, 5
NGC 4590 - HI49	-1.08	1.84	0.11	—	—	4, 5
NGC 5272 - 265	-2.39	4.541	0.137	4.47	0.12	7, 8
NGC 5272 - 334	-2.41	4.487	0.127	4.73	0.16	7, 8
NGC 5272 - 640	-2.38	4.488	0.126	4.28	0.07	7, 8
NGC 5272 - 885	-2.18	4.073	0.118	4.31	0.11	7, 8
NGC 5272 - 1217	-1.65	4.115	0.091	—	—	7, 8
NGC 5272 - 589	-2.78	4.624	0.129	—	—	7, 8
NGC 5272 - 250	-1.54	3.965	0.111	—	—	7, 8
NGC 5272 - 238	-3.03	4.679	0.099	—	—	7, 8
NGC 5272 - 345 ^a	-2.19	4.513	0.124	—	—	7, 8
NGC 6171 - SL	-1.66	5.00	0.16	4.75	0.11	5, 6
NGC 6171 - SR	-1.04	4.25	0.14	4.27	0.14	5, 6
NGC 6171 - S62	-1.73	4.81	0.14	5.13	0.07	5, 6
NGC 6171 - SF	-2.31	5.08	0.13	5.45	0.09	5, 6
NGC 6171 - SS	-0.91	4.72	0.16	4.88	0.15	5, 6
NGC 6171 - SU	-0.92	4.04	0.10	4.44	0.22	5, 6
NGC 6171 - SH	-1.86	5.01	0.14	5.16	0.09	5, 6
NGC 6171 - S203	-0.48	4.08	0.14	4.61	0.19	5, 6

NOTES: a: A non-member based upon its radial velocity

References:

- (1) ID: Stetson & Harris 1977
- (2) Photometry: Stetson & Harris 1977
- (3) ID: Alcaino & Liller 1990
- (4) ID: Harris 1975
- (5) Photometry: Stetson, P.B., private comm.
- (6) ID: Stetson, P.B., private comm.
- (7) ID: Johnson & Sadage 1956
- (8) Photometry: Cudworth 1979

Table 3. The Calibrating Globular Clusters

Cluster	V_{HB} (mag)	[Fe/H]	W'_{Rut} (Å)	$\sigma_{W'_{\text{Rut}}}$ (Å)	W' (Å)	$\sigma_{W'}$ (Å)	N
NGC 1904 = M79	16.15	-1.52	3.09	0.12	2.51	0.05	8
NGC 4590 = M68	15.68	-2.30	1.59	0.08	1.32	0.03	9
NGC 5272 = M3	15.65	-1.55	3.07	0.08	2.91	0.05	8
NGC 6171 = M107	15.70	-0.95	3.99	0.08	3.71	0.05	8

Table 4. Regressions for W' to Fe II Results

Line Style	$[\text{Fe}/\text{H}] = A + B * W' + C * W'^2$								
	A (dex)	σ_A	B (dex/Å)	σ_B	C (dex/Å) ²	σ_C	m.e.1	rms	χ^2_ν
Dashed	-2.985	0.256	+0.329	0.145	+0.029	0.019	1.27	0.14	0.04
Dot-dash	-3.340	0.055	+0.549	0.015	1.40	0.18	4.52
Solid	-3.078	0.058	+0.440	0.020	1.25	0.10	0.31
KI03 ^a	-3.225	0.082	+0.537	0.024

Dot-dash=linear fit, Dashed=quadratic fit, Solid=linear fit to GGCs only
^a: Indicates the fit from KI03 based on Fe II abundances

Table 5. Abundances and Reduced Equivalent Widths for Clusters used in the Ca II \rightarrow [Ca/H] Calibration from Bosler, 2004

Group #	NGC #	Alt. ID	W' (Å)	$\sigma_{W'}$ (Å)	# of Stars	[Fe/H]	$\sigma_{[\text{Fe}/\text{H}]}$	[Ca/H]	$\sigma_{[\text{Ca}/\text{H}]}$	# of Stars
1	104	47 Tuc	4.53 ^b	0.07	31	-0.64	0.04	-0.50	0.04	12
	288		3.86	0.08	10	-1.53	0.06	-1.11	0.13	2
	1904	M79	3.14 ^b	0.14	9	-1.52	0.04	-1.24	0.07	6
	4590	M68	1.59 ^b	0.08	19	-2.30	0.04	-2.01	0.05	7
	5272	M3	3.10	0.07	9	-1.58	0.04	-1.31	0.06	6
	5904	M5	3.73 ^b	0.12	43	-1.38	0.06	-0.99	0.09	4
	6341	M92	1.77	0.08	6	-2.43	0.04	-2.04	0.06	7
	6638		4.31 ^b	0.12	12	-1.26	0.05	-0.98	0.08	4
	7089	M2	3.26	0.07	11	-1.72	0.08	-1.36	0.10	4
	7099	M30	1.89	0.09	5	-2.22	0.04	-1.83	0.06	5
2 ^a	6121	M4	3.87 ^b	0.07	33	-1.37	0.11	-1.11	0.11	24
	6254	M10	3.42 ^b	0.09	16	-1.67	0.11	-1.38	0.09	9
	6397		2.17 ^b	0.08	19	-2.11	0.11	-1.91	0.11	6
	6752		3.41 ^b	0.07	14	-1.72	0.12	-1.46	0.11	8
	6838	M71	4.64 ^b	0.17	11	-1.09	0.11	-0.66	0.09	10
	7078	M15	1.56 ^b	0.12	6	-2.45	0.11	-2.16	0.09	7
3	2141		5.41	0.09	10	-0.46	0.11	-0.42	0.11	5
	2420		5.21	0.10	6	-0.33	0.13	-0.41	0.14	3
	2682	M67	5.62	0.10	8	+0.03	0.10	-0.08	0.09	6
	6791		6.50	0.11	8	+0.07	0.29	+0.02	0.24	2
	7789		5.32	0.10	8	-0.37	0.11	-0.41	0.12	3

^a: The [Ca/H] values for Group 2 clusters have been derived using the [Ca/Fe] value found in the literature: Ivans et al. (1999) for M4, Kraft et al. (1995) for M10, Castillo et al. (2000) for N6397, Cavallo et al. (2004) for N6752, Ramirez et al. (2002) for M71 and Sneden et al. (1997) for M15. Since these values have not been transformed to the scale of this work, the calcium values are listed here but were not used in the final [Ca/H] calibration of the Ca II triplet.

^b: W' and $\sigma_{W'}$ come from R97a.

Table 6: Parameters for Stars in the Leo I dSph

ID	V (mag)	B-V (mag)	RA (J2000)	DEC (J2000)	SNR	v_{helio} (km/sec)
2195	19.78	1.45	10:7:59.14	12:17:17.6	18	303.0
2405	20.40	1.14	10:8:01.21	12:16:14.7	11	280.9
2488	19.92	1.33	10:8:01.89	12:17:55.6	26	287.1
2557	20.13	1.32	10:8:02.49	12:16:19.8	14	278.8
2655	20.30	1.39	10:8:03.24	12:19:11.0	17	282.7
2767	20.22	1.22	10:8:04.00	12:19:41.6	16	297.6
2907	20.20	1.20	10:8:04.91	12:17:53.3	17	279.1
3135	20.20	1.12	10:8:06.28	12:17:45.1	19	270.6
3499	20.15	1.33	10:8:08.02	12:19:24.3	16	281.9
3994	19.88	1.31	10:8:09.96	12:16:25.4	17	287.9
4173	20.08	1.12	10:8:10.59	12:17:07.9	19	257.6
4690	20.16	1.36	10:8:12.12	12:17:12.4	15	270.3
5496	19.89	1.01	10:8:14.19	12:17:36.1	18	302.9
6065	19.81	1.47	10:8:15.41	12:19:01.4	34	279.2
6119	20.16	1.29	10:8:15.52	12:16:41.8	16	300.0
6372	20.30	1.09	10:8:16.08	12:19:22.7	23	265.6
6581	20.25	1.10	10:8:16.48	12:15:51.4	15	296.1
6849	19.88	0.95	10:8:16.97	12:18:28.3	26	293.0
7239	20.21	1.13	10:8:17.61	12:16:30.4	22	266.4
7548	19.92	1.23	10:8:18.14	12:17:46.2	25	270.3
7752	20.23	1.01	10:8:18.47	12:19:51.1	12	241.5
7975	20.26	1.13	10:8:18.82	12:19:50.9	26	269.9
7984	20.15	1.18	10:8:18.83	12:19:04.5	13	274.1
8203	19.91	1.32	10:8:19.16	12:20:48.7	21	281.9
8391	20.26	1.01	10:8:19.44	12:16:34.2	13	282.1
8409	20.11	1.21	10:8:19.47	12:19:09.7	14	273.8
8608	19.76	1.27	10:8:19.75	12:16:55.0	33	298.8
8635	20.32	1.08	10:8:19.79	12:16:34.2	13	282.1
8885	19.65	1.13	10:8:20.13	12:17:02.8	27	288.0
8893	20.18	0.94	10:8:20.15	12:17:47.0	16	286.1
8937	19.78	1.08	10:8:20.21	12:17:56.0	14	266.8
9099	20.33	1.07	10:8:20.45	12:16:01.7	21	283.4
9187	20.24	0.98	10:8:20.55	12:15:47.2	14	263.7
9241	20.33	1.19	10:8:20.63	12:19:21.0	14	276.6
9683	19.93	1.36	10:8:21.23	12:17:41.3	15	283.5
9764	19.83	1.35	10:8:21.34	12:19:52.6	12	284.3
9782	19.56	1.17	10:8:21.36	12:16:22.8	23	279.7
9915	19.68	1.33	10:8:21.55	12:19:12.9	35	283.0
10190	20.09	1.30	10:8:21.87	12:19:33.2	17	271.2
10439	20.01	1.21	10:8:22.22	12:21:39.5	18	279.1
10670	20.12	1.21	10:8:22.50	12:22:40.1	26	275.6
10789	19.91	1.28	10:8:22.65	12:17:21.5	18	252.8
10914	19.80	1.19	10:8:22.80	12:17:59.9	29	290.3
11712	20.43	1.10	10:8:23.77	12:15:43.9	18	295.0
11758	19.63	1.20	10:8:23.83	12:17:10.7	36	273.6
11808	19.69	1.28	10:8:23.89	12:17:37.3	23	290.0
12171	20.33	0.89	10:8:24.35	12:18:27.4	11	296.4
12351	19.78	1.21	10:8:24.54	12:17:42.1	22	288.2
12515	19.87	1.40	10:8:24.71	12:17:24.2	28	276.0
12581	20.24	1.17	10:8:24.81	12:15:54.6	19	269.1
13094	20.02	1.37	10:8:25.39	12:16:53.3	18	284.1
13137	20.01	1.29	10:8:25.43	12:17:16.6	26	245.9
13158	19.88	1.24	10:8:25.46	12:16:36.3	25	288.6
13415	20.13	1.48	10:8:25.74	12:21:01.9	13	285.2
14095	19.81	1.34	10:8:26.49	12:19:11.2	34	279.6
14307	20.53	1.19	10:8:26.71	12:16:36.4	16	275.7

continued on next page

Table 6: Leo I *continued*

ID	V (mag)	B-V (mag)	RA (J2000)	DEC (J2000)	SNR	v_{helio} (km/sec)
14738	19.92	0.84	10:8:27.16	12:17:56.8	14	284.6
14927	19.73	1.25	10:8:27.36	12:16:17.6	23	282.6
16048	19.79	1.13	10:8:28.56	12:19:08.0	14	295.2
16088	20.12	1.20	10:8:28.59	12:16:20.6	25	280.8
16219	19.64	1.19	10:8:28.76	12:17:55.1	25	284.0
16248	20.33	1.05	10:8:28.79	12:20:33.6	16	272.8
16334	19.90	1.21	10:8:28.89	12:19:27.8	18	291.6
16635	19.78	1.25	10:8:29.20	12:16:12.2	33	283.3
17009	19.82	1.36	10:8:29.60	12:18:07.5	32	289.7
17226	20.32	1.13	10:8:29.86	12:19:14.6	22	298.1
17437	20.12	0.96	10:8:30.08	12:18:12.6	15	265.3
17620	20.40	0.98	10:8:30.29	12:17:13.5	12	300.6
17854	19.74	1.11	10:8:30.56	12:16:27.5	34	293.8
18030	19.56	1.12	10:8:30.76	12:17:29.8	26	285.6
18214	19.77	1.35	10:8:30.97	12:16:40.6	27	286.4
18315	19.69	1.28	10:8:31.09	12:18:35.8	30	270.8
18323	20.08	0.94	10:8:31.09	12:18:02.6	21	298.4
18509	20.03	1.19	10:8:31.31	12:20:21.9	19	297.2
18588	19.87	1.46	10:8:31.40	12:15:55.8	26	288.6
18676	20.44	1.14	10:8:31.50	12:21:49.1	13	274.4
18765	20.03	1.34	10:8:31.58	12:17:26.4	24	287.0
18801	19.74	1.29	10:8:31.62	12:18:50.3	18	287.5
18812	20.13	1.13	10:8:31.64	12:16:52.4	16	293.0
18880	20.05	1.16	10:8:31.71	12:18:38.6	11	271.7
19040	20.08	1.20	10:8:31.88	12:22:30.9	14	291.4
19080	19.71	1.18	10:8:31.93	12:18:41.9	31	275.1
19262	20.11	1.22	10:8:32.14	12:18:38.5	11	293.9
19667	19.73	1.22	10:8:32.62	12:18:09.0	31	265.8
19881	20.02	1.15	10:8:32.87	12:17:35.2	27	290.1
20470	19.75	1.18	10:8:33.57	12:18:25.7	28	279.5
20882	19.96	1.33	10:8:34.06	12:23:16.7	15	275.8
21026	20.06	1.23	10:8:34.24	12:16:11.4	16	292.1
21192	20.28	1.19	10:8:34.45	12:21:23.0	14	286.8
21196	20.54	1.13	10:8:34.46	12:20:06.5	11	302.1
21325	19.70	1.33	10:8:34.64	12:18:56.2	26	297.3
21348	20.29	1.11	10:8:34.67	12:17:16.7	33	270.4
22001	20.35	1.20	10:8:35.55	12:16:59.1	23	279.1
22513	20.07	1.30	10:8:36.25	12:19:12.1	26	298.3
22788	19.73	1.34	10:8:36.65	12:17:50.6	11	271.5
23074	20.08	1.25	10:8:37.06	12:16:56.3	23	282.2
23518	20.35	0.99	10:8:37.68	12:19:49.6	18	267.9
24095	20.26	0.99	10:8:38.65	12:18:51.8	17	263.8
25113	19.70	1.38	10:8:40.45	12:16:37.9	26	287.1
25440	20.38	0.90	10:8:41.10	12:17:36.5	17	292.1
25820	20.20	1.23	10:8:41.92	12:18:39.5	21	251.9

Table 7: Parameters for Stars in the Leo II dSph

ID	V (mag)	B-V (mag)	RA (J2000)	DEC (J2000)	SNR	v_{helio} (km/sec)
156	18.58	1.79	11:13:20.9	22:08:22.9	19	103.2
166	18.87	1.17	11:13:38.9	22:10:18.2	38	92.7
180	19.08	1.47	11:13:23.2	22:10:55.9	42	84.7
195	19.08	1.08	11:13:33.2	22:08:12.5	36	88.2
209	19.16	1.42	11:13:31.1	22:06:30.4	42	98.6
230	19.23	1.41	11:13:34.8	22:09:42.4	27	108.0
233	19.22	1.34	11:13:24.5	22:06:13.5	18	75.6
234	19.26	1.21	11:13:20.8	22:08:34.4	21	75.1
235	19.24	1.44	11:13:23.4	22:08:54.3	22	94.6
236	19.21	1.37	11:13:40.5	22:12:18.4	37	101.1
237	19.26	1.04	11:13:39.8	22:10:23.1	30	100.0
248	19.31	1.20	11:13:27.7	22:10:13.0	29	98.7
249	19.32	1.16	11:13:19.3	22:07:41.6	22	106.8
254	19.35	1.34	11:13:32.1	22:07:29.8	34	84.8
255	19.30	1.35	11:13:34.5	22:11:42.5	38	86.7
256	19.34	1.23	11:13:27.7	22:10:39.7	30	99.7
258	19.35	1.35	11:13:19.8	22:09:20.3	37	91.1
259	19.35	1.37	11:13:30.8	22:10:51.0	18	100.2
260	19.32	1.29	11:13:26.6	22:07:26.3	33	113.4
271	19.37	1.37	11:13:19.9	22:09:45.9	40	74.2
277	19.39	1.26	11:13:37.8	22:09:27.2	22	85.2
280	19.45	1.12	11:13:23.8	22:05:32.8	28	90.7
281	19.42	1.09	11:13:32.7	22:07:04.7	35	82.1
282	19.38	1.48	11:13:39.5	22:09:16.8	34	95.3
285	19.43	1.31	11:13:33.9	22:06:08.2	34	79.3
293	19.37	1.29	11:13:25.7	22:06:37.8	37	60.4
296	19.46	1.05	11:13:21.4	22:10:37.7	35	64.6
302	19.46	1.17	11:13:30.9	22:08:11.5	30	117.2
304	19.47	1.25	11:13:30.3	22:06:57.6	35	82.9
320	19.47	1.30	11:13:29.7	22:06:46.5	18	87.3
331	19.56	1.12	11:13:37.1	22:09:33.2	33	101.7
333	19.56	1.20	11:13:26.5	22:11:07.4	33	76.4
336	19.56	1.18	11:13:23.3	22:10:05.2	37	91.0
341	19.59	1.24	11:13:29.6	22:08:57.7	32	87.4
351	19.59	1.25	11:13:31.0	22:11:21.9	39	79.1
352	19.55	1.36	11:13:23.1	22:10:22.6	17	92.4
370	19.64	0.93	11:13:33.3	22:09:44.3	21	88.2
377	19.65	1.19	11:13:29.6	22:07:16.1	27	84.3
379	19.67	1.29	11:13:31.2	22:08:24.6	33	72.5
392	19.70	1.13	11:13:28.8	22:08:47.0	12	106.0
395	19.73	1.14	11:13:33.1	22:07:37.6	23	91.7
396	19.71	0.95	11:13:27.9	22:08:15.4	18	85.2
397	19.73	1.17	11:13:34.5	22:08:09.8	19	80.6
402	19.74	1.19	11:13:31.0	22:08:44.6	24	86.5
409	19.74	1.06	11:13:27.9	22:08:29.5	11	78.5
420	19.82	1.11	11:13:30.9	22:09:32.6	28	79.7
422	19.79	1.10	11:13:16.6	22:08:58.9	21	80.0
429	19.73	1.22	11:13:25.6	22:07:44.1	19	79.4
430	19.79	1.18	11:13:28.5	22:08:43.2	19	79.9
432	19.83	0.97	11:13:15.5	22:09:00.9	14	82.4
434	19.81	1.14	11:13:31.7	22:07:46.8	21	67.0
435	19.78	1.20	11:13:36.0	22:12:20.8	21	99.5
441	19.83	1.01	11:13:31.6	22:08:34.2	20	88.4
471	19.88	0.95	11:13:38.5	22:09:47.3	12	90.4
493	19.96	1.04	11:13:35.9	22:09:27.7	16	99.5
495	19.95	1.14	11:13:32.5	22:11:22.8	22	92.7

continued on next page

Table 7: Leo II *continued*

ID	V (mag)	B-V (mag)	RA (J2000)	DEC (J2000)	SNR	v_{helio} (km/sec)
508	19.97	1.11	11:13:23.7	22:07:07.2	22	86.9
524	20.04	1.18	11:13:35.1	22:11:34.7	17	95.6
526	20.06	1.12	11:13:36.2	22:10:18.6	16	86.9
533	20.06	1.03	11:13:26.8	22:08:24.8	15	70.7
541	20.10	1.08	11:13:23.7	22:09:12.6	15	60.7
549	20.13	1.07	11:13:18.2	22:08:29.3	15	88.5
552	20.15	1.01	11:13:32.8	22:10:53.3	22	103.5
556	20.14	1.00	11:13:38.0	22:11:17.4	13	105.4
558	20.20	0.95	11:13:23.3	22:05:23.3	24	57.9
569	20.15	1.06	11:13:23.4	22:06:18.1	22	85.3
570	20.17	1.09	11:13:34.7	22:11:01.9	12	111.8
573	20.18	1.16	11:13:36.2	22:08:51.2	24	92.6
576	20.20	1.04	11:13:30.5	22:08:24.9	16	86.0
584	20.20	1.04	11:13:32.3	22:06:55.9	17	78.6
588	20.22	1.00	11:13:33.8	22:10:03.3	15	83.6
604	20.24	1.05	11:13:37.9	22:08:13.3	14	74.2
614	20.30	0.99	11:13:34.5	22:11:05.5	18	86.9
623	20.26	1.22	11:13:26.1	22:06:48.2	17	83.0

Table 8: Spectroscopic Data for Stars in the Leo I dSph

ID	W'_{α} (Å)	$\sigma_{W'}$ (Å)	[Fe/H] CG97	$\sigma_{[\text{Fe}/\text{H}]}$ Total	$\sigma_{[\text{Fe}/\text{H}]}$ Random	[Ca/H]	$\sigma_{[\text{Ca}/\text{H}]}$ Total	$\sigma_{[\text{Ca}/\text{H}]}$ Random
2195	3.76	0.20	-1.08	0.16	0.08	-1.01	0.15	0.09
2405	3.17	0.30	-1.33	0.21	0.11	-1.29	0.22	0.14
2488	2.92	0.19	-1.43	0.15	0.06	-1.41	0.15	0.09
2557	2.90	0.23	-1.44	0.17	0.08	-1.42	0.17	0.11
2655	1.99	0.21	-1.82	0.16	0.07	-1.84	0.16	0.10
2767	2.50	0.24	-1.61	0.18	0.09	-1.60	0.18	0.11
2907	2.84	0.22	-1.47	0.17	0.08	-1.44	0.16	0.10
3135	3.03	0.24	-1.39	0.18	0.09	-1.35	0.18	0.11
3499	3.79	0.23	-1.07	0.17	0.09	-1.00	0.17	0.11
3994	2.59	0.19	-1.57	0.15	0.06	-1.56	0.15	0.09
4173	2.77	0.21	-1.50	0.16	0.07	-1.48	0.16	0.10
4690	3.81	0.26	-1.06	0.19	0.10	-0.99	0.19	0.12
5496	2.50	0.22	-1.61	0.17	0.08	-1.60	0.16	0.10
6065	3.50	0.19	-1.19	0.15	0.07	-1.13	0.15	0.09
6119	2.56	0.22	-1.58	0.17	0.08	-1.57	0.16	0.10
6372	1.86	0.20	-1.88	0.15	0.06	-1.90	0.15	0.09
6581	3.66	0.36	-1.12	0.25	0.15	-1.06	0.26	0.17
6849	2.34	0.23	-1.68	0.17	0.08	-1.68	0.17	0.11
7239	2.58	0.19	-1.57	0.15	0.06	-1.57	0.15	0.09
7548	4.04	0.23	-0.96	0.17	0.09	-0.88	0.17	0.11
7752	1.77	0.28	-1.92	0.20	0.10	-1.95	0.20	0.13
7975	3.64	0.21	-1.13	0.16	0.08	-1.07	0.16	0.10
7984	3.85	0.20	-1.04	0.16	0.07	-0.97	0.15	0.09
8203	3.72	0.20	-1.10	0.16	0.07	-1.03	0.15	0.09
8391	2.92	0.35	-1.41	0.15	0.12	-1.41	0.25	0.16
8409	3.09	0.24	-1.36	0.18	0.09	-1.33	0.18	0.11
8608	2.83	0.24	-1.47	0.18	0.09	-1.45	0.18	0.11
8635	3.13	0.23	-1.13	0.22	0.11	-1.31	0.17	0.11
8885	2.22	0.21	-1.73	0.16	0.07	-1.73	0.16	0.10
8893	3.58	0.26	-1.16	0.19	0.10	-1.10	0.19	0.12
8937	4.21	0.28	-0.89	0.20	0.11	-0.80	0.20	0.13
9099	3.40	0.20	-1.23	0.16	0.07	-1.18	0.15	0.09
9187	3.28	0.28	-1.28	0.20	0.11	-1.24	0.20	0.13
9241	2.84	0.24	-1.47	0.18	0.09	-1.44	0.18	0.11
9683	3.01	0.22	-1.40	0.17	0.08	-1.36	0.17	0.10
9764	2.40	0.29	-1.65	0.21	0.11	-1.65	0.21	0.14
9782	2.25	0.18	-1.71	0.15	0.05	-1.72	0.14	0.08
9915	3.95	0.21	-1.00	0.16	0.08	-0.92	0.16	0.10
10190	2.70	0.21	-1.53	0.16	0.07	-1.51	0.16	0.10
10439	3.27	0.19	-1.28	0.15	0.07	-1.24	0.15	0.09
10670	3.40	0.23	-1.23	0.17	0.08	-1.18	0.17	0.11
10789	3.36	0.22	-1.25	0.17	0.08	-1.20	0.17	0.10
10914	3.09	0.21	-1.36	0.16	0.07	-1.33	0.16	0.10
11712	2.25	0.26	-1.72	0.19	0.09	-1.72	0.19	0.12
11758	2.70	0.19	-1.53	0.15	0.06	-1.51	0.15	0.09
11808	3.45	0.20	-1.21	0.16	0.07	-1.16	0.15	0.09
12171	3.24	0.30	-1.30	0.21	0.12	-1.26	0.22	0.14
12351	3.00	0.22	-1.40	0.17	0.08	-1.37	0.17	0.10
12515	2.80	0.24	-1.49	0.18	0.09	-1.46	0.18	0.11
12581	3.02	0.20	-1.39	0.16	0.07	-1.36	0.15	0.09
13094	2.87	0.21	-1.45	0.16	0.07	-1.43	0.16	0.10
13137	3.21	0.22	-1.31	0.17	0.08	-1.27	0.17	0.10
13158	3.78	0.21	-1.07	0.16	0.08	-1.00	0.16	0.10
13415	3.04	0.21	-1.38	0.16	0.07	-1.35	0.16	0.10
14095	3.19	0.17	-1.32	0.14	0.06	-1.28	0.13	0.08
14307	4.63	0.26	-0.72	0.19	0.11	-0.60	0.19	0.12

continued on next page

Table 8: Leo I *continued*

ID	W' ^a (Å)	$\sigma_{W'}$ (Å)	[Fe/H] CG97	$\sigma_{[\text{Fe}/\text{H}]}$ Total	$\sigma_{[\text{Fe}/\text{H}]}$ Random	[Ca/H]	$\sigma_{[\text{Ca}/\text{H}]}$ Total	$\sigma_{[\text{Ca}/\text{H}]}$ Random
14738	3.16	0.24	-1.33	0.18	0.09	-1.29	0.18	0.11
14927	3.25	0.20	-1.29	0.16	0.07	-1.25	0.15	0.09
16048	2.35	0.24	-1.67	0.18	0.08	-1.67	0.18	0.11
16088	2.97	0.21	-1.41	0.16	0.07	-1.38	0.16	0.10
16219	3.11	0.21	-1.35	0.16	0.07	-1.32	0.16	0.10
16248	4.42	0.29	-0.80	0.21	0.12	-0.70	0.21	0.14
16334	3.42	0.23	-1.22	0.17	0.08	-1.17	0.17	0.11
16635	3.14	0.21	-1.34	0.16	0.07	-1.30	0.16	0.10
17009	2.78	0.21	-1.49	0.16	0.07	-1.47	0.16	0.10
17226	4.00	0.23	-0.98	0.17	0.09	-0.90	0.17	0.11
17437	2.94	0.26	-1.43	0.19	0.10	-1.40	0.19	0.12
17620	3.53	0.26	-1.18	0.19	0.10	-1.12	0.19	0.12
17854	0.83	0.19	-2.31	0.15	0.05	-2.39	0.14	0.09
18030	3.89	0.19	-1.03	0.15	0.07	-0.95	0.15	0.09
18214	2.10	0.20	-1.78	0.16	0.06	-1.79	0.15	0.09
18315	2.93	0.17	-1.43	0.14	0.05	-1.40	0.13	0.08
18323	3.04	0.22	-1.38	0.17	0.08	-1.35	0.17	0.10
18509	3.88	0.21	-1.03	0.16	0.08	-0.95	0.16	0.10
18588	3.45	0.20	-1.21	0.16	0.07	-1.16	0.15	0.09
18676	3.65	0.27	-1.13	0.19	0.10	-1.06	0.20	0.13
18765	3.52	0.20	-1.18	0.16	0.07	-1.12	0.15	0.09
18801	3.22	0.22	-1.31	0.17	0.08	-1.26	0.17	0.10
18812	2.32	0.23	-1.68	0.17	0.08	-1.69	0.17	0.11
18880	3.21	0.37	-1.31	0.26	0.15	-1.27	0.26	0.17
19040	3.14	0.26	-1.34	0.19	0.10	-1.30	0.19	0.12
19080	2.09	0.18	-1.78	0.15	0.05	-1.80	0.14	0.08
19262	3.76	0.23	-1.08	0.18	0.09	-1.01	0.17	0.11
19667	1.90	0.17	-1.86	0.14	0.04	-1.89	0.13	0.08
19881	3.41	0.22	-1.23	0.17	0.08	-1.18	0.17	0.10
20470	3.50	0.22	-1.19	0.17	0.08	-1.13	0.17	0.10
20882	3.08	0.26	-1.36	0.19	0.10	-1.33	0.19	0.12
21026	2.78	0.21	-1.49	0.16	0.07	-1.47	0.16	0.10
21192	2.73	0.22	-1.52	0.17	0.08	-1.49	0.16	0.10
21196	2.63	0.28	-1.56	0.20	0.11	-1.54	0.20	0.13
21325	3.15	0.20	-1.34	0.16	0.07	-1.30	0.15	0.09
21348	3.91	0.17	-1.02	0.14	0.06	-0.94	0.14	0.08
22001	3.56	0.19	-1.16	0.15	0.07	-1.10	0.15	0.09
22513	3.00	0.19	-1.40	0.15	0.06	-1.37	0.15	0.09
22788	4.11	0.32	-0.93	0.23	0.13	-0.85	0.23	0.15
23074	3.05	0.17	-1.38	0.14	0.05	-1.34	0.13	0.08
23518	3.40	0.20	-1.23	0.16	0.07	-1.18	0.15	0.09
24095	3.09	0.20	-1.36	0.16	0.07	-1.33	0.15	0.09
25113	3.56	0.19	-1.17	0.15	0.07	-1.10	0.15	0.09
25440	1.55	0.25	-2.01	0.18	0.09	-2.05	0.18	0.12
25820	3.40	0.20	-1.23	0.16	0.07	-1.18	0.15	0.09

^a The W' values listed here have been scaled to the work of R97a.

Table 9: Spectroscopic Data for Stars in the Leo II dSph

ID	W' (Å)	$\sigma_{W'}$ (Å)	[Fe/H] CG97	$\sigma_{[\text{Fe}/\text{H}]}$ Total	$\sigma_{[\text{Fe}/\text{H}]}$ Random	[Ca/H]	$\sigma_{[\text{Ca}/\text{H}]}$ Total	$\sigma_{[\text{Ca}/\text{H}]}$ Random
156	2.87	0.19	-1.45	0.15	0.06	-1.45	0.15	0.09
166	2.71	0.18	-1.52	0.15	0.06	-1.53	0.14	0.08
180	2.52	0.19	-1.60	0.15	0.06	-1.61	0.15	0.09
195	2.53	0.19	-1.60	0.15	0.06	-1.61	0.15	0.09
209	2.54	0.18	-1.59	0.15	0.06	-1.60	0.14	0.08
230	2.61	0.21	-1.56	0.16	0.07	-1.57	0.16	0.10
233	2.49	0.19	-1.62	0.15	0.06	-1.63	0.15	0.09
234	2.05	0.19	-1.80	0.15	0.05	-1.83	0.15	0.09
235	3.26	0.25	-1.29	0.18	0.09	-1.28	0.18	0.11
236	1.81	0.19	-1.90	0.15	0.05	-1.94	0.15	0.09
237	0.36	0.22	-2.51	0.16	0.06	-2.59	0.16	0.10
248	2.74	0.18	-1.51	0.14	0.05	-1.51	0.14	0.08
249	0.77	0.25	-2.34	0.18	0.08	-2.41	0.18	0.11
254	2.94	0.19	-1.43	0.15	0.06	-1.42	0.15	0.09
255	2.38	0.18	-1.66	0.14	0.05	-1.68	0.14	0.08
256	2.68	0.20	-1.54	0.16	0.07	-1.54	0.15	0.09
258	2.59	0.18	-1.57	0.15	0.06	-1.58	0.14	0.08
259	3.54	0.29	-1.17	0.21	0.11	-1.15	0.21	0.13
260	2.60	0.18	-1.57	0.14	0.05	-1.58	0.14	0.08
271	2.82	0.18	-1.48	0.15	0.06	-1.48	0.14	0.08
277	2.20	0.23	-1.74	0.17	0.08	-1.76	0.17	0.10
280	2.76	0.19	-1.50	0.15	0.06	-1.50	0.15	0.09
281	1.46	0.20	-2.05	0.15	0.06	-2.09	0.15	0.09
282	2.72	0.18	-1.52	0.15	0.06	-1.52	0.14	0.08
285	2.76	0.19	-1.50	0.15	0.06	-1.50	0.15	0.09
293	1.95	0.18	-1.84	0.14	0.05	-1.87	0.14	0.08
296	1.53	0.19	-2.02	0.15	0.05	-2.06	0.15	0.09
302	1.97	0.19	-1.83	0.15	0.05	-1.86	0.15	0.09
304	2.01	0.17	-1.81	0.14	0.04	-1.84	0.14	0.08
320	2.96	0.18	-1.42	0.15	0.06	-1.41	0.14	0.08
331	0.90	0.19	-2.28	0.15	0.04	-2.35	0.15	0.09
333	2.89	0.21	-1.45	0.16	0.07	-1.45	0.16	0.10
336	1.50	0.18	-2.03	0.14	0.05	-2.08	0.14	0.08
341	2.93	0.22	-1.43	0.17	0.08	-1.43	0.17	0.10
351	3.01	0.19	-1.40	0.15	0.07	-1.39	0.15	0.09
352	3.23	0.22	-1.31	0.17	0.08	-1.29	0.17	0.10
370	1.80	0.21	-1.90	0.16	0.07	-1.94	0.16	0.10
377	2.22	0.20	-1.73	0.16	0.06	-1.75	0.15	0.09
379	2.72	0.20	-1.52	0.16	0.07	-1.52	0.15	0.09
392	2.19	0.24	-1.74	0.18	0.09	-1.76	0.18	0.11
395	2.24	0.19	-1.72	0.15	0.06	-1.74	0.15	0.09
396	2.10	0.33	-1.78	0.23	0.13	-1.80	0.23	0.15
397	2.47	0.21	-1.62	0.16	0.07	-1.64	0.16	0.10
402	2.28	0.21	-1.70	0.16	0.07	-1.72	0.16	0.10
409	1.97	0.30	-1.83	0.21	0.11	-1.86	0.21	0.14
420	2.85	0.18	-1.46	0.15	0.06	-1.46	0.14	0.08
422	1.32	0.21	-2.11	0.16	0.06	-2.16	0.16	0.10
429	2.65	0.21	-1.55	0.16	0.07	-1.55	0.16	0.10
430	2.38	0.19	-1.66	0.15	0.06	-1.68	0.15	0.09
432	3.84	0.35	-1.05	0.24	0.14	-1.02	0.25	0.16
434	2.40	0.16	-1.65	0.14	0.04	-1.67	0.13	0.07
435	2.44	0.28	-1.64	0.20	0.11	-1.65	0.20	0.13
441	2.72	0.23	-1.52	0.17	0.08	-1.52	0.17	0.10
471	3.31	0.65	-1.27	0.43	0.27	-1.26	0.44	0.29
493	2.24	0.23	-1.72	0.17	0.08	-1.74	0.17	0.10
495	2.45	0.21	-1.63	0.16	0.07	-1.65	0.16	0.10

continued on next page

Table 9: Leo II *continued*

ID	W' ^a (Å)	$\sigma_{W'}$ (Å)	[Fe/H] CG97	$\sigma_{[\text{Fe}/\text{H}]}$ Total	$\sigma_{[\text{Fe}/\text{H}]}$ Random	[Ca/H]	$\sigma_{[\text{Ca}/\text{H}]}$ Total	$\sigma_{[\text{Ca}/\text{H}]}$ Random
508	2.90	0.22	-1.44	0.17	0.08	-1.44	0.17	0.10
524	0.81	0.22	-2.32	0.16	0.06	-2.39	0.16	0.10
526	2.76	0.22	-1.50	0.17	0.08	-1.50	0.17	0.10
533	2.83	0.23	-1.47	0.17	0.08	-1.47	0.17	0.10
541	2.24	0.23	-1.72	0.17	0.08	-1.74	0.17	0.10
549	2.70	0.24	-1.53	0.18	0.09	-1.53	0.18	0.11
552	2.41	0.26	-1.65	0.19	0.10	-1.66	0.19	0.12
556	4.65	0.41	-0.71	0.28	0.17	-0.65	0.29	0.19
558	1.86	0.21	-1.88	0.16	0.07	-1.91	0.16	0.10
569	2.17	0.23	-1.75	0.17	0.08	-1.77	0.17	0.10
570	2.84	0.32	-1.47	0.23	0.13	-1.47	0.23	0.14
573	3.34	0.21	-1.26	0.16	0.07	-1.24	0.16	0.10
576	3.00	0.26	-1.40	0.19	0.10	-1.40	0.19	0.12
584	2.55	0.22	-1.59	0.17	0.08	-1.60	0.17	0.10
588	3.12	0.26	-1.35	0.19	0.10	-1.34	0.19	0.12
604	2.28	0.21	-1.70	0.16	0.07	-1.72	0.16	0.10
614	3.02	0.21	-1.39	0.16	0.08	-1.39	0.16	0.10
623	2.06	0.21	-1.79	0.16	0.07	-1.82	0.16	0.10

^a The W' values listed here have been scaled to the work of R97a.

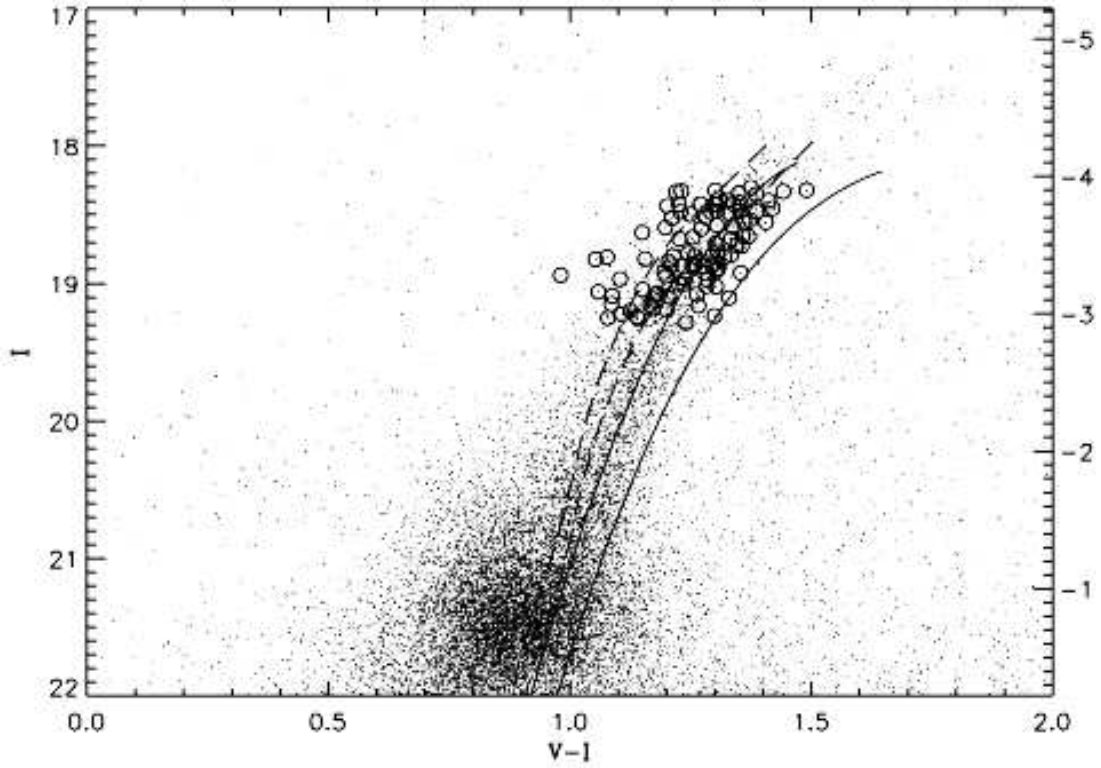


Figure 1. The color-magnitude diagram for the Leo I dSph with the spectroscopic targets shown as large circles. Solid lines show fiducials for Galactic globular clusters, from left to right, M15 with $[Fe/H] = -2.0$ and M2 with $[Fe/H] = -1.31$ (Da Costa & Armandroff 1990). The range in ages for the selected stars is demonstrated with the dashed lines representing Yale isochrones with $[Fe/H] = -1.28$ and with ages 2 and 4 Gyrs, from left to right, respectively; stars bluer than the M2 fiducial are likely younger. Note that, for convenience, we adopted the M15 fiducial to describe the shape of the Leo I RGB in selecting our spectroscopic targets.

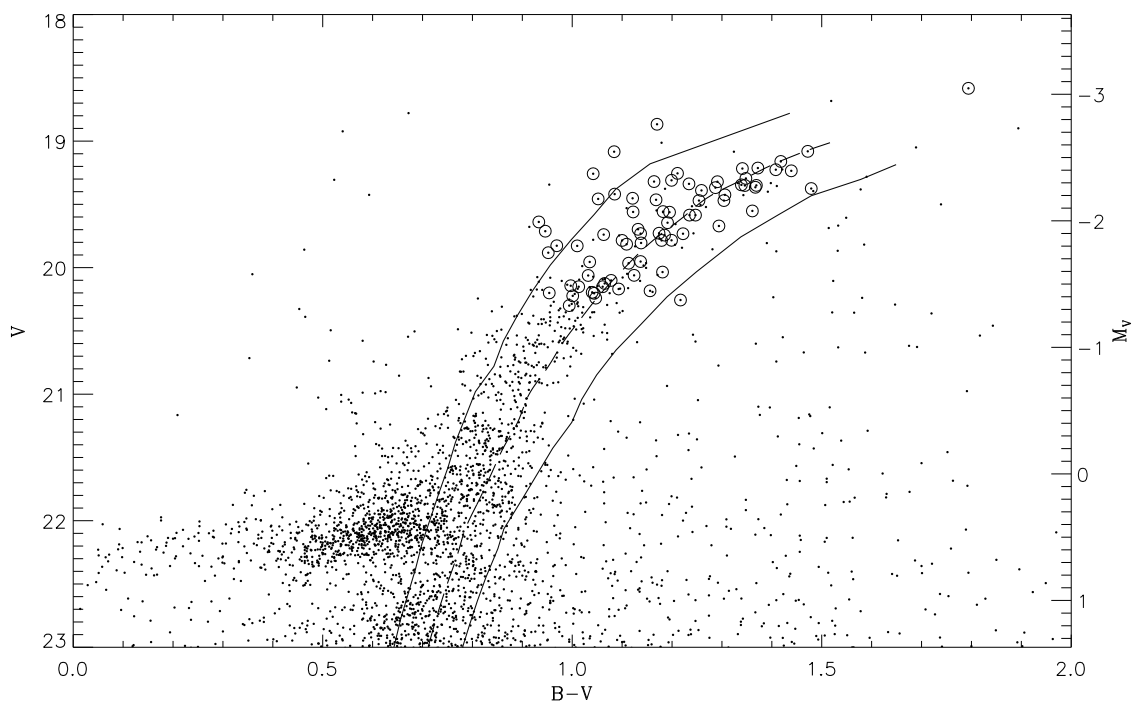


Figure 2. The color-magnitude diagram for the Leo II dSph with the spectroscopic targets shown as large circles. Solid lines show fiducials for Galactic globular clusters, from left to right, M68 with $[Fe/H] = -1.92$ (McClure et al. 1987) and M5 with $[Fe/H] = -1.17$ (Sandquist et al. 1996). The dashed line shows the adopted fiducial for the RGB of Leo II.

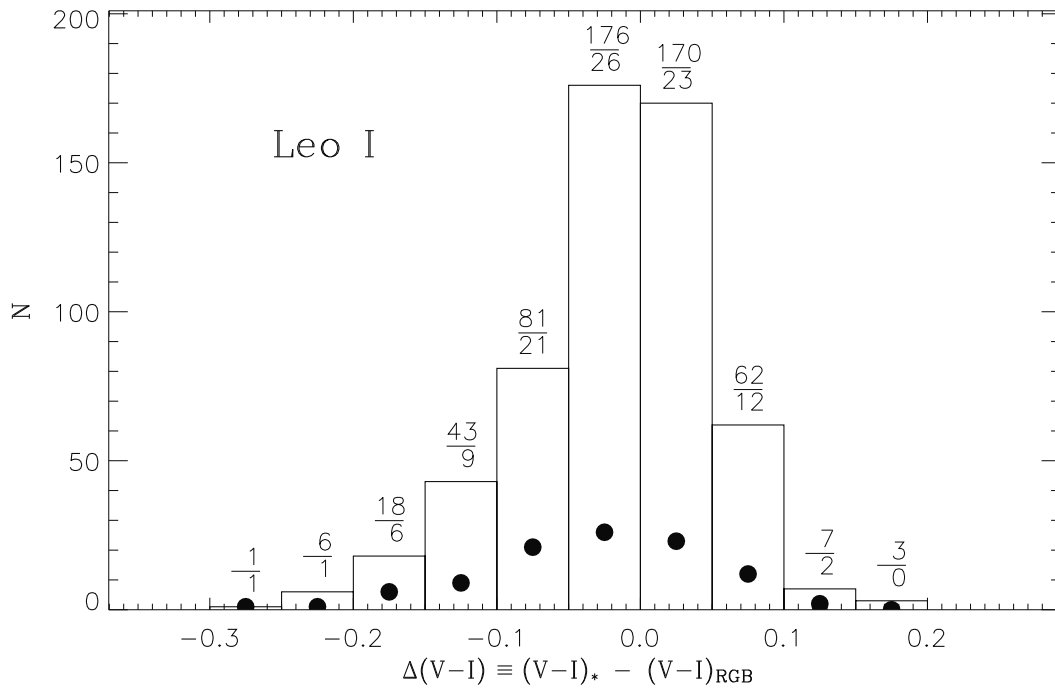


Figure 3. The histogram of the entire sample of RGB stars in the Leo I dSph (histogram) and the stars for which spectra were obtained (filled circles). Above each bin is given the number of stars in the bin in the total sample divided by the number of stars in the bin in the spectroscopic sample.

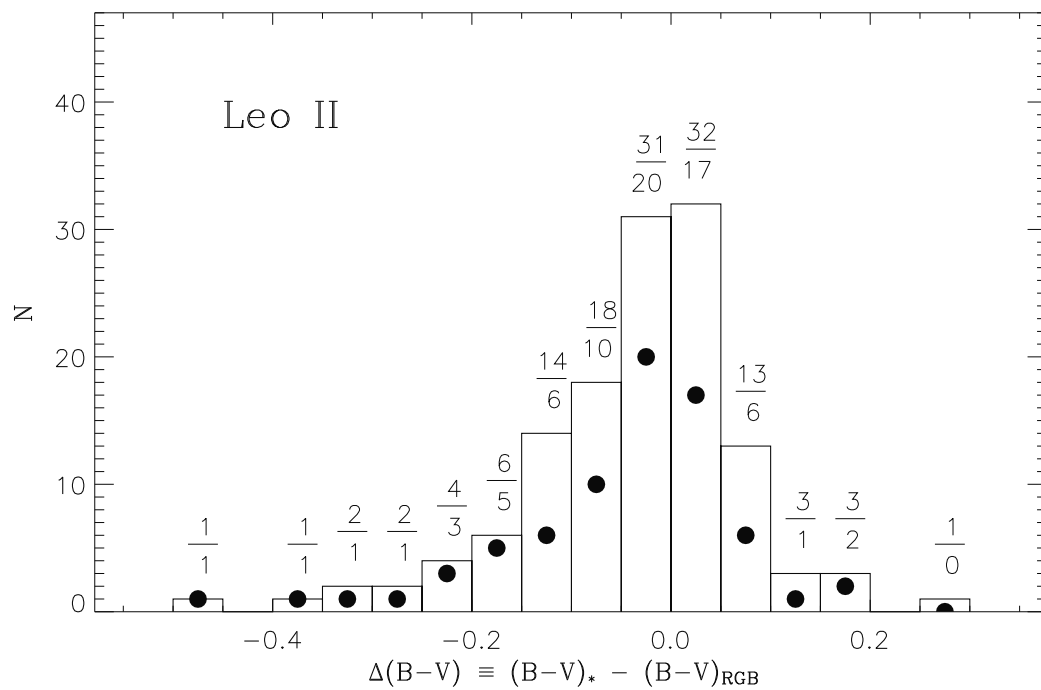


Figure 4. The histogram of the entire sample of RGB stars in the Leo II dSph (histogram) and the stars for which spectra were obtained (filled circles). Above each bin is given the number of stars in the bin in the total sample divided by the number of stars in the bin in the spectroscopic sample.

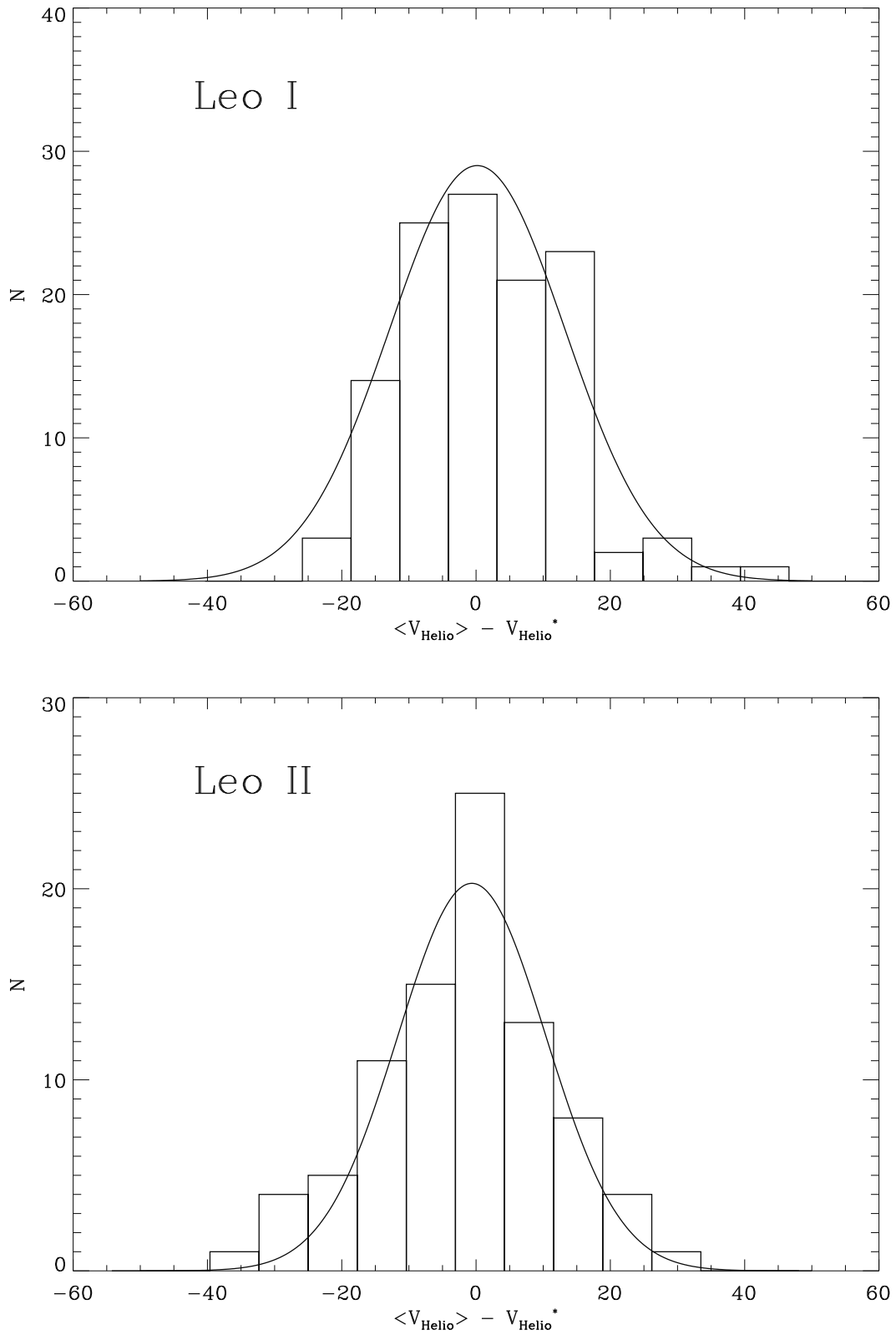


Figure 5. Velocity distributions of Leo I and Leo II overlaid with a Gaussian.

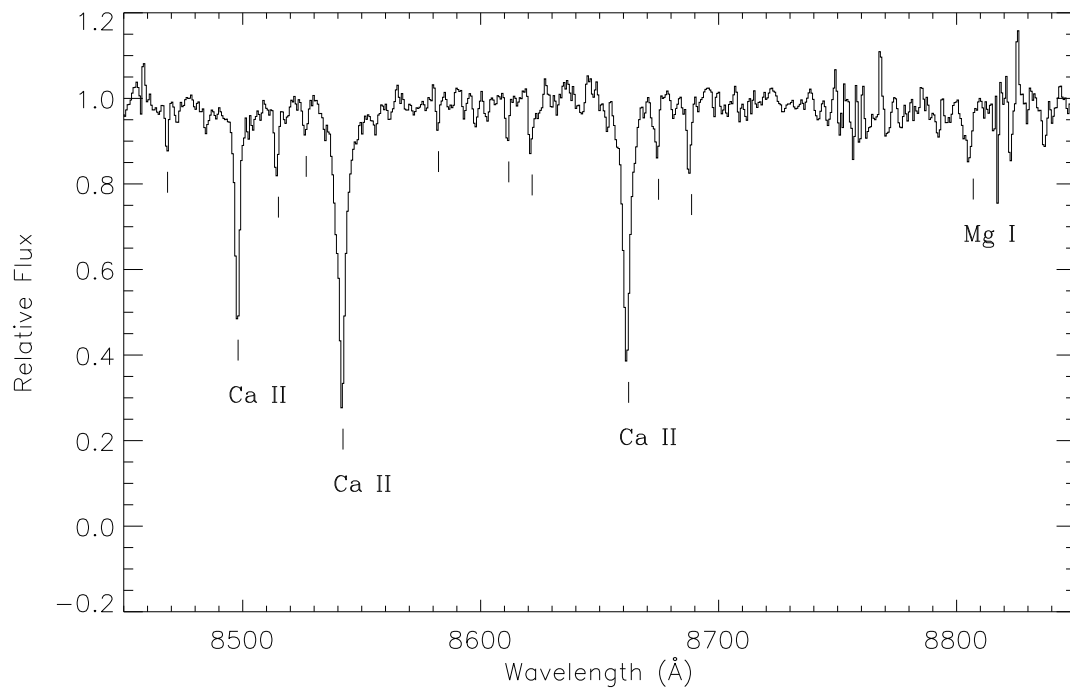


Figure 6. Low-dispersion spectrum of Star #9915 in the Leo I dSph with $[Ca/H] = -0.97$ and $SNR = 35$. For clarity, Fe I lines are marked but not labelled. Note that the Ca II lines are resolved but the weak Fe I lines are not. Indeed many of the Fe I lines are actually blends at this resolution ($R=14,000$).

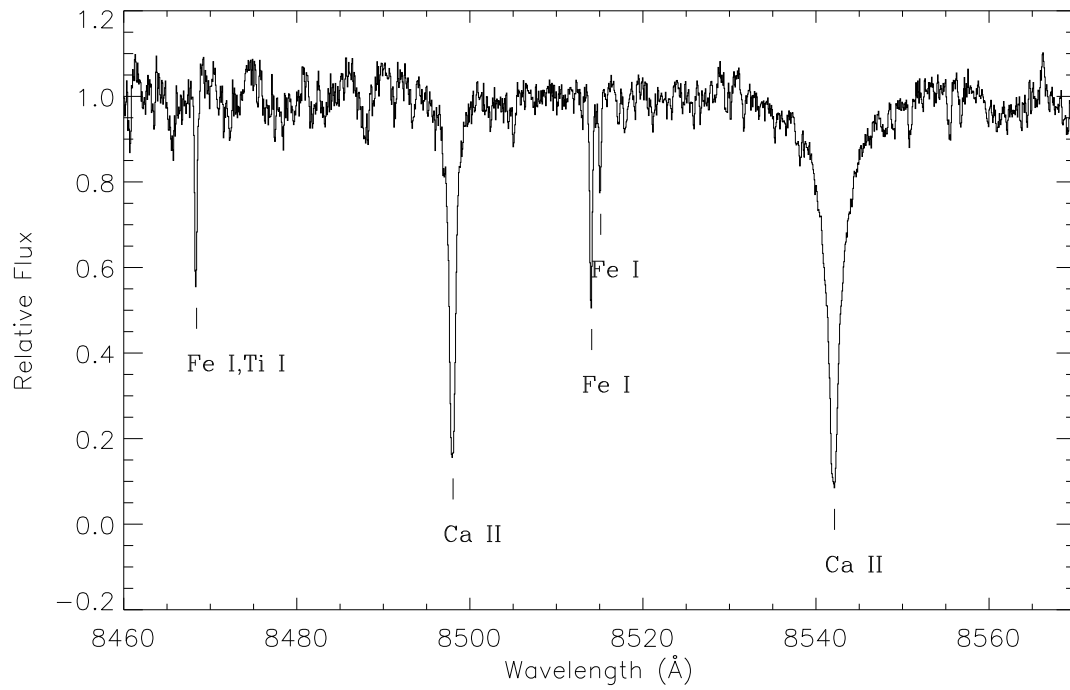


Figure 7. High-dispersion spectrum of calibration star HD135148, which as $[Fe/H] = -1.81$ and spectral type K0III (Bosler 2004). The wavelength coverage is much narrower than that of Fig 6. Note how the two Fe I lines blended in the low dispersion spectrum are resolved at higher resolution ($R=40,000$) while the Ca II lines are resolved at both resolutions (see Figure 6).

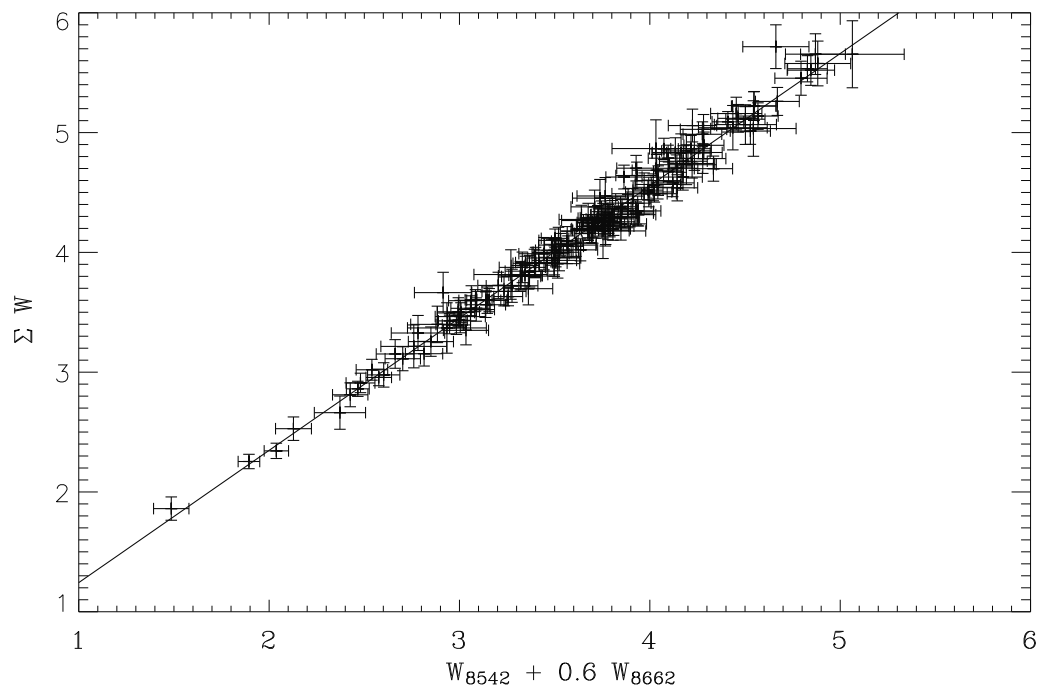


Figure 8. The relationship between the weighted sum of the two strongest Ca II lines and the weighted sum of all three Ca II lines in the globular cluster stars.

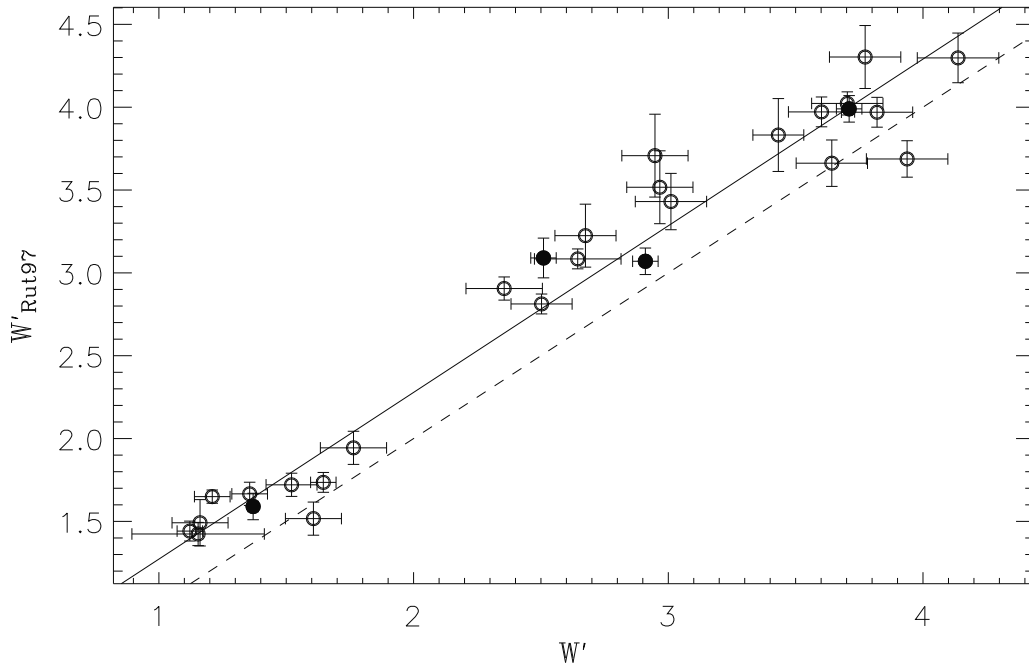


Figure 9. The reduced equivalent width measured by us and R97a for individual globular cluster stars in NGC 1904, NGC 4590, NGC 5272, and NGC 6171 (open circles), and the averages for the clusters (filled circles). The dashed line shows the line of equivalence. The solid line shows the regression using the W' values for individual stars.

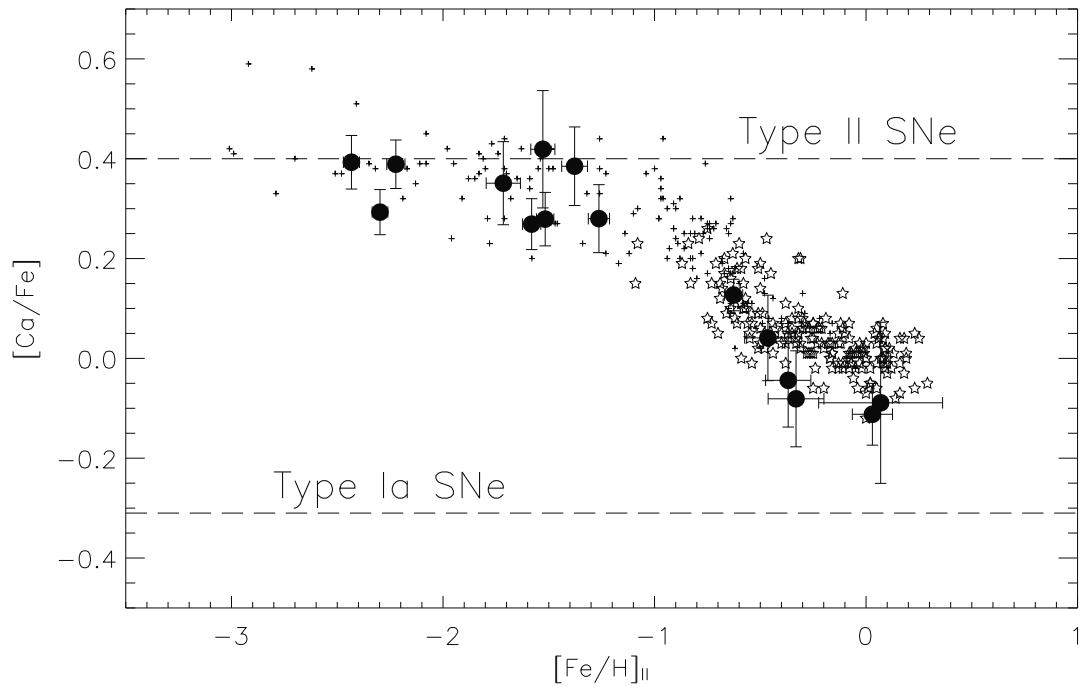


Figure 10. The $[Ca/Fe]$ ratio as a function of $[Fe/H]$ for all Galactic clusters from Bosler(2004; large filled circles) and individual Milky Way field stars from Fulbright (2000; pluses) and Edvardsson et al. (1993; open stars). Dashed horizontal lines indicate the predicted abundance ratios from Type II and Type Ia SNe (+0.4 from McWilliam, 1997 and -0.31 from Thielemann et al. 1986, respectively).

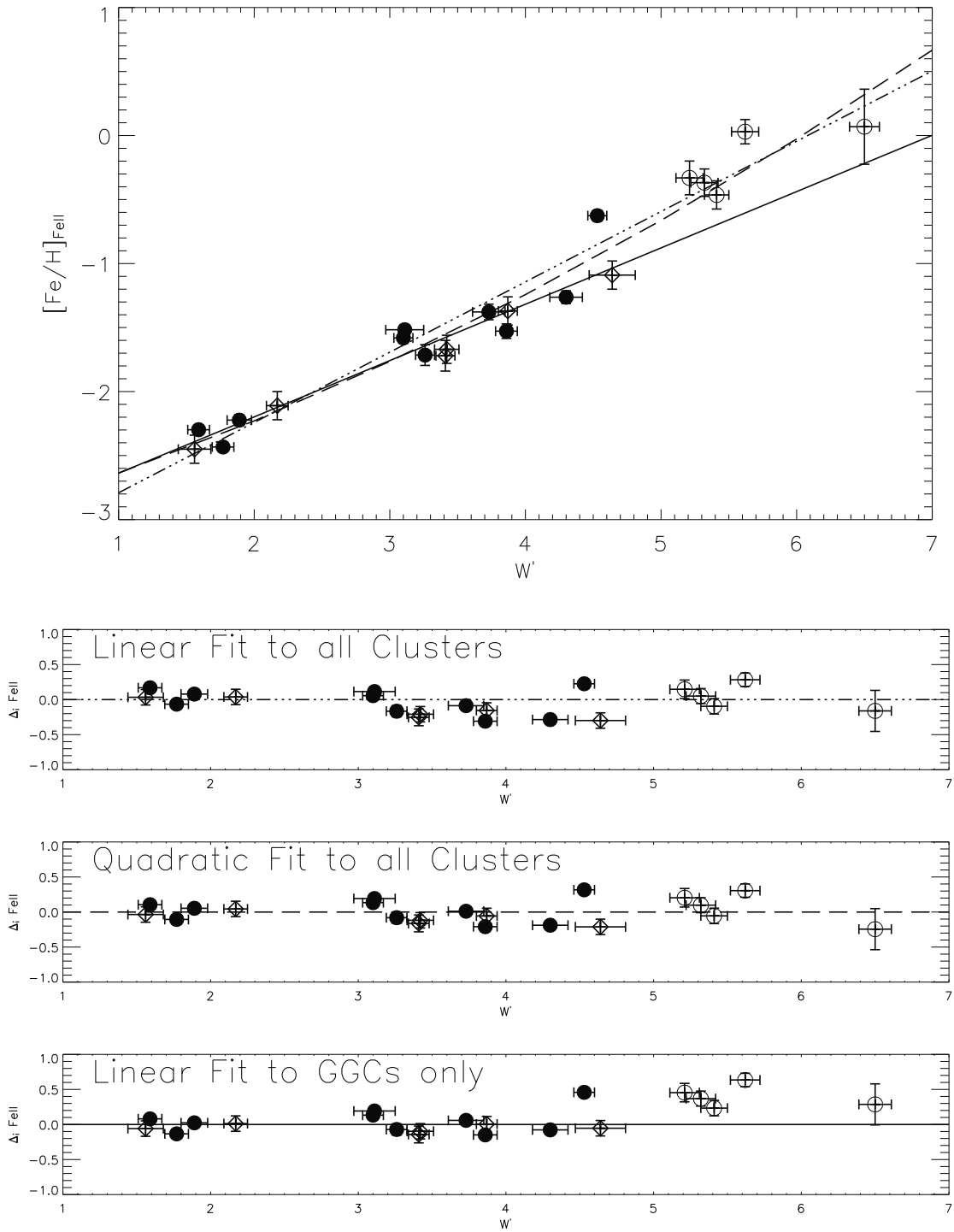


Figure 11. $[\text{Ca}/\text{H}]$ versus W' and residuals for all observed clusters. Solid circles indicate GGCs; open circles indicate GOCs; and the KI03 clusters scaled to this data set are indicated with open diamonds

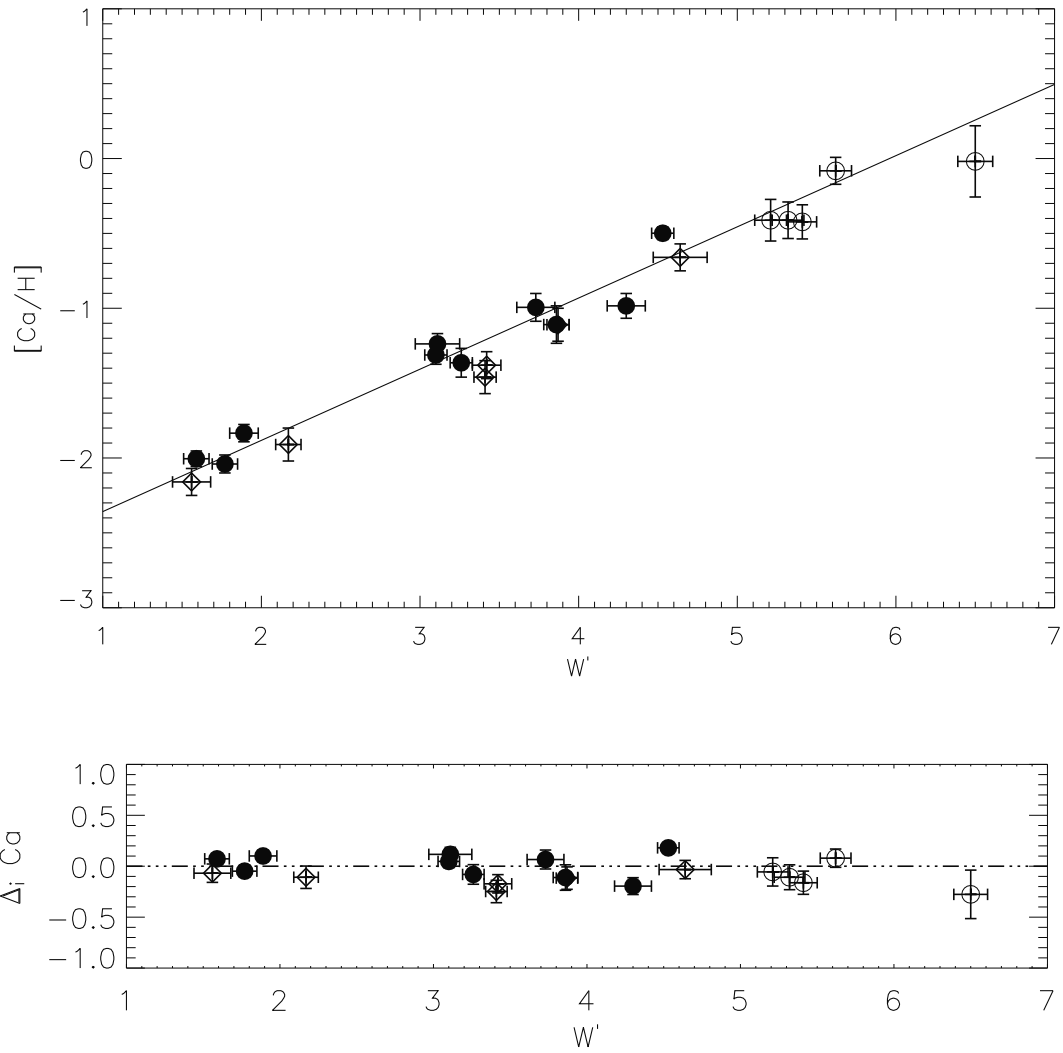


Figure 12. Iron abundances from singly-ionized lines versus reduced equivalent width and residuals for all of the clusters. Solid circles indicate GGCs; open circles indicate GOCs; and the KI03 clusters scaled to this data set are indicated with open diamonds. The dotted-dashed line indicates a linear fit to all stars, the dashed line is a 2nd order polynomial, and the solid line indicates a linear fit to the GGCs with $[Fe/H] < -0.8$, see text for details.

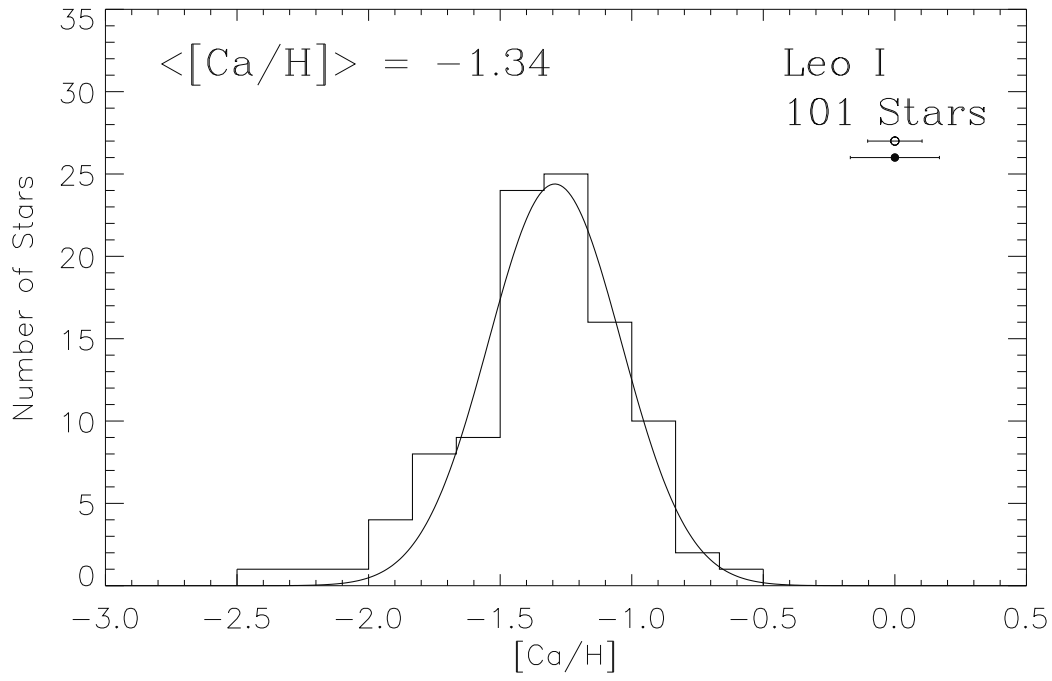


Figure 13. The metallicity distribution function in the Leo I dSph. Typical $1-\sigma$ errors shown in the upper right; random and total errors are shown as open and filled circles, respectively. The Gaussian fit to the distribution is shown as a solid line.

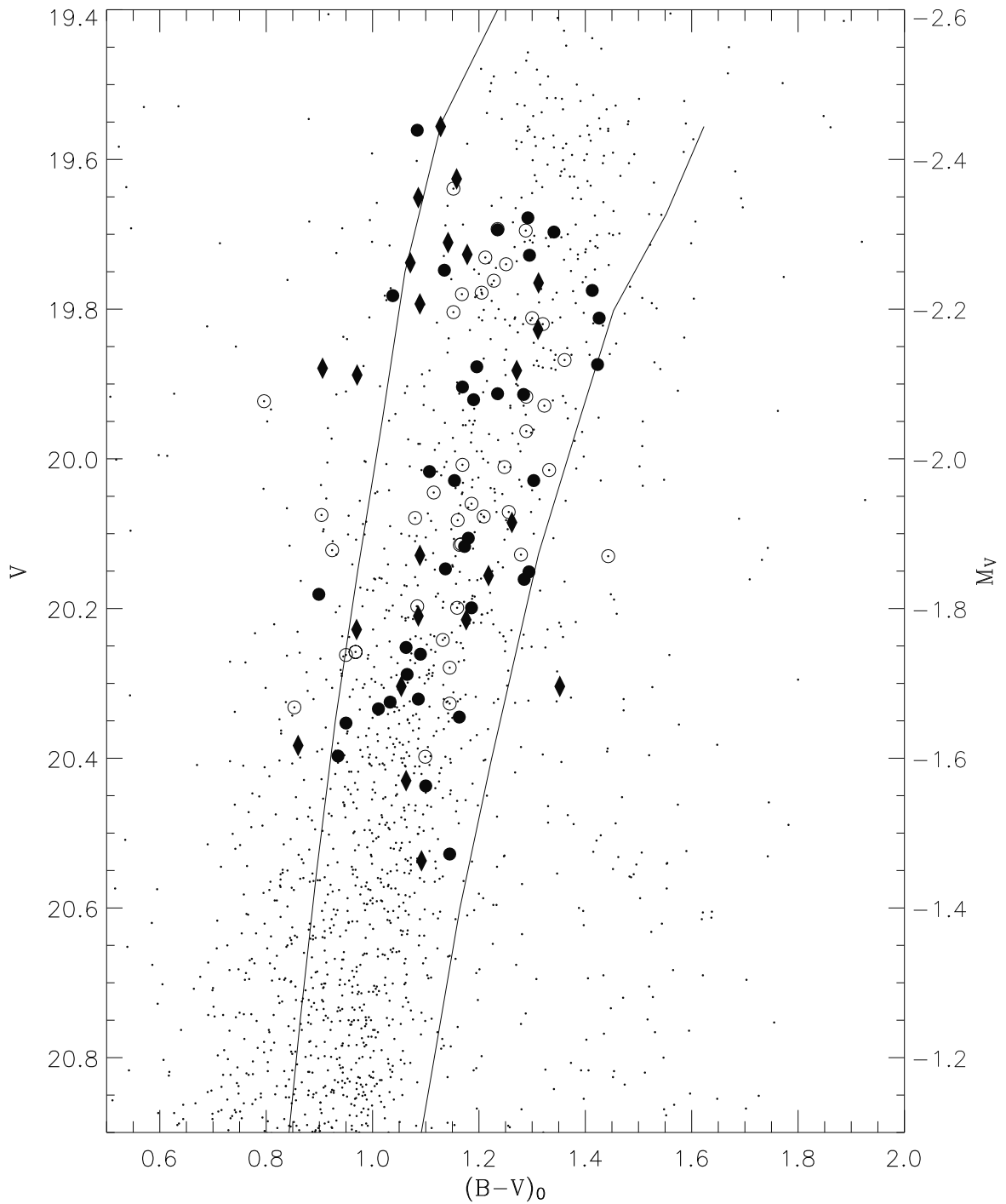


Figure 14. The CMD of Leo I showing the metallicities of the stars. V, B–V rather than I, V–I is shown for ease of comparison with the Leo II CMD. Stars are coded based on their derived metallicity: filled diamonds for stars with $[Ca/H] < -1.5$; open circles for stars with $-1.5 \leq [Ca/H] < -1.2$; filled circles for stars with $[Ca/H] \geq -1.2$. The fiducials for GGCs M5 ($[Ca/H] = -0.96$) and M68 ($[Ca/H] = -1.78$) are over-plotted for reference.

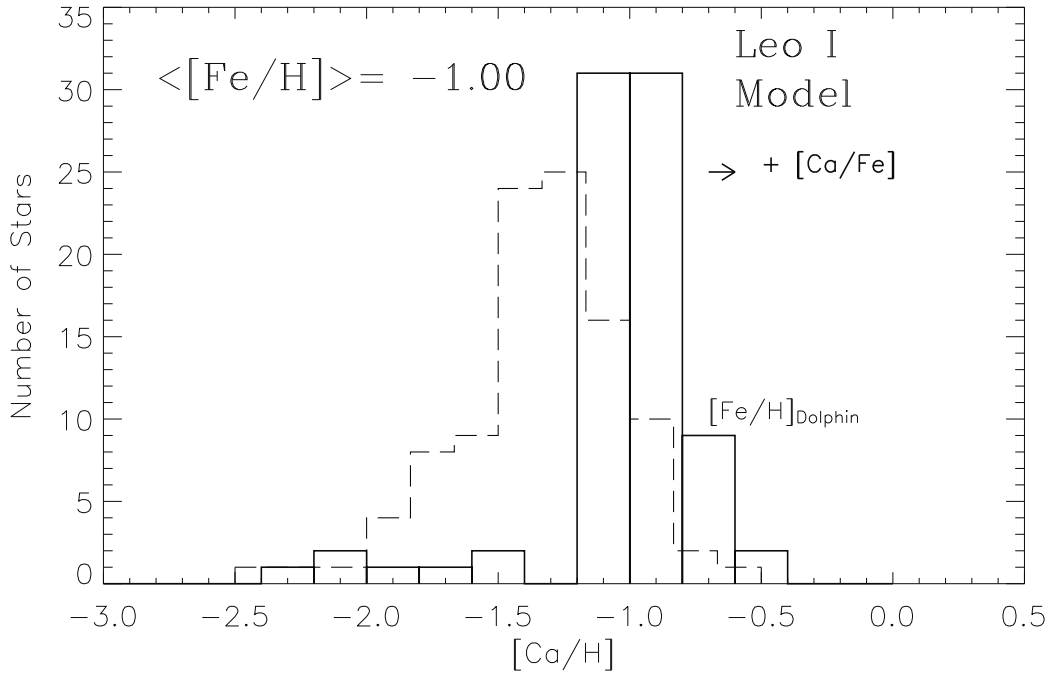


Figure 15. The predicted metallicity distribution from Dolphin’s CMD modelling of the Leo I dSph (solid lines) along with the observed distribution (dashed lines). Note that Dolphin derived $[Fe/H]$ and a significant offset exists between the two distributions. If $[Ca/Fe]$ from Shetrone et al. (2003) is added to Dolphin’s $[Fe/H]$ values yield $[Ca/H]$ (indicated with an arrow of length 0.1 dex), the theoretical histogram shifts even further from the observed distribution (see text for discussion).

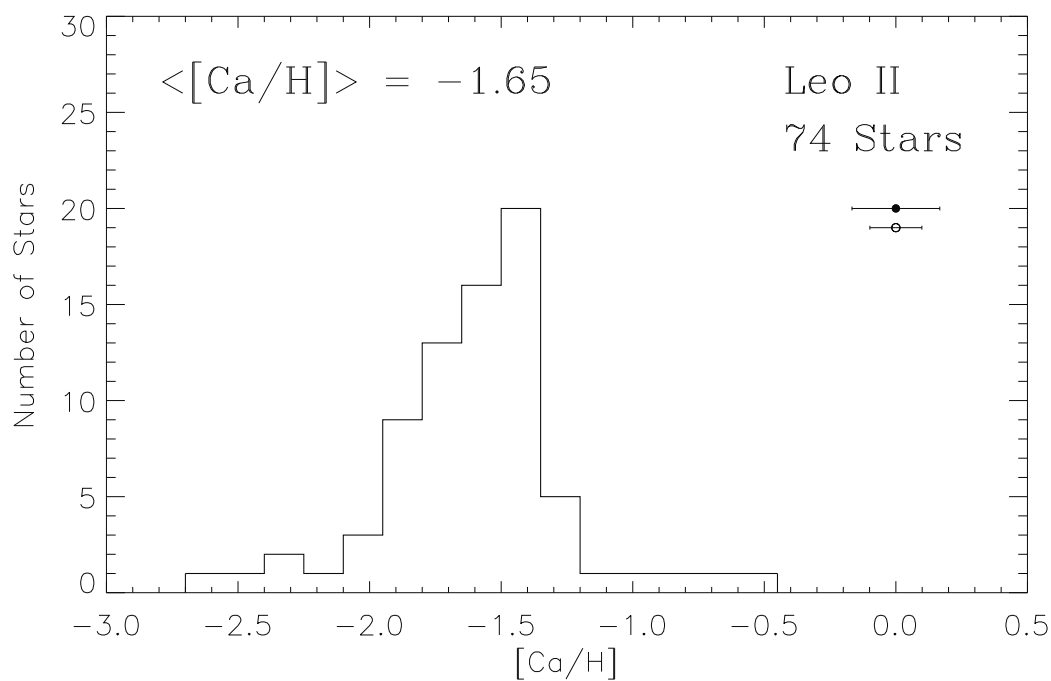


Figure 16. The observed metallicity distribution function in the Leo II dSph. Typical $1\text{-}\sigma$ errors are shown in the upper right; median random and total errors are shown as open and filled circles, respectively.

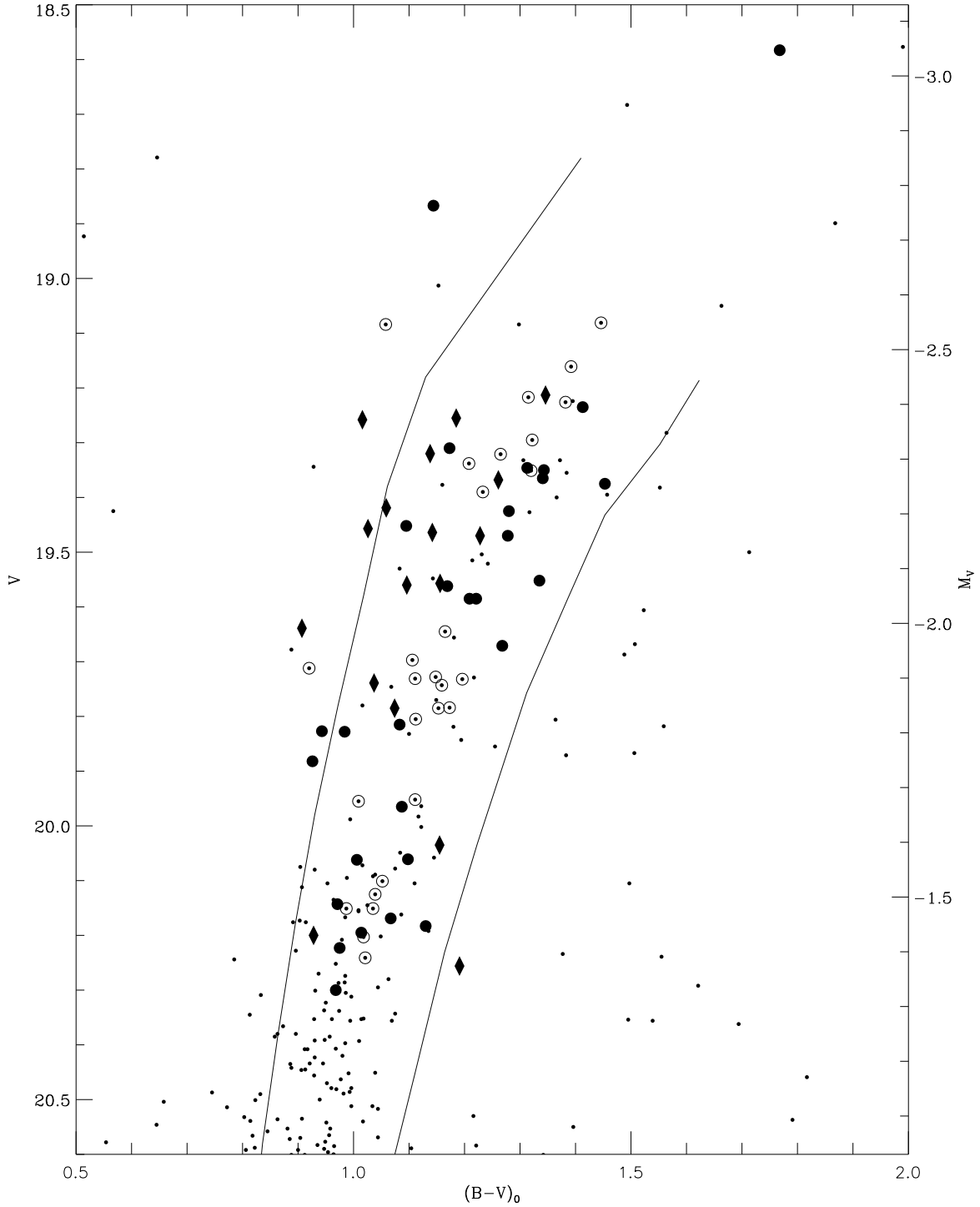


Figure 17. The CMD of Leo II showing the metallicities of the stars. Stars are coded based on their derived metallicity: filled diamonds for stars with $[Ca/H] < -1.8$; open circles for stars with $-1.8 \leq [Ca/H] < -1.5$; filled circles for stars with $[Ca/H] \geq -1.5$. The fiducials for GGCs M5 ($[Ca/H] = -0.96$) and M68 ($[Ca/H] = -1.78$) are over-plotted for reference.

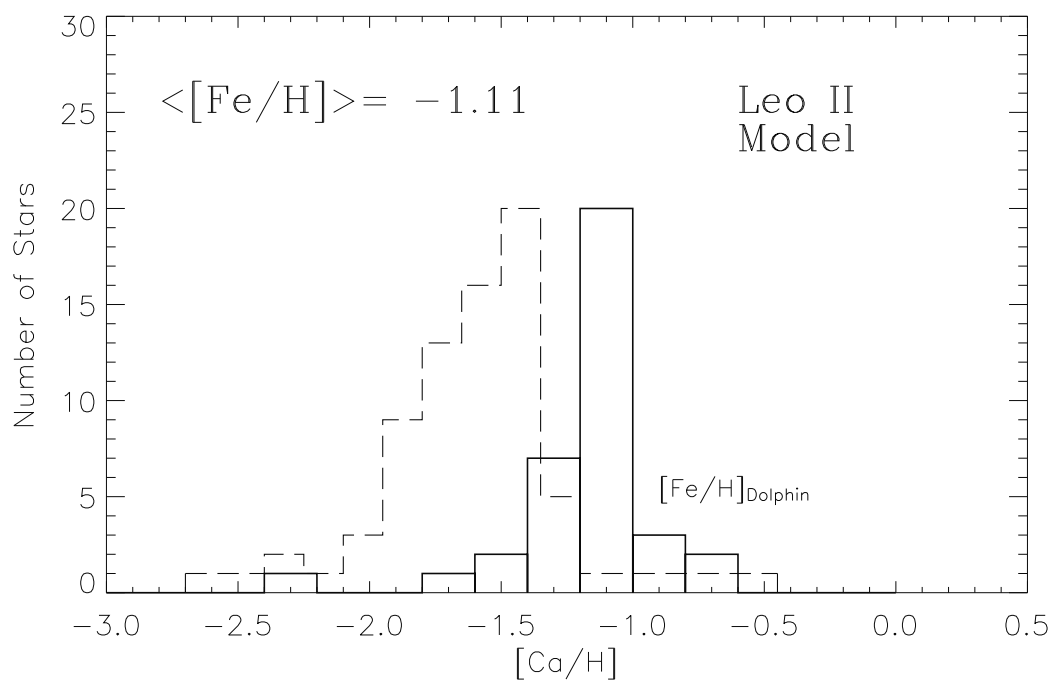


Figure 18. The predicted metallicity distribution from Dolphin's CMD modelling of the Leo II dSph (solid lines) along with the observed distribution (dashed lines). Note that Dolphin derived $[Fe/H]$ rather than $[Ca/H]$ values, and a significant offset exists between the central values of the two distributions (see text for discussion).